

DOCTORAL THESIS

Tribological Behavior of Hybrid Coatings at Extreme Conditions

Asad Alamgir Shaikh

TALLINN UNIVERSITY OF TECHNOLOGY
DOCTORAL THESIS
33/2021

Tribological Behavior of Hybrid Coatings at Extreme Conditions

ASAD ALAMGIR SHAIKH



TALLINN UNIVERSITY OF TECHNOLOGY

School of Engineering

Department of Mechanical and Industrial Engineering

This dissertation was accepted for the defense of the degree 22/04/2021

Supervisor: Senior Research Scientist Vitali Podgursky
School of Engineering
Department of Mechanical and Industrial Engineering
Tallinn University of Technology
Tallinn, Estonia

Co-Supervisor: Prof. Fjodor Sergejev
School of Engineering
Department of Mechanical and Industrial Engineering
Tallinn University of Technology
Tallinn, Estonia

Opponents: Research Professor, D.Sc.(Tech.) Anssi Laukkanen
Computational Materials and Data Sciences
VTT Technical Research Centre of Finland Ltd.
Espoo, Finland

Associate Professor in Materials Science Sergei Vlassov
Laboratory of Physics of Nanostructures
Institute of Physics, University of Tartu
Tartu, Estonia

Defence of the thesis: 21/06/2021, Tallinn

Declaration:

Hereby I declare that this doctoral thesis represents my original investigation and achievements and is submitted for doctoral degree at Tallinn University of Technology. It has not been submitted elsewhere for a doctoral or equivalent academic degree.

Asad Alamgir Shaikh

signature



European Union
European Regional
Development Fund



Investing
in your future

Copyright: Asad Alamgir Shaikh, 2021

ISSN 2585-6898 (publication)

ISBN 978-9949-83-705-2 (publication)

ISSN 2585-6901 (PDF)

ISBN 978-9949-83-706-9 (PDF)

Printed by Koopia Niini & Rauam

TALLINNA TEHNIKAÜLIKOOL
DOKTORITÖÖ
33/2021

Hübriidpinnete triboloogiline käitumine ekstreemsetes tingimustes

ASAD ALAMGIR SHAIKH



Contents

List of Publications	6
Author's Contribution to the Publications	7
List of Other Publications	8
Introduction	9
List of Abbreviations and Symbols	11
1 Overview of the literature.....	13
1.1 Classification of chemical bonding	13
1.2 Types of coating	14
1.2.1 Carbon based coatings	14
1.2.2 Oxide based coatings	15
1.2.3 Hybrid coatings	17
1.3 Coating generations	18
1.4 Fundamentals of coating tribology	18
1.4.1 Wear and friction mechanisms	19
1.4.2 Solid lubrication	20
1.4.3 Self-organization and self-organized criticality	21
1.5 Aim and objectives of thesis	22
2 Materials and methods	23
2.1 Deposition techniques	23
2.2 Sliding tests	23
2.3 Nanoindentation and nanoscratch	25
2.4 Characterization methods.....	26
3 Results and discussion.....	27
3.1 Investigation of thin alumina layers prepared on Si(100) substrate	27
3.2 Self-organized criticality on nanocrystalline diamond	30
3.3 Tribological behavior of hard multilayer coatings.....	36
3.4 Tribological performance of a-C:H:Si and Al ₂ O ₃ /a-C:H:Si coatings	41
4 Conclusions	49
References	51
Acknowledgements.....	57
Abstract.....	58
Lühikokkuvõte.....	59
Appendix	61
Curriculum vitae.....	112
Elulookirjeldus.....	113

List of Publications

The following is the list of publications by the author on the basis of which this thesis has been prepared:

- Publication I. **Alamgir, A.**, Bogatov, A., Yashin, M. and Podgursky, V., 2019. Mechanical and tribological properties of 100-nm thick alumina films prepared by atomic layer deposition on Si (100) substrates. *Proceedings of the Estonian Academy of Sciences*, 68(2), pp. 126-130.
- Publication II. Bogatov, A., Podgursky, V., Vagiström, H., Yashin, M., **Shaikh, A.A.**, Viljus, M., Menezes, P.L. and Gershman, I.S., 2019. Transition from Self-Organized Criticality into Self-Organization during Sliding Si₃N₄ Balls against Nanocrystalline Diamond Films. *Entropy*, 21(11), p. 1055.
- Publication III. **Alamgir, A.**, Yashin, M., Bogatov, A., Viljus, M., Traksmäa, R., Sondor, J., Lümkmann, A., Sergejev, F. and Podgursky, V., 2020. High-temperature tribological performance of hard multilayer TiN-ALTiN/nACo-CrN/AlCrN-AlCrO-ALTiCrN coating deposited on WC-Co substrate. *Coatings*, 10(9), p. 909.
- Publication IV. Podgursky, V., **Alamgir, A.**, Yashin, M., Jögiaas, T., Viljus, M., Raadik, T., Danilson, M., Sergejev, F., Lümkmann, A., Kluson, J. and Sondor, J., 2021. High-Temperature Tribological Performance of Al₂O₃/aC: H: Si Coating in Ambient Air. *Coatings*, 11(5), p. 495.

Manuscripts are included in the Appendix.

Author's Contribution to the Publications

The contributions of the author to the papers included in this thesis are as follows:

Publication I. Corresponding author. Indentation and scratch tests, SEM investigation, processing of data, calculations, text writing.

Publication II. Co-author. Sliding tests, SEM investigation, text writing.

Publication III. Corresponding author. Sliding tests, profilometry and SEM investigation, processing of data, calculations, text writing.

Publication IV. Corresponding author. Sliding tests, profilometry and SEM investigation, processing of data, calculations, text writing.

List of Other Publications

- I. Podgursky, V., Yashin, M., Jõgiaas, T., Viljus, M., **Alamgir, A.**, Danilson, M. and Bogatov, A., 2020. High Temperature Tribological Properties of Al₂O₃/NCD Films Investigated Under Ambient Air Conditions. *Coatings*, 10(2), p.175.
- II. **Shaikh, A.**, Churyumov, A., Pozdniakov, A. and Churyumova, T., 2020. Simulation of the Hot Deformation and Fracture Behavior of Reduced Activation Ferritic/Martensitic 13CrMoNbV Steel. *Applied Sciences*, 10(2), p.530.

Introduction

Wear-resistant (hard) coatings were developed using the knowledge obtained from materials science of bulk materials. The tribological response of a coating system depends on many factors (coating properties, counterpart, substrate, interface and running conditions and many other aspects); therefore, selecting an appropriate coating for a given tribological application is still a difficult and complicated task. New deposition techniques, which provide in addition a wide range of selections of tribological coatings, are constantly updates.

Holmberg and Erdemir [1] concluded that a huge amount of the world's total energy consumption, i.e., ~23%, is due to friction and wear occurring at tribological contacts. Friction and wear of moving mechanical systems lead to energy and material losses. It causes huge economic and environmental impacts because a significant amount of fuel and energy is used for the exploitation of mechanical systems at high friction and remanufacturing and replacement of worn parts. Therefore, minimization of heat generation, friction and wear demand in industry is essential for sustainable development of global economy. In the area of industry 4.0, the surface engineering meets the ever-increasing demands for quality, flexibility, productivity, and environmental performance with respect to new machining and forming technologies, including near net shape production, high speed machining, hard turning, micromanufacturing, dry machining, and environmentally friendly machining. Effective execution requires high performance tools. The tools must be able to endure extreme cyclic contact with rapidly heated materials at high temperatures. The ideal tool material should combine properties like high hardness, good toughness and chemical stability. It is very important for these properties to hold out under a wide range of extremal external conditions, including high temperature and aggressive environment.

In previous studies carried out in TalTech, several characteristic types of the coefficient of friction (CoF) vs cycle curves were addressed during sliding on diamond coatings [2]. Formation of a carbonaceous layer, ripple and groove patterns was found within the wear scars [3], which indicates self-organization during sliding. Furthermore, the diamond coating deflection (plastic deformation) on a silicon substrate was observed in sliding tests [4]. The degradation of the diamond coatings properties in sliding tests at high temperature was investigated in [5].

In the present thesis, the main focus is on the improvement of tribological properties of coatings tested at high temperature in air by using thin oxide layers.

Scientific novelties of the present PhD thesis:

1. The thin alumina layer preserves the excellent tribological properties of hydrogenated amorphous carbon doped with the Si (a-C:H:Si) coating at high temperature. The thin oxide layer is an adaptive layer, it inhibits atmospheric oxidation attack and improves the coating lifetime.
2. The superlubricating effect was observed on the Al_2O_3 / a-C:H:Si coating in sliding tests at high temperature.
3. Due to the phase transition from fcc-(AlCr)O to α -(AlCr)O in the hard multilayer coating TiN-AlTiN/nAlCo-CrN/AlCrN-AlCrO-AlTiCrN (HMC) in sliding tests at 800 °C, the decrease of the CoF value and wear was observed.
4. Coating deflection was found on a-C:H:Si and HMC coatings. Therefore, coating deflection is a general phenomenon for broad spectra of coatings.
5. Transition from self-organized criticality to self-organization during the running-in period was found in the nanocrystalline diamond coating.

Approbation

Publications and conferences

In addition to publications in peer-reviewed journals presented in the appendix section, the author of this thesis has participated in five symposiums and seminars and made four oral and one poster presentations.

Collaborations

This research work was conducted in collaboration and support of scientific institutes and an industrial partner as follows:

- 1) Department of Materials and Environmental Technology, Tallinn University of Technology, performed the Raman and XPS analyses on coatings.
- 2) Institute of Physics, University of Tartu, the thin oxide layer was deposited on the surface of coatings surface by the atomic layer deposition method.
- 3) Moscow State Technological University “Stankin” (MSTU “STANKIN”), developed the theory of self-organization and self-organized criticality.

This research was partially carried out in collaboration with the industrial partner “PLATIT AG”, a leading Swiss company. PLATIT is one of the world leaders in the field of Physical Vapor Deposition technology.

List of Abbreviations and Symbols

Abbreviations

ALD	Atomic layer deposition
CoF	Coefficient of Friction
CVD	Chemical Vapor Deposition
DLC	Diamond-Like Carbon
EDS	Energy-dispersive X-ray spectroscopy
HT	High-Temperature
HMC	TiN-AlTiN/nACo-CrN/AlCrN-AlCrO-AlTiCrN
h	Hour
HT-XRD	High-temperature X-ray diffraction
min	Minute
PACVD	Plasma Assisted Chemical Vapor Deposition
NCD	Nanocrystalline Diamond
QUAD	Fourth generation coatings from AG Platit
RT	Room-Temperature
SCD	Single-Crystal Diamond
sec	second
SEM	Scanning Electron Microscopy
SOC	Self-organized criticality
SO	Self-organization
Si	Silicon
t-Pa	Trans-polyacetylene
UMT	Universal Material Tester
XPS	X-ray photoelectron spectroscopy
XRD	X-ray diffraction
WC-Co	Tungsten carbide cobalt

Symbols

Greek

P_{\max}	Maximum load (mN)
ν_i and ν_s	Poisson's ratio
Δ_1, Δ_2 and Δ_3	Coating deformation (nm)
μ	Power-law exponent

Latin

A_f	Indentation area (μm^2)
E_r	Reduced modulus (GPa)
E	Young's modulus (GPa)
F_x	Friction force (N)
F_z	Normal load (N)
l	Length of wear scar (mm)
k	Coefficient of friction
r	Radius of wear scar (mm)
S_s	Cross-section area of wear scar (μm^2)
T	Temperature ($^{\circ}\text{C}$)
t	Time
r	Radius of wear scar (mm)
v	Velocity of sliding test (rpm)
V	Volume of the wear scar (mm^3)

1 Overview of the literature

Advanced tribological technology can reduce wear and friction, thus a decrease of economic expenditures together with environmental benefits can be achieved [1]. Smart tribology systems can provide an ultra-low friction coefficient, high wear resistance, and promising mechanical properties. Coating deposition is one of the most widely used approaches, which allows tailoring surface morphology, improving friction and wear performance, fatigue strength, etc., of the tribological substrate/coating system [1].

This chapter provides a brief overview of the studies of thin hard coatings.

1.1 Classification of chemical bonding

Traditionally, several types of chemical bonding are defined as ionic (heteropolar), covalent (homopolar) and metallic bonds. Based on the type of bonding, the classification of hard ceramic coatings is presented in Fig. 1.1. A metallic bond is a chemical bond formed by positively charged atoms sharing their free electrons among a lattice of cations. Covalent and ionic bonds, on the other hand, form between two discrete atoms. Ceramic coatings possess usually several types of bonds.

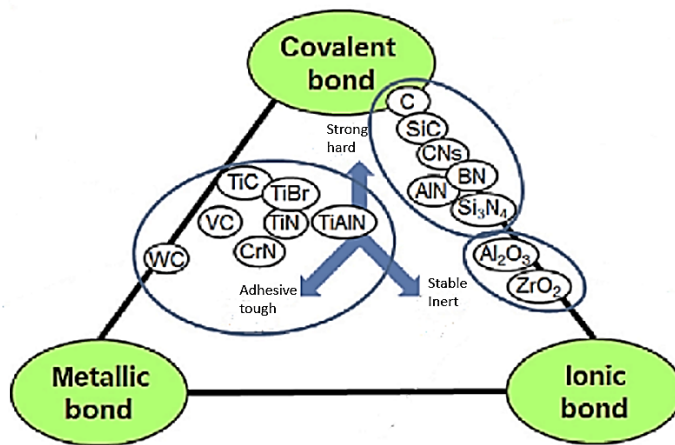


Figure 1.1. Hard ceramic materials are divided into groups based on their bonding type [6].

Coatings with metallic bond

The most common type of a chemical bond formed between metal atoms is metallic bonding. Metallic bonds are seen in pure metals, alloys and some metalloids. For instance, graphene has two-dimensional metallic bonding. Pure metals can form other types of chemical bonds also between their atoms.

Metals are considered good conductors of heat and electricity. The outer energy levels of metal atoms (the *s* and *p* orbitals) are overlapped. The valence electrons can move from one atom to the other as the outermost shell of electrons of each metal atoms overlaps the neighboring atoms. The electrons form an "electron sea" in which valence electrons are free to move from one atom to another. Metallic bonding may be seen as a consequence of a material having many more delocalized energy states than it has delocalized electrons (electron deficiency); so, localized unpaired electrons may become delocalized and mobile. The materials with metallic bonds show good adhesive properties and toughness. Coatings with metal bonding are TiN, TiC, CrN, etc.

Coatings with covalent bond

The covalent bond is an interatomic linkage that results from the sharing of an electron pair between two atoms. The binding arises from the electrostatic attraction of their nuclei for the same electrons. The sp^2 and sp^3 hybridizations of covalent bonds occur in carbon based materials. Covalent bonding is one of the strongest among the other types of bonds.

The idea that two electrons can be shared between two atoms and serve as the link between them was introduced in 1916 by the American chemist G.N. Lewis [7] who described the formation of such bonds as resulting from the tendencies of certain atoms to combine with one another in order for both to have the electronic structure of a corresponding noble-gas atom. The materials with covalent bonds are hard. Carbon based Si_3N_4 , TiN, CrN are the examples of covalent bonded coatings.

Coatings with ionic bond

The electrostatic attraction between oppositely charged ions in a chemical compound forms an ionic bond. When the valence (outermost) electrons of one atom are transferred to another atom, a bond is formed. When an atom loses electrons, it becomes a positively charged ion (cation), while when it gains them, it becomes a negatively charged ion (anion).

An ionic bond is a type of polar covalent bond that results from an unequal electron sharing rather than completing electron transfer. When the electronegativities of the two atoms vary greatly, ionic bonds form, while covalent bonds form when the electronegativities are identical. The materials with ionic bonds are chemically inert and stable. Coatings with ionic bonding structures include oxides like Al_2O_3 and ZrO_2 .

1.2 Types of coating

1.2.1 Carbon based coatings

Carbon-based coatings have found wide industrial applications (aerospace, automotive, machine tools, medical implants, etc.) due to the low CoF of different types of friction pairs, good mechanical properties and chemical inertness. Polycrystalline diamond (micro-, nano-, or ultra-nano crystalline) [8] can be deposited on a variety of tools to mimic the properties that are similar to single crystal diamond. Diamond coated cutting tools are used, for instance, for machining of Al and Cu alloys and composite materials. Amorphous DLC coatings have excellent tribological properties. The potential applications of DLC coatings for space exploration were reported in [8,9]. Figure 1.2 shows a ternary phase diagram of various forms of amorphous C-H materials [10]. The DLC coatings with different composition can be prepared by using CVD and PVD deposition techniques. The surface and bulk properties can be modified by doping (Si, W, O, etc.), annealing and irradiation. Coating surface properties can be modified by using different lubricants and ambient environments, post-treatment of the surface by plasma, deposition of thin adaptive layers, etc. It was claimed in the studies reported on the thermal stability of the DLC coating that DLC becomes unstable at a relatively low temperature, i.e., 200-300 °C, due to structural changes induced by the conversion of sp^3 to sp^2 bonds [11-13].

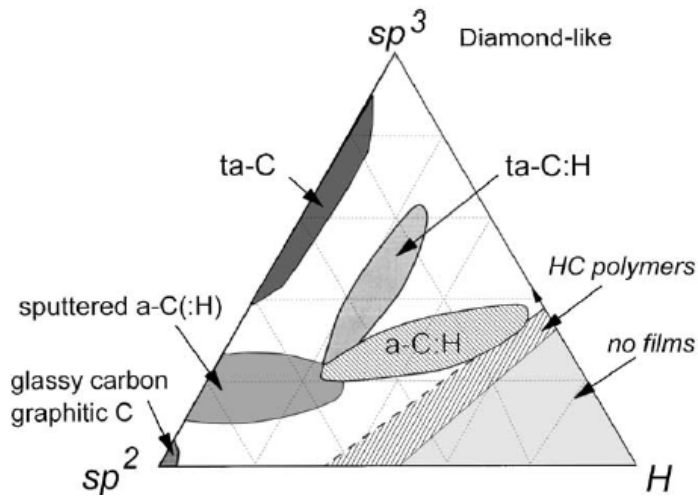


Figure 1.2. Ternary phase diagram of amorphous carbon-hydrogen materials [10].

In comparison to diamond coatings, DLC fabrication requires less processing time, hence it reduces the production costs. Furthermore, the fabrication of CVD diamond films necessitates very high temperatures and the surface roughness of the diamond coatings is usually higher in comparison with DLC. DLC has become commercially viable for industrial mass production as a result of these advantages [10].

1.2.2 Oxide based coatings

Oxides are a group of materials with a wide range of technological applications, for instance, in optics, semiconductor industry, tooling, etc. [14,15]. One of the most commonly used wear-resistant ceramic material is alumina (Al_2O_3). The coating properties of alumina depend significantly on the structure (amorphous, crystalline), which is highly influenced by the process parameters [16]. Thin chromium oxide layer (Cr_2O_3) can be applied as nucleation inter-layers (e.g., allowing alumina growth on some substrates) and in combination with other layers (CrN, for instance) to improve adhesion and tribological properties. Zirconium oxide (ZrO_2) coating has attracted considerable attention as a wear-resistant coating, due to useful combination of thermal, chemical and mechanical properties. As an example, a hard coating with an oxide layer used for dry machining is shown in Fig. 1.3.

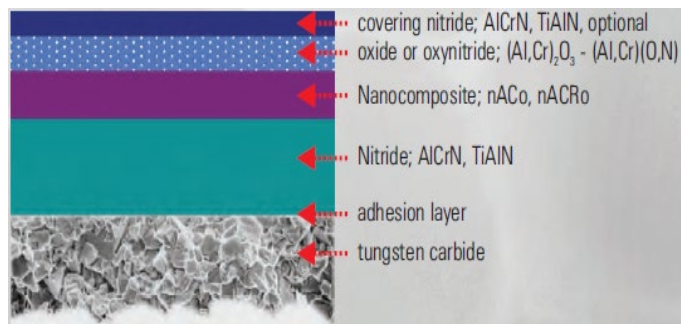


Figure 1.3. QUAD (PLATIT) coating with layered architecture including an oxide film [17].

Al_2O_3

Alumina exhibits many different metastable crystal structures. The most thermodynamically stable structure is the corundum phase denoted by α . The corundum structure is the most commonly sought phase of Al_2O_3 within the area of tool materials (coating or bulk) for metal cutting. Deposition of alumina is carried out in a selective environment by PVD and CVD methods. The transition of alumina phases with respect to the temperature is shown in Fig. 1.4. In stage I, the amorphous alumina layer grows during the low temperature oxidation [18]. When the temperature becomes sufficiently high, i.e., about 700 °C, the amorphous oxide transforms into γ -alumina (stage II), the density of γ -alumina exceeds that of amorphous alumina [19]. In stage III, the growth of γ - Al_2O_3 continues, for which the oxidation rate is limited by the inward grain boundary diffusion of oxygen anions [20,21]. Growth of the γ - Al_2O_3 layer can be accompanied by phase transformations into other transition polymorphs, such as δ - Al_2O_3 and θ - Al_2O_3 , which have densities very close to that of γ - Al_2O_3 [21]. The stable and denser α -alumina polymorph starts forming by the end of stage III; stage IV is considered to start when the oxide scale is completely transformed to α -alumina. Further research efforts were lately directed to prepare the corundum phase by the PVD methods at lower temperature [22].

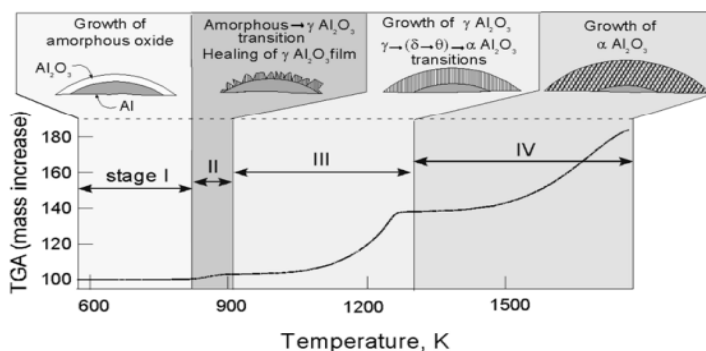


Figure 1.4. Phase transitions in alumina [23].

$(\text{Al}_{1-x}\text{Cr}_x)_2\text{O}_3$

The synthesis of $(\text{Al,Cr})_2\text{O}_3$ coatings by PVD can result in metastable cubic structures next to the thermodynamically stable and mechanically favorable corundum phase. The formation of $\text{fcc}-(\text{Al}_{1-x}\text{Cr}_x)_2\text{O}_3$ at the early stage of deposition at 550 °C after reaching the thickness of 2 μm reverts to the growth of the corundum structure $\alpha-(\text{Al}_{1-x}\text{Cr}_x)_2\text{O}_3$ [22]. Figure 1.5 shows the cubic (fcc) and corundum structures (α) of $(\text{Al}_{1-x}\text{Cr}_x)_2\text{O}_3$ [22]. The corundum phase offers particular potential for applications that require chemical inertness, thermal stability, mechanical strength, and good tribological properties at elevated temperatures. The lattice parameter of the metastable cubic $(\text{Al}_{1-x}\text{Cr}_x)_2\text{O}_3$ phase slightly varies with the chemical composition, as shown by Khatibi et al. and Alling et al. [24,25], Najafi et al. [22], and Diechle et al. [26]. The lattice parameter is smallest for the Al-rich and largest for the Cr-rich compositions.

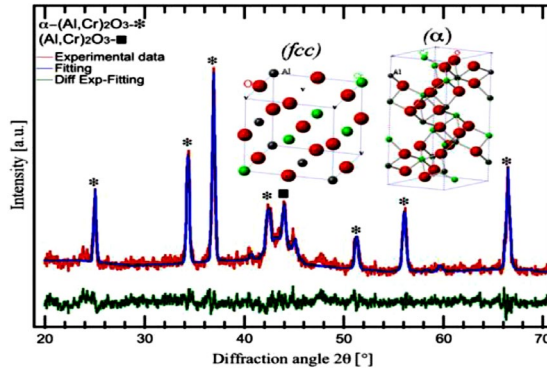


Figure 1.5. X-ray diffraction of the $(Al,Cr)_2O_3$ coatings with cubic (fcc) and Corundum (α) structures [22].

1.2.3 Hybrid coatings

Hybrid coatings systems were developed by combining in-situ and/or ex-situ deposition methods such as CVD and PVD. In comparison to conventional deposition methods, hybrid coatings have a significant impact due to their multifunctionality (counteract the many threats at once) and synergy (properties which cannot be obtained by standard methods) [27]. In the present PhD study, the hybrid coatings like $Al_2O_3/a-C:H:Si$ and Al_2O_3/NCD were prepared with the help of different types of deposition methods, such as PVD, PACVD and ALD. ALD is a CVD technique where gaseous reactants (precursors) are introduced into the chamber to prepare the desired material via chemical surface reactions. Figure 1.6 shows different methods of surface treatment in a multi-step process, i.e., the hybrid technology can be configured in a variety of ways.

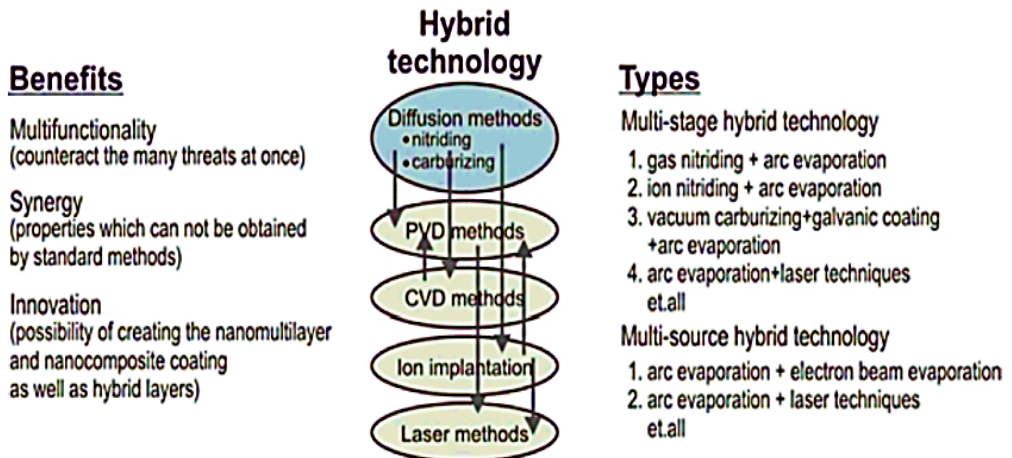


Figure 1.6. Hybrid technologies for hard coating preparation [27].

1.3 Coating generations

There are four coating generations defined by Platit [17]. The first generation of the coating was a single layer (monoblock) structure without the adhesion layer, for instance TiN, CrN (Fig. 1.7a). The second generation of the coating structure arrived with adhesion layer support for monoblock, gradient, multilayer, nanolayers and nanocomposite structures (Fig. 1.7b).

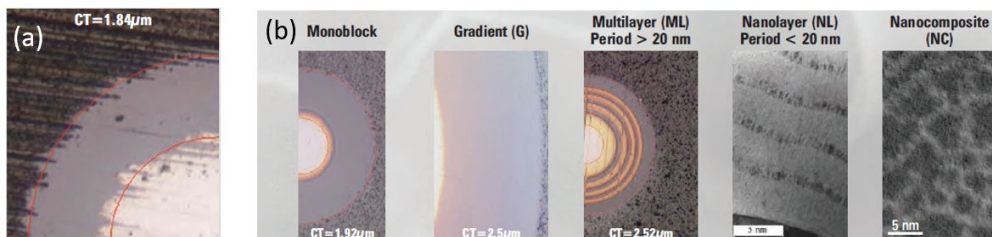


Figure 1.7. Calo-tests of the PVD hard coating structure. The (a) 1st and (b) 2nd generation of coatings [15].

The 3rd generation of triple coatings^{3®} PLATIT consists of an adhesion layer, a core layer (monoblock or gradient) and a nanocomposite top layer; it has the advantages of conventional (TiN, CrN, TiAlN, AlTiN, gradient) coatings and of nanocomposite coatings (nc-TiAlN/a-SiN, nc-AlCrN/a-SiN, nc AlTiCrN/a-SiN) [28]. This generation is applicable for general purpose use, but particularly for high performance cutting tools (Fig. 1.8a).

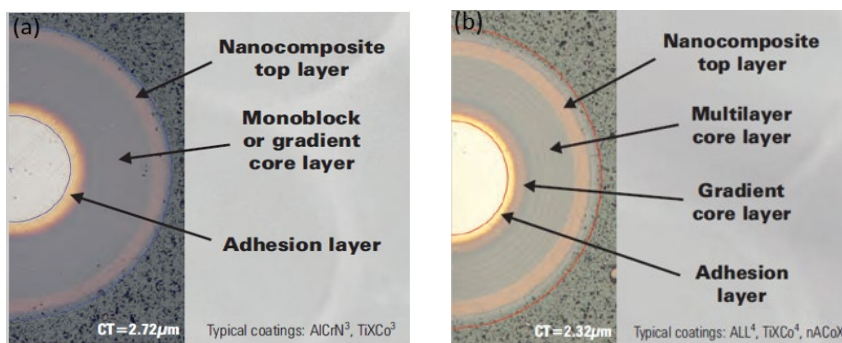


Figure 1.8. Calo-tests of the PVD hard coating structure: (a) 3rd and (b) 4th generations [17].

The 4th generation is QUAD coatings^{4®}, which is a combination of gradient, multilayer, oxide and nanocomposite layers to make them durable under harsh conditions [29]. Figure 1.8b shows the QUAD coating structure. In the present PhD study, the Platit π411 unit was used to produce QUAD HMC, see also Fig. 1.3.

1.4 Fundamentals of coating tribology

The principles of friction, wear and lubrication are the main objectives of tribological studies. All mechanical systems with moving components in contact with one another experience friction and wear. Due to excessive energy consumption and progressive material loss, these phenomena are largely responsible for the degradation of system reliability and performance. In this regard, significant efforts have been made to employ effective methods to reduce the wear and optimize CoF [8-10]. By definition, in the case of the super low friction,

the CoF value is < 0.01 [30]. The preparation of coatings that exhibit low wear and appropriate CoF value over a wider range of aggressive conditions (temperature, atmosphere, irradiation, etc.) is a challenge in modern industrial tribological systems.

1.4.1 Wear and friction mechanisms

The wear and friction are multiscale phenomena and related mechanisms can be considered on different size scales, i.e., nano, micro and macro scales. For instance, Hertzian contact pressure is calculated on the macro level, i.e., mm. Different processes occur on the micro level of asperities within the tribological contact. The composition of the outermost surface layer and properties are changed by chemical reactions (nanoscale) that occur at the surfaces during sliding as well.

Figure 1.9 shows the main tribological contact conditions [31,32]. In addition to sliding, the other kinds are abrasion where a hard sharp counterface ploughs in the surface; fatigue where a load is continuously repeated; impact where a dynamic load is applied, fretting where the movement is reciprocating with a small amplitude; chemical dissolution where high temperatures can induce mutual solubility at the surface, and corrosion where the contact is within a corrosive medium or environment. These may also be augmented by lubrication if an external fluid is introduced into the contact.

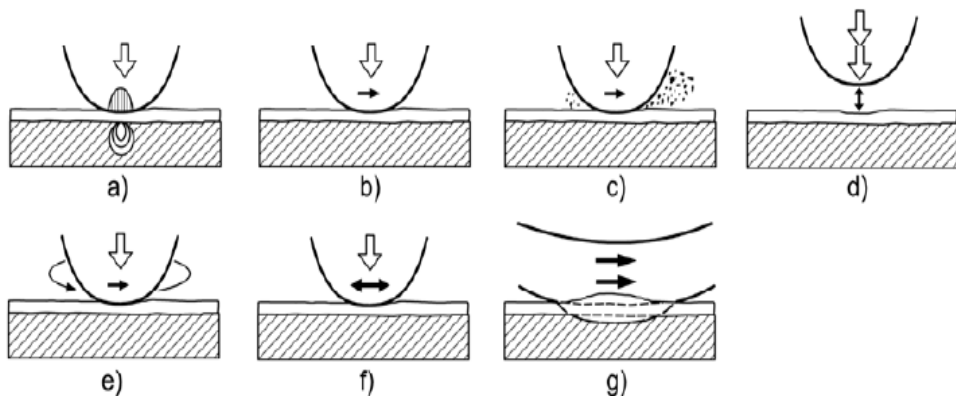


Figure 1.9. Typical contact conditions in tribological applications of coated surfaces: (a) contact stresses at normal load, (b) sliding, (c) abrasion, (d) impact, (e) surface fatigue, (f) fretting, and (g) chemical dissolution [29].

The different categories of wear mechanisms can be generalized in two groups, namely mechanical wear mechanisms and physical and chemical wear mechanisms [31].

Mechanical wear mechanisms cover such phenomena as:

- **Micro-ploughing:** abrasion, erosion etc., whereby micro asperities of the material are formed through ploughing of a harder surface (or 3rd body) in a softer surface.
- **Extraction:** due to the local cohesive strength of the material, the wear particles are formed by being pulled out (extract) from the surface.
- **Plastic deformation/compaction:** volume is lost locally by the material on the surface during the plastically deformed and compacted within the contact region or spread away from it.

Physical and chemical wear mechanisms are generalized as:

- **Physical wear:** volume lost due to dissolution, diffusion, and evaporation.

- **Chemical wear:** during the chemical reaction, the volume is lost, such as oxidation in the material leads to subsequent loss of the material.

In practice, the tribo-pair encounters different combinations of the abovementioned mechanisms during the course of the wear process.

1.4.2 Solid lubrication

Solid lubricating materials have been employed by industries for a long time to achieve low friction and wear under different conditions. These materials, despite being in the solid state, form a tribofilm leading to improved wear resistance and friction reduction [33,34]. Solid lubricants are widely used to overcome frictional/wear problems in high vacuum and variable temperature environments because they do not evaporate under high vacuum and result in relatively small changes in the physical and chemical properties in response to large variations in temperature.

Some soft metals like Cu, Ag, Sn and Au are used on sliding surfaces as lubricant additives or as soft metallic films for providing low friction coefficients due to their low shear strength [35,36]. MoS₂ is a layered material employed as a solid lubricant and can considerably reduce the CoF value at HT [37]. Carbon based materials have generated strong interest due to their outstanding physical, mechanical, biomedical, and tribological properties [38]. Carbon forms different allotropies and the properties of each form depend on its unique structure [39]. The trends of solid-lubricating materials are illustrated in Fig. 1.10 [40].

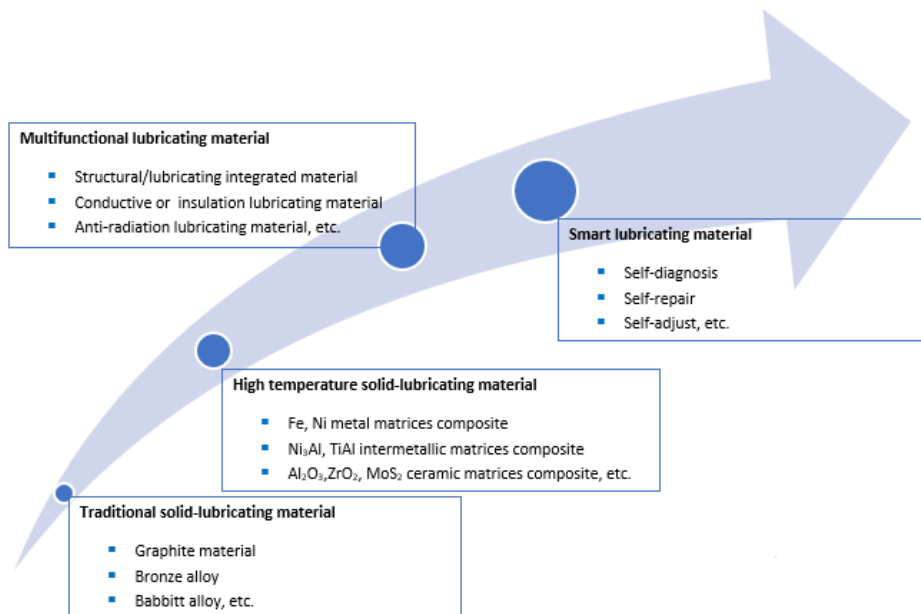


Figure 1.10. Trends of solid-lubricating materials [40].

There has been considerable progress in the development of high temperature solid-lubricating coatings. Initially, high temperature solid-lubricating coatings contained a single-phase solid lubricant or a monolithic component. However, at elevated temperatures, in the case of a single-phase solid lubricant, the simultaneous maintenance of low friction and wear is non-trivial. Therefore, structural integrated materials were developed.

The temperature adaptive behavior involves complex chemical-physical structural evolution of the contact surface [41,42]. Due these evolutions, the tribo-system tends toward

formation of low friction and wear contact conditions for an effective adaptive mechanism. There are several conditions that can generate adaptive behavior [43], such as:

- i. Temperature activated diffusion of metal lubricants to the surface
- ii. Temperature and environment activated formation of lubricious oxide phases
- iii. Temperature and strain actuated structural evolutions in the contact

In the present study, formation of lubricious oxide phases and structural evolutions in the contact were observed and investigated.

By means of advanced manufacturing technology, high temperature solid-lubricating materials possessing self-diagnosis with self-repairing properties following can be prepared.

1.4.3 Self-organization and self-organized criticality

Friction is a complex phenomenon that could be considered as an irreversible nonequilibrium process. This process may leap either into chaos or greater complexity and stability due to self-organization with dissipative structures formation [44,45]. To use the approach of nonequilibrium thermodynamic [46,47], some generic features of friction should be outlined. Wear can vary over a wide range of magnitudes; a large variety of different wear mechanisms exist, but wear is a fundamental characteristic of friction for any tribo-system. The other generic characteristic of friction is the formation of tribo-films or secondary (i.e., formed during friction) structures on the surface [48]. Friction is an irreversible process because energy dissipation takes place [49]. The driving force of self-organization is that the open systems tend to protect and stabilize themselves. This could be related to the decrease in entropy production during nonequilibrium processes. As dissipative structures generated during self-organization, tribo-films are dynamic surface spatial structures with temporal behavior. As tribo-films form in situ during friction, they became originally known as 'secondary structures' [48]. Such structures demonstrate the adaptive behavior of the complex tribo-system. During friction, these tribo-films are produced on the base surface of the engineered material through structural modification and interaction with the environment [50-60]. The entropy production rate reaches its minimum in the self-organized state. Therefore, the self-organization is usually beneficial for the tribological system, as it leads to the reduction of friction and wear [60-62].

The relation between the self-organization and the wear mechanism in diamond films was investigated in our group [2]. The probability of self-organization to occur can be described by Eq. (1.1), where Y is the probability of loss of thermodynamic stability (or the probability of self-organization) and n is the number of the interrelated processes (humidity, temperature, etc.) in the tribo-system [2]:

$$Y = 1 - \frac{1}{2^n} \quad (1.1)$$

Self-organized criticality is a critical point at which a system radically changes its behavior or structure and shows avalanche-like behavior [63]. In general, the process is characterized by a high instability due to complexity. Self-organized criticality could be associated with the stick-slip phenomenon during friction that is similar to avalanche-like behavior [64,65]. The stick-slip phenomenon is typical in the cutting process while the chip slides along the rake surface of the tool [66,67].

1.5 Aim and objectives of thesis

The overall aim of this study is to protect the coatings (carbon based and hard coatings) from catastrophic failure due to atmospheric oxidation attack during operations and preserve excellent tribological properties of coatings, particularly, under high temperature conditions.

Objectives of the study:

- To enhance the tribological properties of amorphous carbon coating (a-C:H:Si) by using thin alumina layer.
- To understand the occurrence of the adaptive and superlubricating effects due to a thin alumina layer.
- To understand the mechanisms of friction and wear of hard multilayers coatings (HMS) at high temperature during sliding.
- To understand the plastic deformation (coating deflection) in a-C:H:Si and HMC.
- To understand the transition from self-organized criticality to self-organization on NCD coatings during sliding.

2 Materials and methods

2.1 Deposition techniques

The following different types of coatings were prepared by means of various deposition methods:

- i. Diamond like carbon a-C:H:Si coatings were deposited by the PACVD method.
- ii. Alumina (Al_2O_3) layers were deposited by the ALD method.
- iii. NCD films were deposited by the PACVD method.
- iv. Hard coatings (adhesive layer and HMC) were deposited by the PVD method.

Coating deposition procedures are explained in the attached publications, see Appendix.

2.2 Sliding tests

The friction and wear were investigated by means of a CERT UMT-2 Bruker® tribometer. The reciprocating unidirectional and rotatory sliding tests were carried out to evaluate the coating properties. High-temperature chamber with a rotation drive (S21ME 1000) was used for the sliding tests at HT. Si_3N_4 and Al_2O_3 balls (REDHILL, Czech Republic) were selected as a counterbody for carbon-based and HMC. Table 2.1 presents the conditions and parameters of the tests carried out to analyze the friction and wear behavior of coatings.

The volume of the wear scar (V) was estimated using Eq. (2.1), where S is the cross-section area and l is the length of the wear scar:

$$V = S \cdot l \quad (2.1)$$

Table 2.1. Specimens and parameters of tribo-tests.

Types of coatings	NCD	HMC	a-C:H:Si	Al ₂ O ₃ / a-C:H:Si
Substrate	SCD (110)	WC-Co		
Thickness (μm)	2.2, 8, 10.5, 14 and 22.5	3.6	1	1.2
Counter body (mm)	Si ₃ N ₄ , ∅ 3	Al ₂ O ₃ , ∅ 6	Si ₃ N ₄ , ∅ 10	
Temperature (°C)	RT	RT, 600 and 800	RT and 400	
Methods	Reciprocating Unidirectional	Rotatory		
Normal Load Force (N)	0.5 – 2	10	2	
Radius of wear scar (mm)	-	4	1.5	
Length of wear scar (mm)	1	-	-	
Velocity v (rpm)	300	300	200	
Duration N (cycles)	3000, 6000, 9000, 36000, 72000	54000	36000	

2.3 Nanoindentation and nanoscratch

The mechanical properties of coatings were determined by the nano-mechanical testing system (NanoTest, Micro Materials Ltd.). The nanoindentation tests were performed with the Berkovich diamond indenter and nanoscratch tests were carried out with a sphero-conical diamond indenter with a radius of 5 μm . The schematic of nano tests is shown in Fig. 2.1. The progressive loading method was adopted for nanoindentation tests within the range of 0.2-0.45 mN of load with the increment of 0.05 mN.

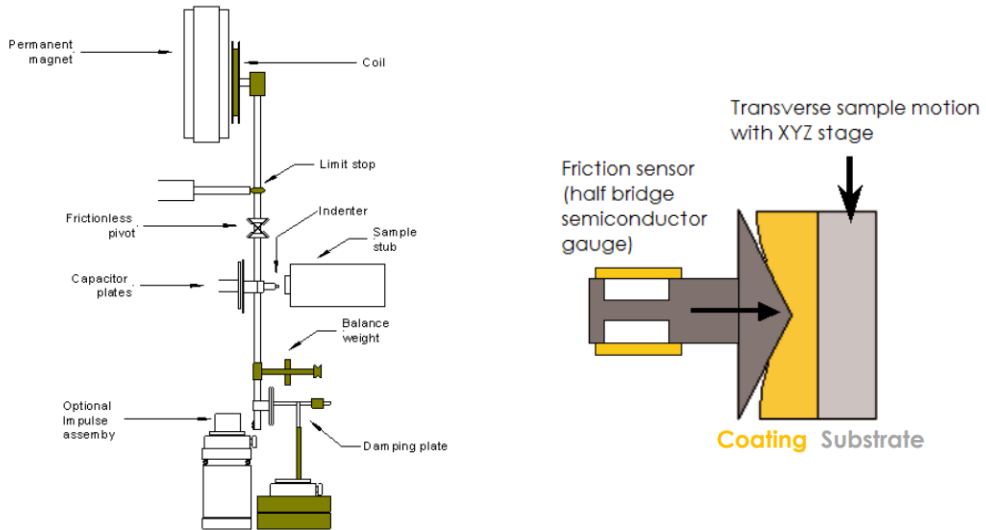


Figure 2.1. Schematic view of NanoTest Micro-Materials® equipment for (a) nanoindentation and (b) nanoscratch.

The hardness and Young's modulus were estimated using the Oliver-Pharr method [68]. The nanohardness was calculated using Eq. (2.2), where H – hardness, P_{max} – maximum load and A_r – the indentation area. The Young's modulus was evaluated with Eq. (2.3), where E_r – reduced modulus, ν_i and ν_s – Poisson's ratio and E_1 and E_2 – Young's modulus of diamond indenter and films:

$$H = \frac{P_{\text{max}}}{A_r} \quad (2.2)$$

$$\frac{1}{E} = \frac{1-\nu_i^2}{E_1} + \frac{1-\nu_s^2}{E_2} \quad (2.3)$$

The nanoscratch tests were carried out in the Z direction with a friction sensor attached. All tests were performed as multi-pass experiments (3 scans: topography–scratch–topography) that were subsequently analyzed using NanoTest software. The load was applied after scanning the distance of 50 μm , with the following progressive load with a loading rate of 5 mN/s up to reaching the peak load value.

2.4 Characterization methods

The coatings were characterized by using conventional and high-temperature X-ray diffraction methods to analyze the crystal structures, Micro-Raman spectroscopy was used to analyze the bonding structure of coatings, X-ray photoelectron spectroscopy (XPS) was used to investigate the surface chemical composition, scanning electron microscopy (SEM) was used to analyze the chemical structure and the surface morphology of the pristine and wear scars surfaces and mechanical profilometry was used to analyze the wear scar profiles and wear volume estimation.

3 Results and discussion

3.1 Investigation of thin alumina layers prepared on Si(100) substrate

Surface morphology and structure

Alumina films with a thickness of 100 nm were deposited on the Si(100) substrate with the ALD technique. The deposited samples were annealed at different temperatures and times. Their properties were analyzed by means of nanoindentation and nanoscratch tests and compared with as-deposited samples and the Si(100) substrate. Table 3.1 shows the annealing parameters of alumina films.

Table 3.1. Post deposition annealing parameters of alumina films.

Samples	1 (as-deposited)	2	3	4	5	6
Temperature (°C)	-	500	700	900	1100	1100
Time (h)	-	1	1	1	2	3

The surface morphology was investigated by SEM, alumina layer (sample 1) is uniform and smooth (Fig. 3.1a). A similar morphology was found for the samples annealed up to 900 °C. The formation of irregular patterns of holes in films was observed for the samples annealed at 1100 °C, see Fig. 3.1b. The X-ray diffraction (XRD) patterns taken on samples 5 and 6 indicate the formation of a crystalline structure after 2 h of annealing at 1100 °C (Fig. 3.2). Based on the study of literature, the most likely gamma and delta (γ , δ) alumina were formed [69]. The crystal structure of samples 1–4 was amorphous.

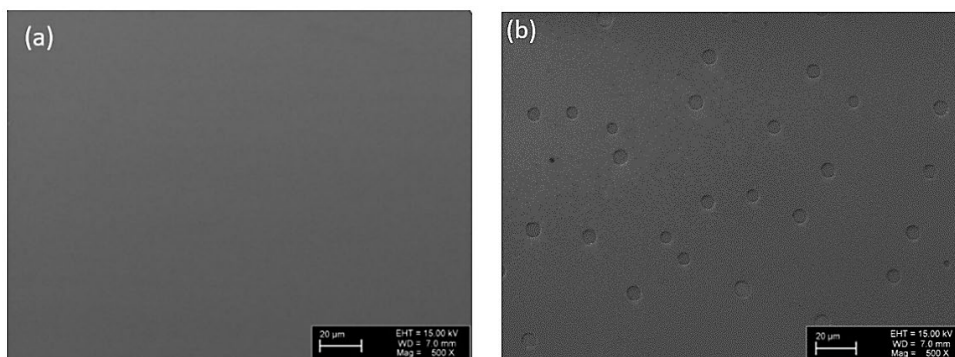


Figure 3.1. SEM images of alumina films (a) as deposited and (b) annealed at 1100 °C for 3 h.

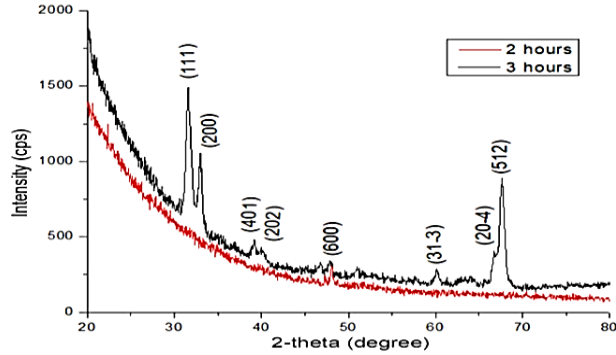


Figure 3.2. XRD patterns of samples 5 and 6 after 2 and 3 hours of annealing at 1100 °C.

Nanoindentation and nanoscratch

The mechanical properties such as hardness and Young's modulus of 100 nm thin alumina film and Si substrate were evaluated by the nanoindentation and nanoscratch methods. The nanohardness and Young's modulus of the Si(100) were in the range of 10.6-13.2 GPa and 142-169 GPa, which is in good agreement with the literature [70]. The nanohardness and Young's modulus of as-deposited and annealed alumina films were in the range of 10-13 GPa and 150-190 GPa, which is in agreement with a previous study [71].

The alumina layer adhesion was evaluated using a nanoscratch test. The nanoscratch tests on the Si(100) substrate with a spherical indenter upon progressive loading were carried out by Beake et al. [72]. Initially, the nanoscratch tests were performed on the Si(100) substrate to determine the friction and scratching behavior of the substrate and then on alumina films to analyze the film properties and to understand the influence of the substrate. The results of the scratch tests with optical microscopy images of the scratch scars are shown in Fig. 3.3 a-c. The scratch tests on the Si(100) substrate and alumina were performed at the peak loads up to 400 mN. The results of the scratch tests on the Si(100) substrate are in good agreement with literature [72]. The main transitions on the Si(100) and alumina films are as follows: Ly – onset of non-elastic deformation, Lc1 – pop-in observed by an accompanied change in the color of the scratch track and Lc2 – prominent chipping observed at the edges of the track. The nanoscratch behavior of as-deposited alumina film (sample 1) is shown in Fig. 3.3b. The Lc1 transition starts at 48 mN and chipping starts at Lc2 = 78 mN. The response of the annealed at 1100 °C Al₂O₃ film (sample 6) is shown in Fig. 3.3c. No clear Lc1 transition was observed and chipping starts at Lc2 = 89 mN. There is a good correlation between the Lc2 values observed on alumina films (as deposited and annealed) with the value of 63 mN (Lc1) observed on Si(100), i.e., when severe deformation starts within the Si(100) substrate. It shows the influence of the substrate on the properties of alumina films.

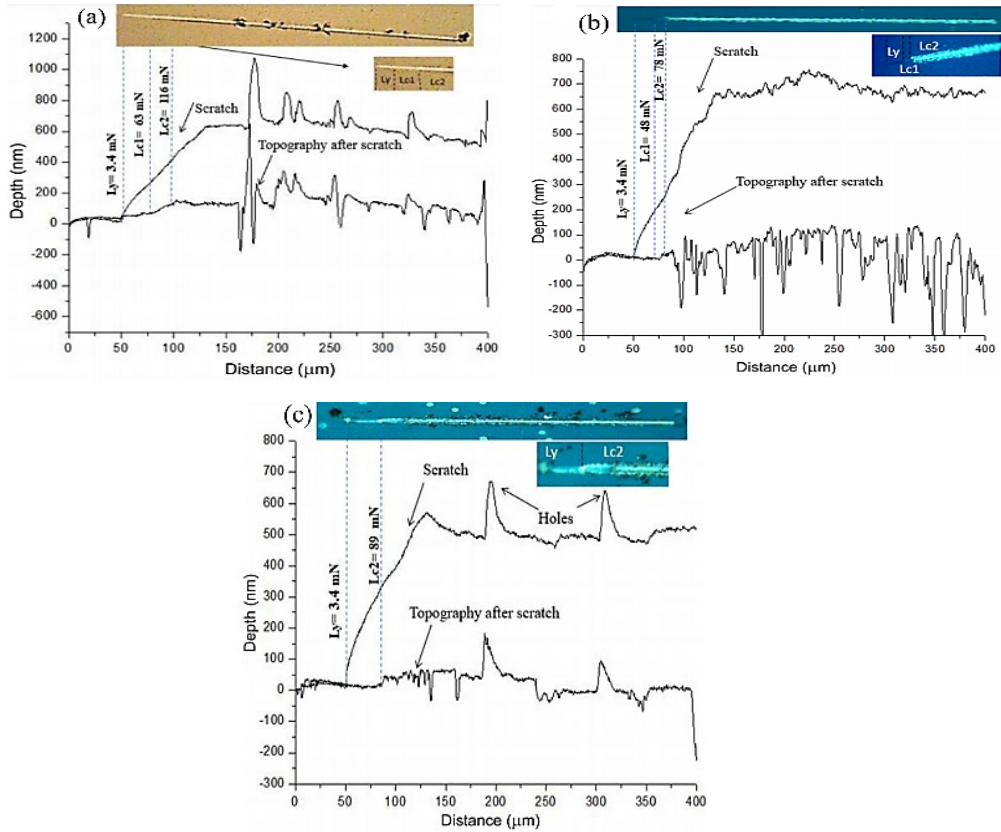


Figure 3.3. Scratch tests at the peak load of 200 mN with optical images for (a) Si(100) substrate, (b) as-deposited alumina film (sample 1) and (c) annealed alumina film (sample 6).

Figure 3.4 shows the CoF value versus the normal load measured in nanoscratch tests. The CoF value increases for alumina and Si(100) within stage 1, which is in a disagreement with Amontons' law of friction in Eq. (3.1), where F_x – the friction force, k – coefficient of friction and F_z – is the normal load. The CoF is the coefficient of proportionality and it is independent of the load [73].

$$F_x = kF_z \quad (3.1)$$

The elastic as well as plastic deformation dominate at stage 1. Most likely, the CoF value changes due to the mainly continuous change of the elastic – plastic behavior of the Si(100) substrate. Therefore, contact conditions between the indenter and the sample surface changed continuously as well. However, for stage 2, the CoF values were nearly constant; such behavior shows agreement with the law of friction, see Eq. (3.1).

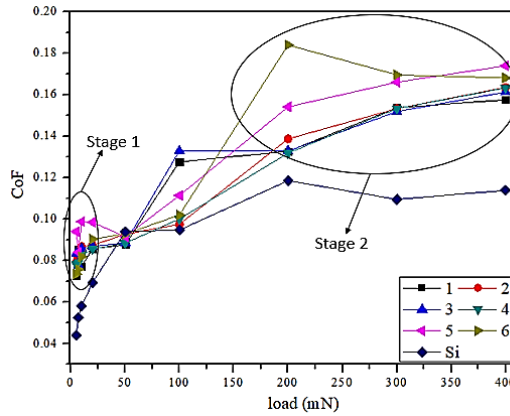


Figure 3.4. CoF versus load.

Conclusions

Nanoindentation and nanoscratch tests were performed to evaluate the mechanical and tribological properties of thin alumina films deposited on Si(100) substrates. The measurements of hardness and Young's modulus of Al₂O₃ thin films were influenced by the Si substrate. The amorphous alumina changed into crystalline structure after annealing at 1100 °C. Disagreement with Amontons' law of friction was found for the loads in the range of 5–20 mN, which probably corresponds to a continuous change from elastic to plastic deformations within the Si substrate. However, for the higher loads (200–400 mN), a good agreement was found with Amontons' law.

3.2 Self-organized criticality on nanocrystalline diamond

Complex behavior can develop spontaneously in certain nonequilibrium systems with many-body interactions. These systems are complex in the sense that there is not a single time or spatial scale characterizing the system behavior, but the statistical properties are well described by simple power laws [74].

The tribological system is a complex system that is controlled by a number of processes, including deformation and fracture of surface asperities, abrasion, adhesion, oxidation, fatigue, tribolayer formation, etc. These processes contribute to friction at different scales (nano-, micro- and macroscale) and hierarchy levels (molecular, surface asperity, component) [75]. Due to the complexity, the friction process is not firmly linear, the CoF can depend on a variety of factors including applied load.

The energy (W) induced by external loading (mechanical work) is accumulated into the tribo-system (ΔE) and converted into the heat (Q):

$$W = Q + \Delta E \quad (3.2)$$

Entropy production ($\partial S/\partial t$) is a useful concept for the characterization of friction and wear, which are dissipative and irreversible processes. The entropy production of a system is the sum of the entropy production of processes occurring within the system. Moreover, according to the second law of thermodynamics, it is impossible to distinguish a part of the system at the macro-, micro- or nanoscale, in which the entropy production would be negative [76]. The net entropy production can be written as the sum of entropy production at different length scales, as shown in Eq. (3.3) [77-79]:

$$\frac{d_i S}{dt} = \sum n \frac{d_i S_{n \text{ micro}}}{dt} = \sum n \frac{d_i S_{n \text{ nano}}}{dt} \quad (3.3)$$

According to Prigogine, the stability conditions for the thermodynamic system can be analyzed using the Lyapunov's function $\partial^2 S$ (where $\partial^2 S$ is the second variation of entropy). Self-organization can occur in the system if inequality is not fulfilled in Eq. (3.4) [80-82].

$$\frac{\partial}{\partial t} (\partial^2 S) \geq 0 \quad (3.4)$$

SO is often characterized in the tribo-system by the formation of a thin tribo-layer at the surface within the contact that reduces the wear and the CoF [81].

Experimental and theoretical studies show that there are systems with many degrees of freedom, which can evolve into a self-organized critical (SOC) state. This state is characterized by the release of energy through rapid relaxation processes (avalanches), as shown in Eq. (3.5). The relation between the avalanche size (A) and the number of avalanches of the same size (n) can be described by the power law:

$$n = A^{-\mu} \quad (3.5)$$

where μ is an exponent characterizing the distribution of avalanches with different sizes [82-84]. A well-known example of the SOC system is a sand pile model [85] where grains of sand are randomly placed into a pile until the slope reaches a critical value. Further addition of grains triggers an avalanche affecting adjacent grains. It is a state that unlike SO systems, SOC systems are constantly "tuned" to a state whereby an avalanche can be initiated again [86]. Another example of the SOC system is a stick-slip friction between rubbing surfaces [81-86]. An indication of SOC is the power-law distribution of friction force drops (dFx) in tribological tests [84]. Some authors suggest strengthening conditions for SOC, namely the presence of frequency power spectra of Fx time series and the existence of stationary state at long times [65,87].

The NCD films of different thickness (different roughness) were used as shown in Tables 2.1 and 3.2. The SOC behavior was estimated using the distribution of friction force (Fx) drops (dFx) during the reciprocating sliding tests. The behavior of Fx is shown in Fig. 3.5.

Table 3.2. Thickness and surface roughness of samples used in the tribological tests.

Sample	n4	n5	n6	n7	n2	n3	n9	n8
Coating thickness (μm)	2.2		8		10.5		14	22.5
Roughness Sq(μm)	33		55		56		66	78

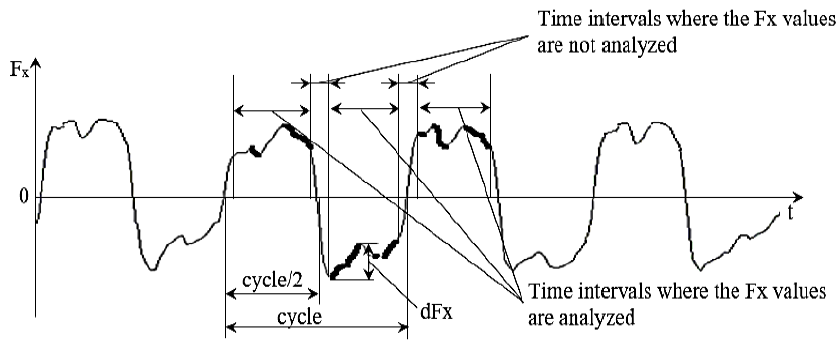


Figure 3.5. Example of friction force (F_x) behavior in the reciprocating sliding test and data selection.

The CoF versus time curves with different sliding times duration for the NCD film with a thickness of $10.5 \mu\text{m}$ is shown in Fig. 3.6a,b. The two types of CoF vs time curves behavior during the sliding on diamond films at RT were observed in our previous studies, see discussion in our publication [2]. The CoF values during the first 800 sec of sliding indicate the friction instabilities during the early stage of the run-in period.

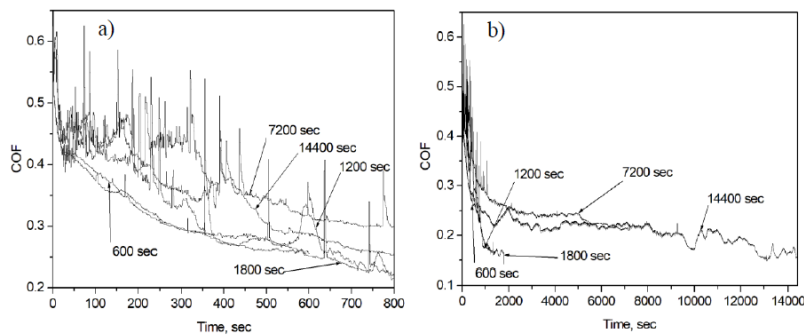


Figure 3.6. CoF versus time curves for NCD with $10.5 \mu\text{m}$ of thickness. Test duration is 600, 1200, 1800, 7200 and 14,400 sec: (a) first 800 sec run-in period (b) and full-length.

The distinctive aspects of F_x value during the reciprocating cycles are shown in Fig. 3.7a,b. The F_x peaks of each half cycle have two peaks at the beginning and at the end. The peak at the beginning is due to the fact that the coefficient of static friction is always greater than the coefficient of sliding friction. In most cases, the height of peak 1 is smaller as compared to peak 2. During the initial run-in period, the height of both the peaks is high, i.e., for the first 0-600 sec of sliding, as shown in Fig. 3.7a. The height of peaks reduces with respect to the sliding time, for a longer period of sliding, the peaks height became approximately constants, as seen after sliding of 1800 sec in (Fig. 3.7b). Due to the stick-slip motion, the values of F_x varied with sliding.

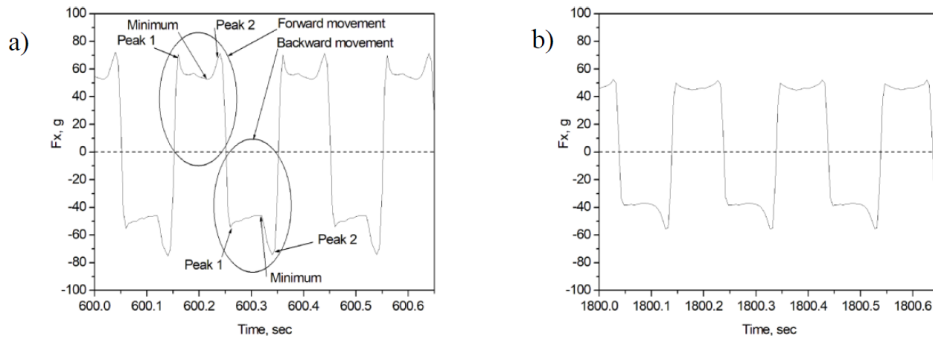


Figure 3.7. The F_x vs. time curves after the sliding test at 2 N of load: (a) 600 sec and (b) 1800 sec of NCD coating with 10.5 μm thickness.

The dF_x distributions are shown in Fig. 3.8. The mean and median of dF_x distributions are higher at 2 N of the load in comparison with 0.5 N (Fig. 3.8b). This could indicate the existence of a threshold in the stick-slip system, which resembles the threshold for a sand pile slope angle in the “sand pile model” when a sudden avalanche occurred [86].

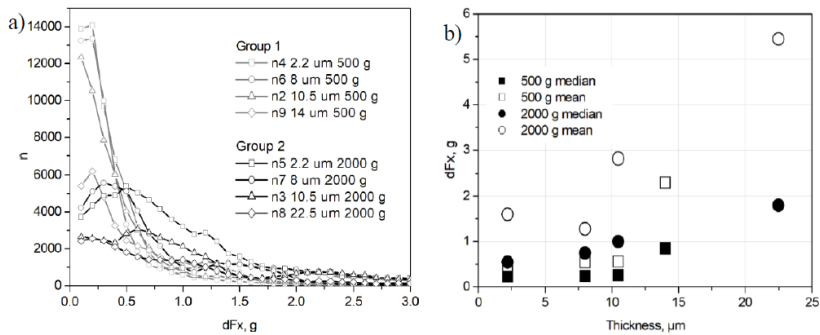


Figure 3.8. (a) Distributions of dF_x obtained for the first 600 sec of the 1800 sec tests and (b) median and mean values of the same distributions.

The F_x drops, dF_x , distributions were estimated for different periods of sliding tests. The log-log behavior of dF_x distributions for coatings with thicknesses of 2.2 μm and 10.5 μm are shown in Fig. 3.9a,c. The log-log behavior for NCD films shows linearity for initial running period specifically (0-600 sec), i.e., it follows the power-law distribution $f^{-\mu}$ with the exponent μ . The μ varied in the range of 0.6-2.9, which indicates the presence of SOC at the initial stage of the run-in period during dry sliding on the nanocrystalline diamond against Si_3N_4 ball. The log-log distribution of dF_x for other time intervals of the sliding tests does not follow the power-law behavior, as shown in Fig. 3.9b,d.

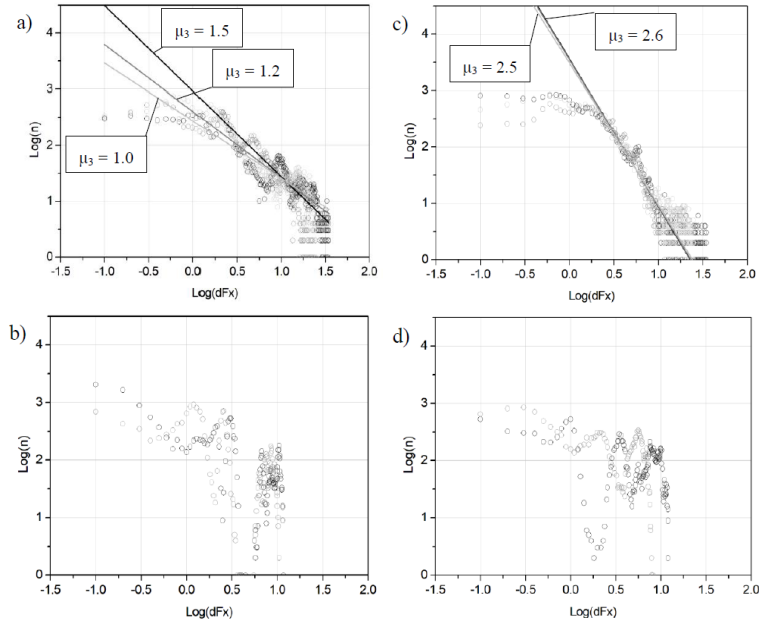


Figure 3.9. Log-log distributions of dFx for 10.5 and 2.2 μm thick NCD films: (a) 0-600 sec, (b) 6600-7200 sec, (c) 0-600 sec and (d) 6600-7200 sec. The data were obtained after 1800, 7200 and 14,400 sec tests with 2 N of load.

The averaged exponent μ for the initial run-in period is shown in Fig. 3.10. The μ value decreases with respect to coating thickness. The roughness of thicker films is higher than that of the thinner film (Table 3.2). The value of the friction drop dFx increases with increasing of film thickness (Fig. 3.8b). In other words, mechanical interlocking between counter body asperities and the NCD film is a crucial aspect for the understanding of SOC, which is in agreement with the conclusion by Zypman et al. [65].

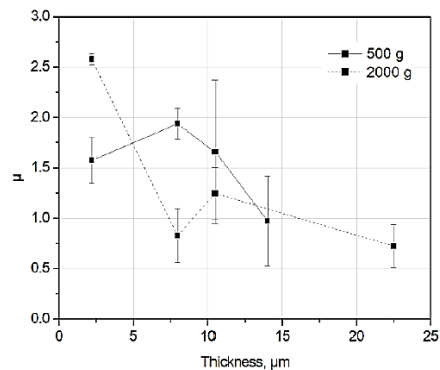


Figure 3.10. Averaged exponent μ vs. coating thickness for the run-in period (0-600 sec).

Figure 3.11 shows SEM images taken of the pristine and the wear scars after the sliding tests on sample n3. The duration of the tests varied between 600 and 14,400 sec, and the normal load was 2 N. A network of ripples was observed within the wear scar after the first 600 sec of sliding and for all the following stages of the sliding regardless of the test duration. Neither fragmentation of the network into isolated ripples nor disappearance of ripples was

found. Formation of some ripples on top of the surface asperities can probably be expected before 600 sec of sliding as well. Smoothing of the NCD surface and formation of the continuous network of ripples on the surface was found after 1800 sec of sliding (Fig. 3.11d). The test duration influences the shape and density of the ripples, as revealed, for instance, when comparing Fig. 3.11c and Fig. 3.11f. It is worth stressing that the formation of ripple patterns is a continuous process, i.e., new patterns are continuously formed in the course of the increase of the wear scar depth. In other words, there is a transition from SOC to SO during the initial run-in period (0-600 sec).

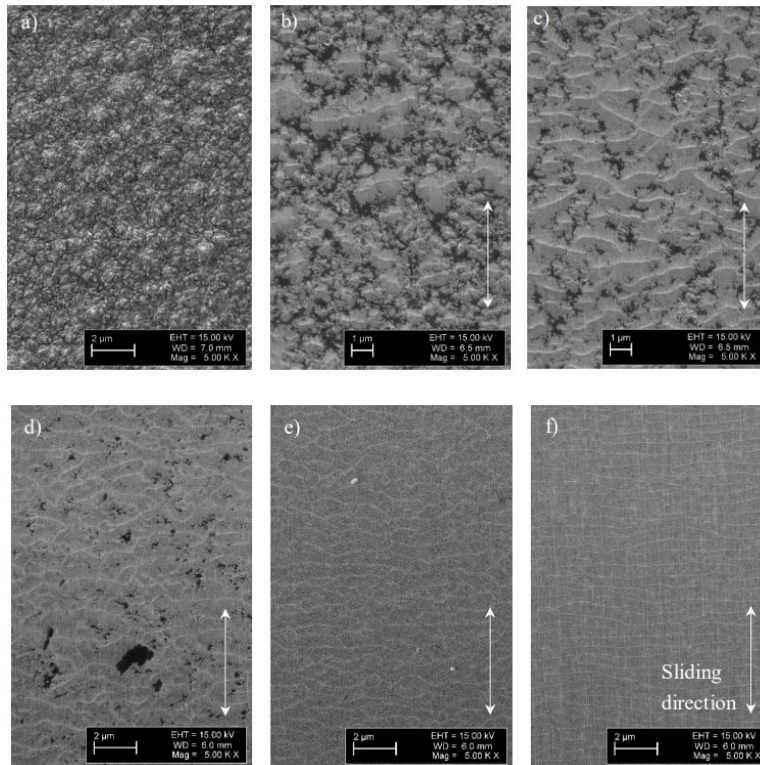


Figure 3.11. Surface morphology and ripple patterns observed within wear scars after the varying sliding time on sample n3: (a) pristine surface, (b) 600, (c) 1200, (d) 1800, (e) 7200 and (f) 14,400 sec.

The SOC and SO can be distinguished by a different way of releasing mechanical energy induced by external work. SOC is related to the process of energy release through the avalanches; however, dissipation of energy through the formation of tribolayer, ripples formation, etc. on the surface occurs in the case of SO.

Conclusions

The distributions of friction force drops dF_x during reciprocating sliding on NCD/SCD(110) samples against Si_3N_4 balls were analyzed. The power-law type of friction force drops distribution was observed at the initial run-in period of the sliding tests, i.e., during the first 600 sec of sliding. This indicates the presence of SOC. The formation of dissipative structures starts during the later stages of the run-in period, i.e., SOC continuously changes into SO. The SOC was not found during the steady-state regime of sliding with an exception for periods where instabilities in sliding occurred.

3.3 Tribological behavior of hard multilayer coatings

Surface morphology and structure

The SEM image of pristine surface and schematic drawing of the hard multilayer coating (HMC) are shown in Fig. 3.12a,b. The pristine surface contains spherical and shapeless microdroplets with surface cavities (Fig. 3.12a). The high temperature X-ray diffraction (HT-XRD) was performed between RT to 1200 °C with an interval of 100 °C, the HT-XRD patterns are shown in Fig. 3.13. The patterns taken from RT to 700 °C show no significant difference in crystal structure.

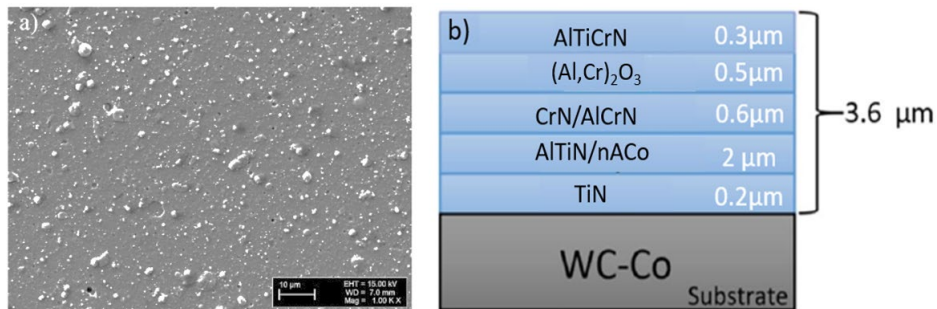


Figure 3.12. (a) The pristine surface morphology of HMC and (b) schematic of hard multilayer coating.

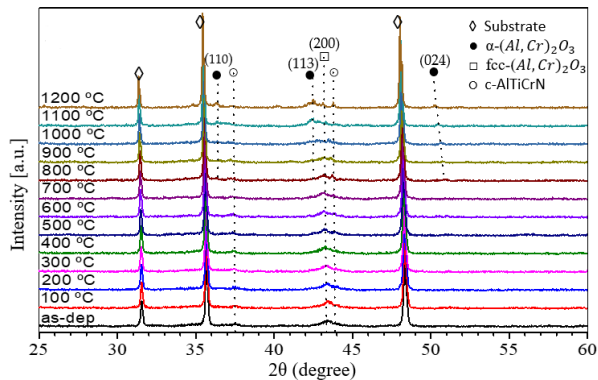


Figure 3.13. HT-XRD patterns taken on HMC.

The XRD peaks correspond to fcc-(Al,Cr)₂O₃, WC-Co and c-AlTiCrN phases up to 700 °C. The α-(Al,Cr)₂O₃ phase appears first at 800 °C and the intensity of the corresponding peaks increases with respect to the temperature, which indicates the phase transition from fcc-(Al,Cr)₂O₃ to α-(Al,Cr)₂O₃ [22,24].

Friction and wear

The CoF behavior was investigated at 10 N of load against an alumina ball (Table 2.1). The CoF vs cycles curves are shown in Fig. 3.14. The CoF value in the sliding test performed at RT shows steady state behavior during the course of the test. The initial and final CoF values are approximately equal to 0.7. The initial running-in period was observed for the tribo-tests at 600 °C and 800 °C. The CoF is about 0.9 at the beginning of the test at 600 °C. The run-in period is approximately 10,000 cycles. After run-in, CoF value drops to 0.6 and is stabilized until 35,000 cycles with the CoF value equal to 0.6 and then increases to 0.7, which is similar to the result observed at RT. The CoF value in the test at 800 °C fluctuates stronger at the beginning of the test, as compared with the CoF value at RT and 600 °C. The CoF value

at 800 °C tends to lower to 0.45. The difference in the CoF values for different temperatures is due to the contact between the alumina ball and the fcc-(Al,Cr)₂O₃ layer at RT and 600 °C, however at 800 °C, the contact is between the alumina ball and the α-(Al,Cr)₂O₃ layer.

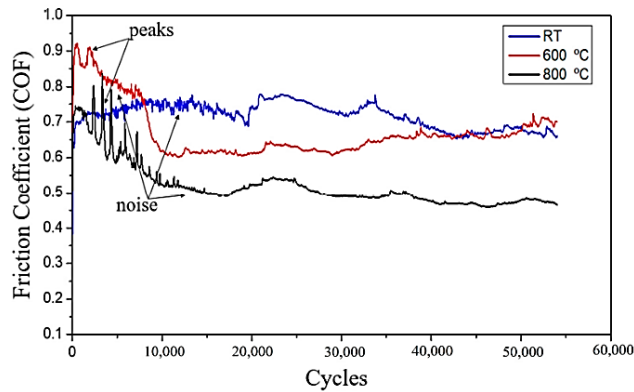


Figure 3.14. CoF behavior with respect to temperature.

The wear scars profiles on HMC taken with the mechanical profilometer, and the coatings and balls surfaces taken by SEM after the sliding tests are shown in Fig. 3.15. The highest wear scar width was observed after the sliding test at 600 °C on the coating surface and as well as on the ball (Fig. 3.15d-f). The relatively smooth surface morphology within the wear scars can be observed after the tests at RT and 600 °C in Fig. 3.15a,d, as compared with the test at 800 °C (Fig. 3.15g). The roughness within the wear scar surface after the sliding tests at 800 °C is higher due to a significant change in the wear mechanisms at this temperature. The wear scar profile shows that the depth in all sliding tests is approximately 0.7 μm, which indicates that the contact between the oxide layer and the ball at the end of the sliding tests took place. Two regions denoted as I and II can be seen in SEM images. Region I indicates the area in the center of the wear scars (i.e., the area corresponding to the real wear) and region II indicates the area where only ball ploughing occurred. Indeed, the wear scar surface morphology after the test at 800 °C within regions I and II suggests that probably, only ploughing of the ball occurred within region II (Fig. 3.16). Therefore, the shape of the wear scars profile shown in Fig. 3.15a,d,g suggests that the coating is plastically deformed during the sliding tests.

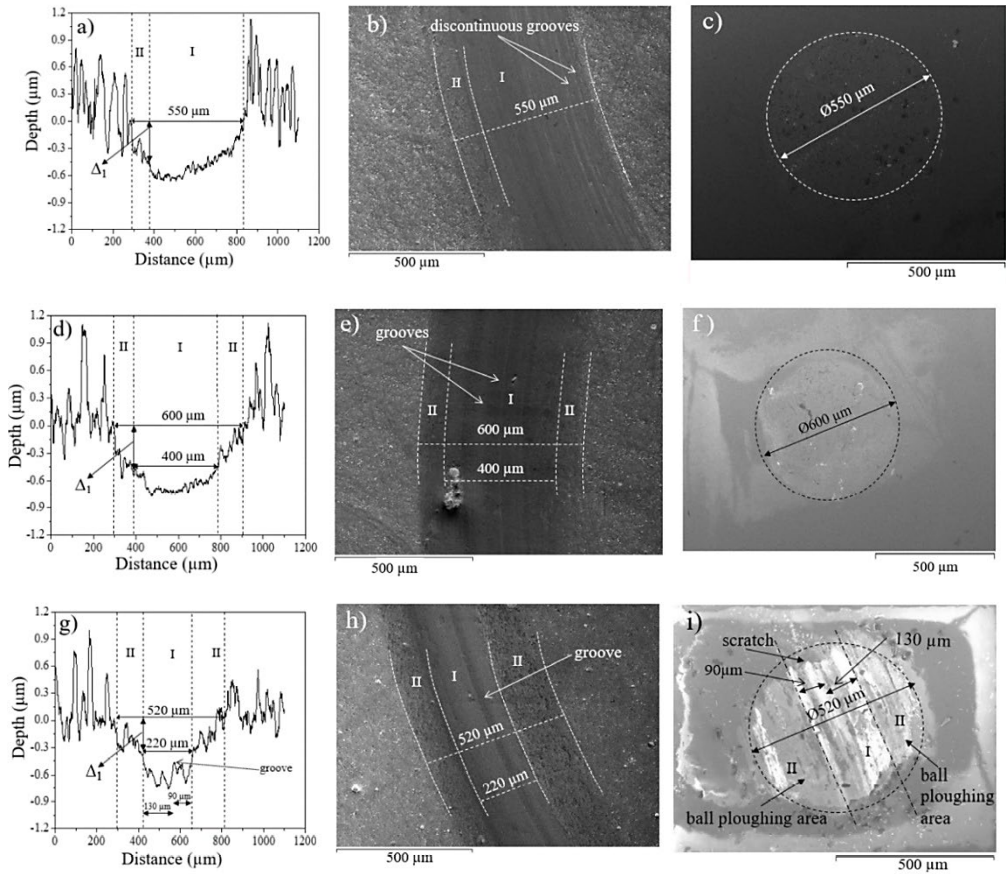


Figure 3.15. Wear scars profile and balls surface after the sliding tests at: (a-c) RT, (d-f) 600 °C and (g-h) 800 °C.

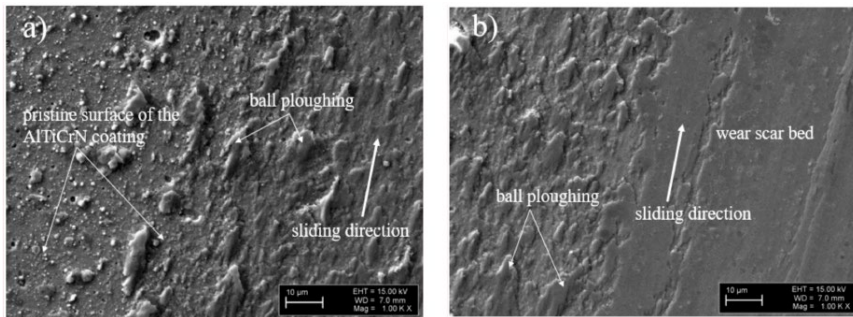


Figure 3.16. SEM images of the wear scar after sliding at 800 °C: (a) pristine surface and region II and (b) regions I and II.

The wear scars volume was calculated based on the difference between apparent and real wear volumes (Fig. 3.17). The apparent wear volume is the sum of the real wear volume and the volume corresponding to the deformation in the coating (Fig. 3.17a). The apparent wear volume was similar after the sliding tests at RT and 600 °C. The real wear volume was not measured after the RT sliding test because of no clear visibility of region II, see SEM image in Fig. 3.15b. The smallest apparent and real wear volumes were observed after the sliding test at 800 °C.

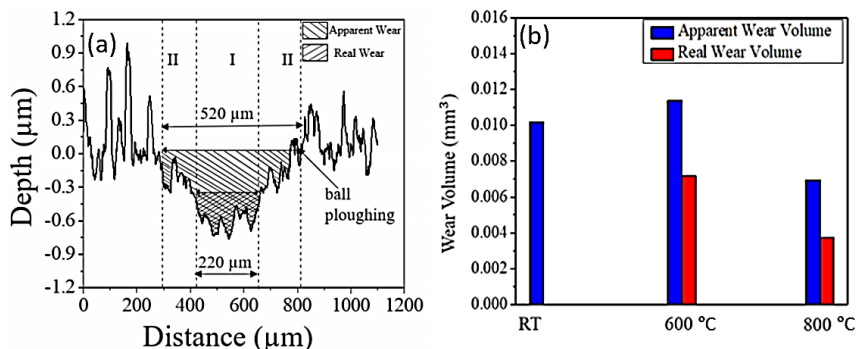


Figure 3.17. (a) Apparent and real wear and (b) wear volumes after the sliding tests at RT, 600 and 800 $^{\circ}\text{C}$.

Energy-dispersive X-ray spectroscopy

The EDS data of chemical composition of HMC is shown in Fig. 3.18. The EDS was taken on the pristine surface of the coating and within the wear scar after sliding. The EDS data corresponding to the measurement on the pristine surface shows that the content of oxygen increases and the content of nitrogen decreases with the temperature increasing (Fig. 3.18a).

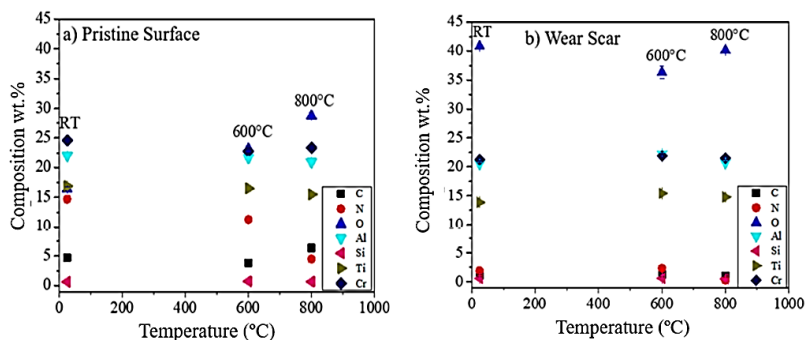


Figure 3.18. EDS analysis on (a) pristine and (b) wear scars surfaces of the coating.

Formation of a thin oxide layer on top of the AlTiCrN layer (Fig. 3.12b) can lead to the mentioned observation, and the fluctuation of the CoF value in the sliding test at 800 $^{\circ}\text{C}$ could be due to the influence of this oxide layer (Fig. 3.14). The EDS data collected on the wear scars shows the presence of higher concentration of oxygen contents independent of the test temperature, as compared with the pristine surface, with a negligible concentration of nitrogen (Fig. 3.18b). This observation suggests removing of the AlTiCrN layer in the course of sliding, i.e., the contact between the ball and the (Al,Cr) $_2\text{O}_3$ layer takes place in all sliding tests (Fig. 3.12b).

Nanoscratch tests on HMC

The nanoscratch tests were performed on the pristine surface of the coating after the sliding tests at different temperatures. Figure. 3.19 shows the results of the nanoscratch tests along with optical image of the scratch track on the coating surface. The procedure for the scratch tests was described in section 2.3. The elastic and plastic deformation occurred on the coating surface during scratching. The deviation due to plastic deformation and the wear (Δ_2) is the distance between the lines scan corresponding to the 1st and 2nd topography scans. The wear is relatively small, thus Δ_2 corresponds mostly to the plastic deformation of the

coating. The highest deflection was observed on the sample after the tests at 600 °C. The values of Δ_1 , Δ_2 , Δ_3 are shown in Table 3.3. The Δ_1 represents region II in Fig. 3.15b,e,h, which corresponds to the deflection of the coating under severe loading conditions in sliding tests. The values of Δ_1 and Δ_2 are similar, indicating similar plastic deformation in the sliding and nanoscratch tests. A significant coating surface deflection (elastic + plastic) was observed during the nanoscratch, for instance, the surface deflection (1140 nm) was about 1/3 of the coating thickness (3.6 μm) at the applied load of 400 mN in the test on the sample after the sliding test at 600 °C (Table 3.3).

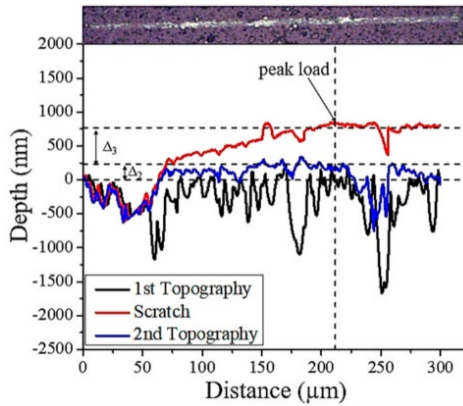


Figure 3.19. Nanoscratch behavior with an optical microscopy image of the scratch track after the test at 400 mN of load on the pristine surface after sliding at 800 °C.

Table 3.3. The Δ values after the sliding and nanoscratch tests.

Samples	Δ_1 (nm)	Δ_2 (nm)	Δ_3 (nm)
RT	480	480	1010
600 °C	450	490	1140
800 °C	350	250	820

Conclusions

The mechanical and tribological properties of the TiN-AlTiN/nACo-CrN/AlCrN-AlCrO-AlTiCrN coating were evaluated at RT and HT (600 and 800 °C). The increase of wear resistance for the coating tested at 800 °C was found due to the phase transformation within the (Al,Cr)₂O₃ layer (from fcc-(Al,Cr)₂O₃ to α -(Al,Cr)₂O₃) leading to the increase of hardness of this oxide layer. It leads also to the decrease of deflection and apparent wear volume of the whole coating system. In contrast, higher coating deflection was observed on the samples tested at RT and 600 °C.

3.4 Tribological performance of a-C:H:Si and Al₂O₃/a-C:H:Si coatings

Surface morphology

The SEM images of a-C:H:Si and Al₂O₃/a-C:H:Si coatings are shown in Fig. 3.20. The presence of irregular cavities can be observed on the a-C:H:Si coating surface (Fig. 3.20a). The alumina layer grew conformally, i.e., it resembled the morphology of the a-C:H:Si surface. After the deposition of a thin Al₂O₃ layer on top of the a-C:H:Si coating, the surface peculiarities can be seen (Fig. 3.20b).

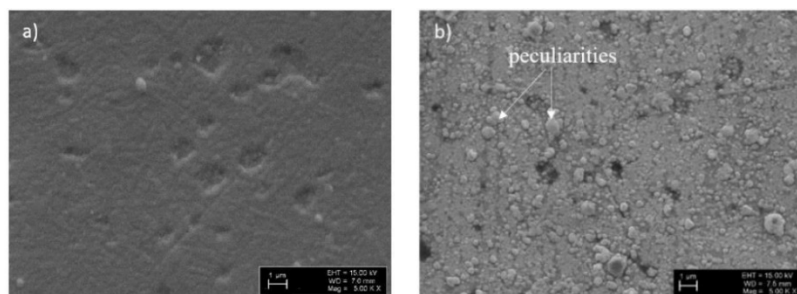


Figure 3.20. SEM images of the native surface of (a) a-C:H:Si and (b) Al₂O₃/a-C:H:Si.

Tribological behavior of a-C:H:Si and Al₂O₃/a-C:H:Si

Figure 3.21 shows the CoF versus cycle curves obtained at RT and 400 °C. The CoF values for both types of coatings (a-C:H:Si and Al₂O₃/a-C:H:Si) are very similar for the tests at RT, i.e., approximately 0.06-0.1. In other words, the thin alumina layer did not strongly influence the friction behavior of a-C:H:Si coating at RT. After reaching the smallest value at the beginning of the test, the CoF value slowly increased during subsequent periods of sliding. In contrast to the tests at RT, significant changes occurred in the tests at 400 °C. In the case of the a-C:H:Si coating, coating failure occurred at the beginning of the test after a short running-in period (Fig. 3.21a). However, in the case of the Al₂O₃/a-C:H:Si coating, relatively stable periods of sliding were revealed, with a CoF value of less than 0.03, and some periods had a super-low CoF of less than 0.01 (Fig. 3.21b). The extended time tests were repeated three times. A short running-in period was found in the case of the test at RT, which was practically absent in the tests at 400 °C. This result shows that the contact between the a-C:H:Si surface and the Si₃N₄ ball was already established at the beginning of the sliding tests.

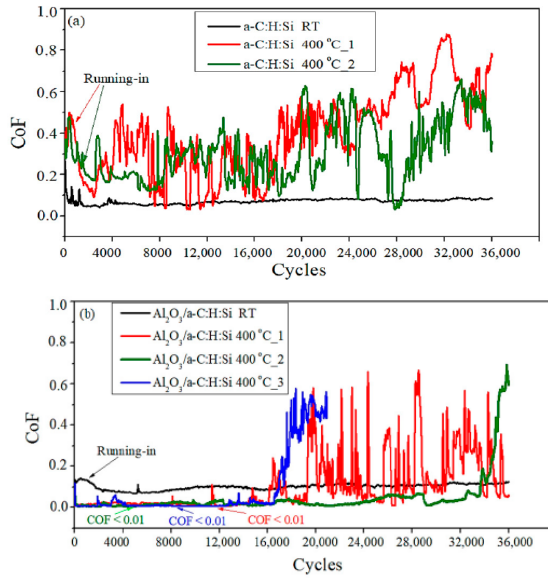


Figure 3.21. CoF versus cycles curves taken at RT and 400 °C on (a) a-C:H:Si and (b) Al₂O₃/a-C:H:Si coatings.

Figure 3.22 shows the SEM images of the wear scars observed on the a-C:H:Si and Al₂O₃/a-C:H:Si coatings after the sliding tests at RT and 400 °C. The smooth wear surfaces are formed on both coatings after sliding for 180-min at RT. The alumina islands can be seen on the Al₂O₃/a-C:H:Si coating as well (Fig. 3.22b). In the case of the a-C:H:Si coating, islands of the a-C:H:Si coating and the surface of WC-Co substrate can be seen after the test at 400 °C, in spite of the uniform a-C:H:Si coating surface for the Al₂O₃/a-C:H:Si coating (Fig. 3.22c,d). Therefore, the thin alumina layer protects the a-C:H:Si coating from oxidation failure.

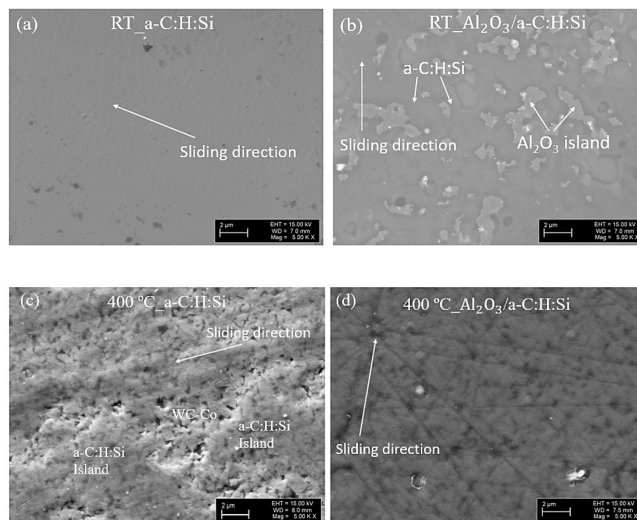


Figure 3.22. SEM images of wear scars after sliding tests at (a,b) RT for 180-min and (c,d) 400 °C for 5-min.

The wear scar profiles after the sliding tests of 5 and 180 min at RT are shown in (Fig. 3.23). The wear scars shape and width obtained after the sliding tests at RT differ between the a-C:H:Si and Al₂O₃/a-C:H:Si coatings. The wear scar widths on the a-C:H:Si and Al₂O₃/a-C:H:Si coatings were approximately 200 and 310 μm after the 5-min sliding tests (Fig. 3.23a,c). However, after 180-min of sliding, the wear scar on the a-C:H:Si coating was narrower and deeper, while wider and shallower for the Al₂O₃/a-C:H:Si coating (Fig. 3.23b,d). These results demonstrate the adaptation effect, an increase in the contact area leads to decreasing in the contact pressure. The depth of the wear scar of the a-C:H:Si was approximately 0.8 μm, which is close to the coating thickness. However, in the case of the Al₂O₃/a-C:H:Si coating, an approximately 0.4 μm thick a-C:H:Si layer was removed. Therefore, a longer lifetime can be expected for the Al₂O₃/a-C:H:Si coating in comparison to the a-C:H:Si coating.

The wear scar of the Al₂O₃/a-C:H:Si coating was also significantly wider after the 5-min sliding test at 400 °C, as compared to the RT 180-min test (Figs. 3.23d and 3.24b). These results could indicate that the structural changes within the a-C:H:Si coating, most likely owing to a-C:H:Si graphitization, decreased the hardness [88,89]. The wear scar profile of the a-C:H:Si coating after a 5-min sliding test at 400°C shows a catastrophic failure of the coating (Fig. 3.24a).

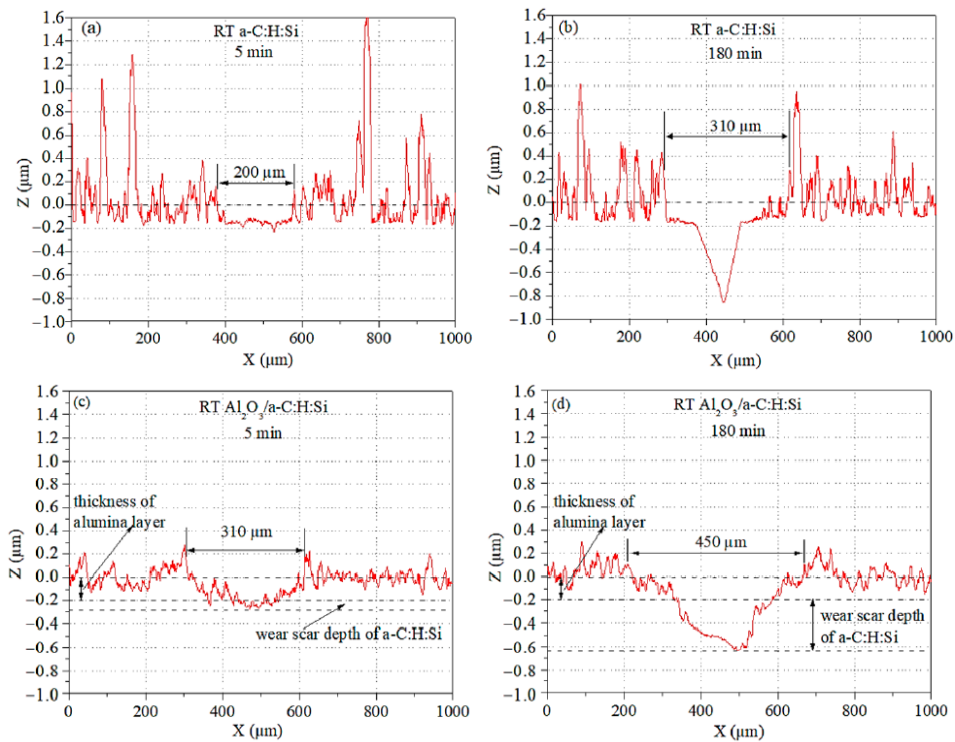


Figure 3.23. Wear scar profiles after sliding tests at RT and 400 °C: (a-b) a-C:H:Si and (c-d) Al₂O₃/a-C:H:Si.

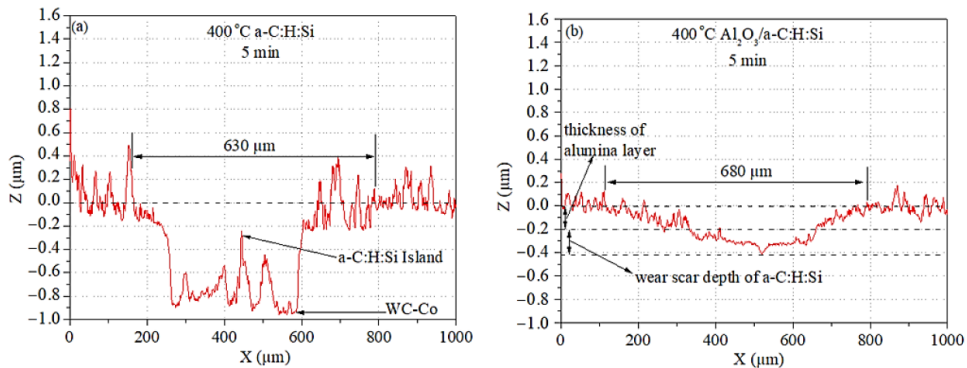


Figure 3.24. Wear scars line profiles taken on the (a) a-C:H:Si and (b) Al₂O₃/a-C:H:Si coatings after the 5-min sliding tests at 400 °C.

The apparent wear volumes of the a-C:H:Si and Al₂O₃/a-C:H:Si coatings are shown in Fig. 3.25. The calculation of the wear volume loss assumed an alumina layer thickness of 200 nm (Figs. 3.23 and 3.24). The wear volume measured on the a-C:H:Si layer (black color in Fig. 3.25) was larger for the a-C:H:Si coating than for the Al₂O₃/a-C:H:Si coating after the 180-min tests at RT. The wear volume was largest after the 5-min sliding test at 400 °C on the a-C:H:Si coating owing to the coating failure (Fig. 3.24a). It should be stressed that the reduced hardness of a-C:H:Si at HT leads to an increase of the wear scar width for Al₂O₃/a-C:H:Si (Fig. 3.24b). Therefore, an apparent wear volume loss may increase owing to the plastic deformation of the a-C:H:Si layer.

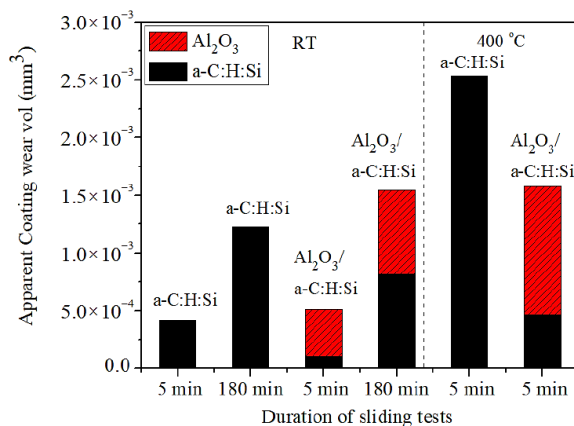


Figure 3.25. The apparent wear volumes loss of a-C:H:Si and Al₂O₃/a-C:H:Si coatings.

Raman spectroscopy

The Raman spectra were obtained on the native surface and within the wear scars (Fig. 3.26). Two characteristic peaks indicated sp² structure ordering, i.e., the D mode (1365 cm⁻¹) is active in the presence of disorder and the G mode (1545 cm⁻¹) indicates the presence of well-ordered graphite [90]. Raman peaks show the presence of vibrational modes in trans-polyacetylene (t-Pa) (1054 cm⁻¹) and sp-bonded chains (1900–2200 cm⁻¹) (Fig. 3.26a). The shape and position of the Raman spectra of the native and wear scar surfaces after the

5- and 180-min tests at RT were quite similar. In the case of the $\text{Al}_2\text{O}_3/\text{a-C:H:Si}$ coating (Fig. 3.26c), the peak positions were similar to those observed for the a-C:H:Si coating, except that the G peak shifted to (1532 cm^{-1}) after the 180-min sliding test.

The Raman spectrum of the native a-C:H:Si surface differs from the one obtained after HT heating. The G peak shifted to 1558 cm^{-1} , and formation of a shoulder (arrow in Fig. 3.26b) was observed after heating at $400\text{ }^\circ\text{C}$. The G peak shifted to a higher value (1612 cm^{-1}) after the 5-min sliding test at $400\text{ }^\circ\text{C}$ (Fig. 3.26b), which indicates the impact of mechanochemical processes on the a-C:H:Si structure. However, in the case of the $\text{Al}_2\text{O}_3/\text{a-C:H:Si}$ coating, no further G peak shift was observed after the 5-min test at $400\text{ }^\circ\text{C}$ (Fig. 3.26d).

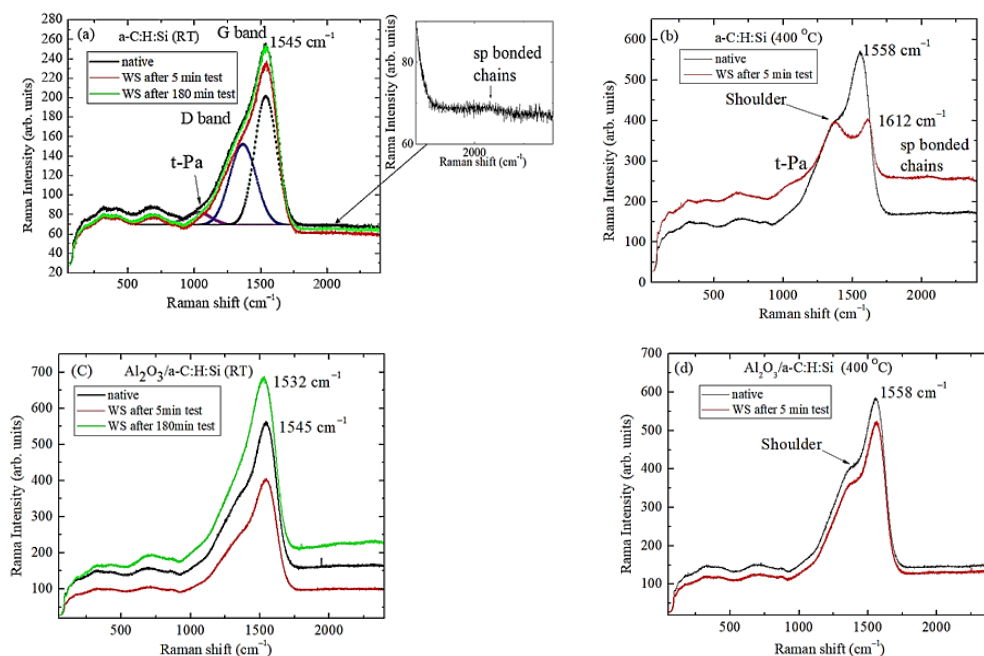


Figure 3.26. Raman spectra taken on the native surface and within the wear scars after the 5- and 180-min tests at RT and $400\text{ }^\circ\text{C}$ on the (a,b) a-C:H:Si and (c,d) $\text{Al}_2\text{O}_3/\text{a-C:H:Si}$ coatings.

X-ray photoelectron spectroscopy

The C 1s XPS spectra were recorded on the a-C:H:Si native surface (Figure 3.27). The peaks correspond to C–C sp^2 , C–C sp^3 , C–O, C=O, C–N, O–C=O and COO–R bonds [91-93]. Sp^3 surface enrichment and increased intensity of the XPS spectrum shoulder corresponding to the bonds formed between carbon, nitrogen, and oxygen atoms were observed after heating at $400\text{ }^\circ\text{C}$ (Fig. 3.27b). Figure 3.28 shows the XPS spectra taken on the surface of the wear scars after the sliding tests at RT and $400\text{ }^\circ\text{C}$. The bonds of the intensity ratio between the XPS signal intensity related to the a-C:H:Si coating (convolution of the C–C sp^2 and sp^3 peaks) and the intensity of the peak corresponding to C–O, C=O, etc., are higher for a-C:H:Si than for the $\text{Al}_2\text{O}_3/\text{a-C:H:Si}$ coating for the tests at RT and $400\text{ }^\circ\text{C}$. The C–C sp^2 and sp^3 XPS signals can be more strongly shielded on the $\text{Al}_2\text{O}_3/\text{a-C:H:Si}$ coating by a thicker and more uniformly distributed layer formed by agents such as C–O, C=O, etc.

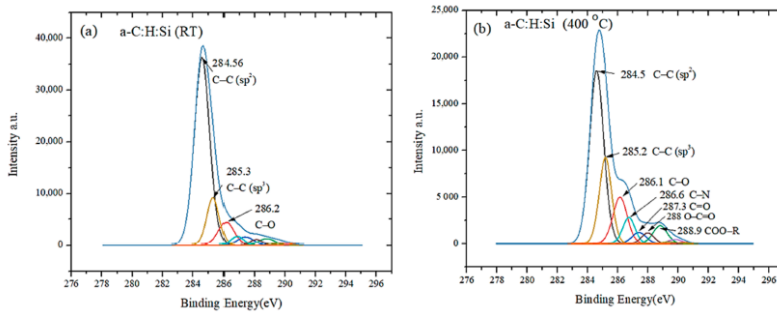


Figure 3.27. *C* 1s XPS spectra taken on the a-C:H:Si coating native surface at (a) RT and (b) 400 °C.

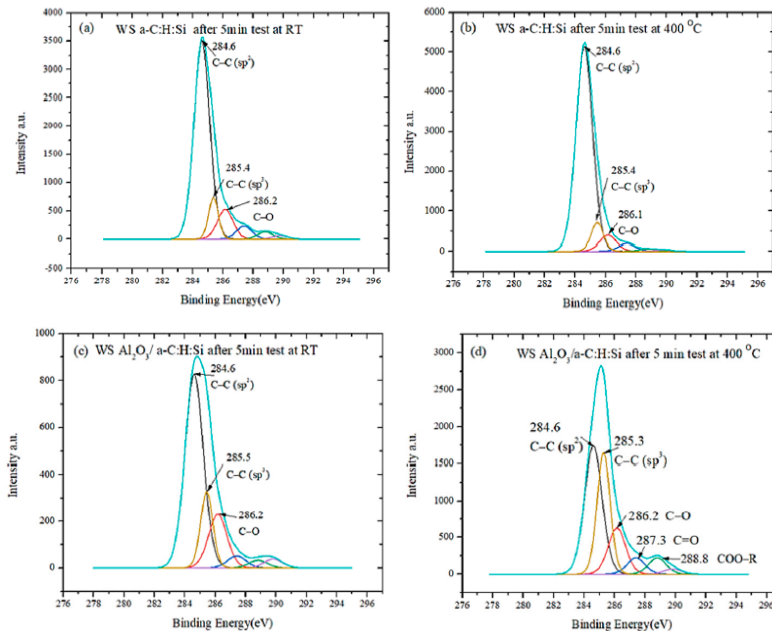


Figure 3.28. *C* 1s XPS spectra taken within the wear scars after the 5-min tests at RT and 400 °C on the (a,b) a-C:H:Si and (c,d) Al₂O₃/a-C:H:Si coatings.

Figure 3.29 shows the Si 2p XPS spectra, the broad Si 2p XPS spectra indicate the presence of several types of silicon oxide with different chemical states of Si (Si¹⁺(Si₂O), Si²⁺(SiO), Si³⁺(Si₂O₃), and Si⁴⁺(SiO₂)) [91]. Due to the likely a-C:H:Si oxidation and formation of the silicon oxides, the Si-C peak intensity decreased after heating at 400 °C (Fig. 3.29a). The Si 2p XPS spectra taken within the wear scars after the sliding test at 400 °C showed the strongest peaks located at 102.5-103.2 eV, which could indicate the formation of stoichiometric SiO₂ oxide.

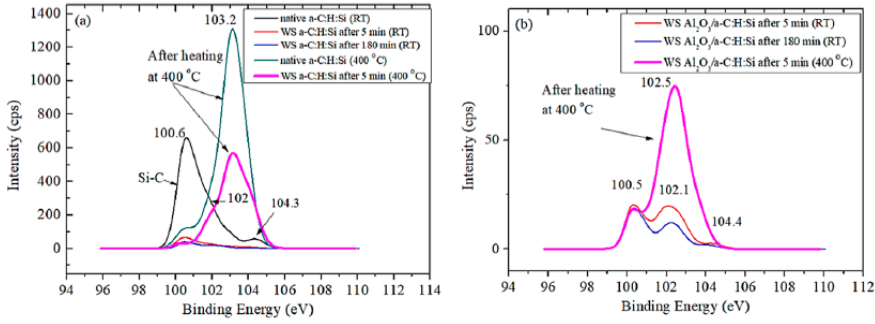


Figure 3.29. Si 2p XPS spectra taken within the native and wear scars surfaces after the sliding tests at RT and 400 °C on the (a) a-C:H:Si and (b) Al₂O₃/a-C:H:Si coatings.

The results of the Raman and XPS investigations of the sp² and sp³ bond contents in the coatings are shown in Fig. 3.30. In the case of the a-C:H:Si coating, the intensity ratios of the D and G peaks (I_D/I_G ratio) are similar for the Raman spectra taken on the native surface and within the wear scars after the 5- and 180-min sliding tests at RT (Fig. 3.30a). The sp²/sp³ ratios of the corresponding XPS peak intensities were similar for the a-C:H:Si coating as well (Fig. 3.30b). These findings imply that mechanochemical processes occurring during sliding tests at RT have no effect on the sp² and sp³ bonding networks in the bulk and on the surface, indicating high stability of the a-C:H:Si coating at RT. However, examination of the a-C:H:Si native surface after 400 °C heating reveals that the sp² and sp³ contents in the bulk and on the surface are modified in different ways.

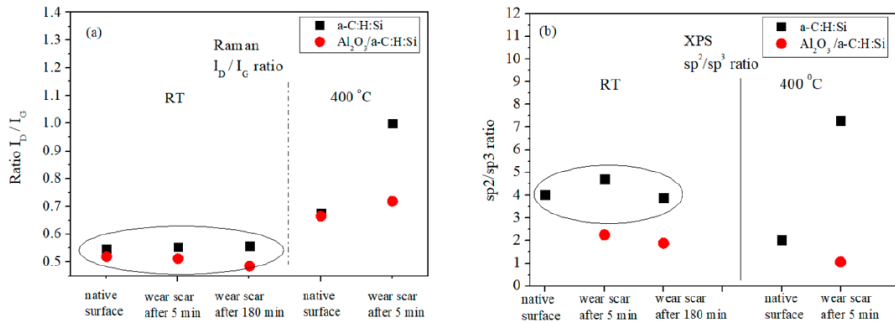


Figure 3.30. Summary of the results of (a) Raman and (b) XPS investigations.

In contrast to the investigations at RT, the analysis of the I_D/I_G ratio (for native surface) suggests that there is an increase in the sp² content in the bulk; however, the XPS data shows a decrease in the sp² and sp³ surface enrichment due to preferable etching of sp² on the a-C:H:Si coating surface at HT. After the 5-min sliding test at 400 °C, the sp² content increases in bulk and on the surface due to sp³ to sp² transformation induced by HT and mechanochemical processes during sliding, resulting in a catastrophic failure of a-C:H:Si. However, in the case of the Al₂O₃/a-C:H:Si coating, extra oxygen delivered by the alumina layer leads to sp³ enrichment of the surface formed within the wear scars in the sliding tests at RT and HT in comparison with a-C:H:Si, see Raman and XPS data in Fig. 3.30. The sp³ enrichment improves the thermal stability and increased the hardness and internal stress of the material [94].

In the sliding tests at RT and 400 °C, the Al₂O₃/a-C:H:Si coating shows better tribological properties and thermal stability than the a-C:H:Si coating.

First, an increase in the contact area and sp³ surface enrichment within the wear scar was observed in the tests at RT and 400 °C. The alumina layer was considered the adaptive layer. The adaptation effect was manifested owing to the use of a relatively soft and thin alumina layer, resulting in the increased contact area. The delivery of extra oxygen to the contact area led to an increase of sp³ content within the thin tribolayer, which improved the thermal and mechanical properties of the tribo-layer [95,96].

Second, carbon surface hydroxylation (C–OH termination) and formation of additional Si–OH bonds results in better tribological properties [96-98]. These types of surface passivation improve surface hydrophilicity and the absorption of atmospheric water vapor. Under ambient humid conditions (30%-60% humidity), water and oxygen absorbed by the surface form a well-ordered easily shared layer-like film, resulting in low friction [97]. In addition, higher surface energies for the a-C:H:Si coating surfaces after oxygen plasma treatment have been reported in [98,99], which means higher surface wettability, leading to more uniform water distribution along the surface. This, in turn, is likely to be beneficial for the formation of the well-ordered layer-like film on the a-C:H:Si surface [97]. In conclusion, it is expected that the hydrophilicity and wettability of Al₂O₃/a-C:H:Si within the wear scar area can be improved owing to the extra oxygen delivered by the alumina layer.

Third, silicon oxide affects the tribological behaviour of the a-C:H:Si coating, leading to the decrease of CoF [91]. The XPS study revealed several types of silicon oxide formed within the wear scar.

Fourth, the mechanism of hydrogen effusion may differ between the a-C:H:Si and Al₂O₃/a-C:H:Si coatings because of the alumina layer and a specific tribolayer layer formed on Al₂O₃/a-C:H:Si during the sliding tests. Upon thermal treatment, the hydrogen content decreases owing to the release of hydrogen and hydrocarbons (C_nH_x) [100]. The hydrogen and hydrocarbon diffusion through alumina can be limited, therefore the alumina layer can be considered a hydrogen diffusion barrier layer. Hydrogen and oxygen play important roles in understanding the friction mechanisms in carbon-based coatings [30,101].

Conclusions

A comparative study of the tribological properties of the a-C:H:Si and Al₂O₃/a-C:H:Si coatings at RT and 400 °C was performed. After 180-min sliding tests at RT, a wider and shallower wear scar was found on the Al₂O₃/a-C:H:Si coating in contrast to the a-C:H:Si coating. The smaller depth indicates that the a-C:H:Si coating lifetime can be increased by preparing an Al₂O₃/a-C:H:Si structure. The a-C:H:Si coating was unstable in the sliding tests at 400 °C and failed catastrophically. However, a stable super low friction regime of sliding over 80-160 min was observed for the Al₂O₃/a-C:H:Si coating. The thin Al₂O₃ acts as a multifunctional layer, which suppressed the atmospheric oxygen attack, induced adaptation and superlubricating effects, and suppressed the hydrogen effusion.

4 Conclusions

The study focuses on the understanding mechanisms of wear and friction, deflection, adaptive and superlubricating effects and phase transition in coatings at high temperature. Particular attention was paid to the investigation of the influence of oxide layers deposited on top of coatings and on the tribological properties of coating/substrate system. This approach was developed to suppress the air oxygen oxidation of coatings.

The following conclusions can be drawn from this research.

1. The high temperature tribological properties of the a-C:H:Si coating were improved by the deposition of the Al₂O₃ layer. The Al₂O₃/a-C:H:Si coating shows low CoF and good thermal stability in the sliding tests at 400 °C. In contrast, the catastrophic failure of the a-C:H:Si coating was observed at the same tribological conditions. It was shown that the alumina layer behaves as the adaptive layer during the initial run-in period, specifically, the contact area between the tribo-pairs increases, which results in a decrease of the contact pressure. Therefore, the lifetime of the a-C:H:Si coating can be improved by the deposition of an alumina layer. The superlubricating effect with the CoF value < 0.01 was observed on the Al₂O₃/a-C:H:Si coating in the sliding tests at 400 °C. Higher hydrophilicity and wettability of the surface within the contact due to extra oxygen delivered by an alumina layer lead to the formation of the well-ordered layer-like water, resulting in super low friction. The plastic deformation (deflection) of the Al₂O₃/a-C:H:Si coating observed in the sliding tests at 400 °C can be explained by reducing of the a-C:H:Si hardness due to sp³ to sp² transition.
2. The tribological tests were carried out on the multilayer TiN-AlTiN/nACo-CrN/AlCrN-AlCrO-AlTiCrN coating at room and elevated temperatures (600 and 800 °C). The nitride based multilayer coating was protected by an AlCrO layer against air oxygen oxidation attack. The lower CoF, apparent wear volume and coating deflection were found after the sliding tests at 800 °C. The transition from the fcc-AlCrO to α-AlCrO phase occurred at 800 °C, leading to an increase of the hardness of oxide layer, resulting in the improvement of the mentioned properties. The significant deflection occurred in the nanoscratch tests as well, namely the surface deflection was about 1/3 of the coating thickness at the applied load of 400 mN.
3. The relation between the self-organized criticality (SOC) and self-organization (SO) during the reciprocating sliding on the NCD/SCD(110) films were established based on the distribution of friction force drops. The power-law based distribution of the friction force occurred at the initial run-in period, i.e., the first 600 seconds of sliding indicate the presence of SOC. It was also found that the value of the power-law exponent μ depends on the roughness of the films. The transition from SOC to SO was observed.
4. The properties (nanohardness and Young's modulus) of a 100 nm thick Al₂O₃ layer deposited on the Si(100) substrate are affected by the substrate behavior in the tests. The CoF values evaluated in the nanoscratch tests at the load between 5-20 mN show disagreement with Amontons' friction law, i.e., CoF depends on the load. This is probably due to a continuous change from elastic to plastic deformation in the Si(100) substrate. On the contrary, at 200-400 mN of the load, the CoF value was independent of the load.

Recommendations and future plans

The present study proves that a substantial improvement of tribological properties of carbon based coatings at high temperature can be achieved by the preparation of a relatively thin oxide layer on top of the mentioned coatings.

However, it could be reasonable to explore the influence of different types of oxide and their properties (thickness, roughness, etc.) on the thermal stability of the carbon based coatings.

References

1. Holmberg, K. and Erdemir, A., 2017. Influence of tribology on global energy consumption, costs and emissions. *Friction*, 5(3), pp. 263-284.
2. Podgursky, V., Bogatov, A., Yashin, M., Sobolev, S. and Gershman, I.S., 2018. Relation between self-organization and wear mechanisms of diamond films. *Entropy*, 20(4), p. 279.
3. Podgursky, V., Hantschel, T., Bogatov, A., Kimmari, E., Antonov, M., Viljus, M., Mikli, V., Tsigkourakos, M., Vandervorst, W., Buijnsters, J.G. and Raadik, A.T., 2014. Rippling on wear scar surfaces of nanocrystalline diamond films after reciprocating sliding against ceramic balls. *Tribology Letters*, 55(3), pp. 493-501.
4. Podgursky, V., Bogatov, A., Yashin, M., Viljus, M., Bolshakov, A.P., Sedov, V., Volobujeva, O., Mere, A., Raadik, T. and Ralchenko, V., 2019. A comparative study of the growth dynamics and tribological properties of nanocrystalline diamond films deposited on the (110) single crystal diamond and Si (100) substrates. *Diamond and Related Materials*, 92, pp. 159-167.
5. Yashin, M., Baroninš, J., Menezes, P.L., Viljus, M., Raadik, T., Bogatov, A., Antonov, M. and Podgursky, V., 2017. Wear rate of nanocrystalline diamond coating under high temperature sliding conditions. In *Solid State Phenomena* (Vol. 267, pp. 219-223). Trans Tech Publications Ltd.
6. Holleck, H. and Schier, A.V., 1995. Multilayer PVD coatings for wear protection. *Surface and Coatings Technology*, 76, pp. 328-336.
7. Gillespie, R.J. and Robinson, E.A., 2007. Gilbert N. Lewis and the chemical bond: The electron pair and the octet rule from 1916 to the present day. *Journal of computational chemistry*, 28(1), pp. 87-97.
8. Moore, S.L., Samudrala, G.K., Catledge, S.A. and Vohra, Y.K., 2018. Rapid growth of nanocrystalline diamond on single crystal diamond for studies on materials under extreme conditions. *Scientific reports*, 8(1), pp. 1-8.
9. Tsigkis, V., Bashandeh, K., Lan, P. and Polycarpou, A.A., 2021. Tribological behavior of PS400-related tribopairs for space exploration. *Tribology International*, 153, p. 106636.
10. Erdemir, A. and Donnet, C., 2006. Tribology of diamond-like carbon films: recent progress and future prospects. *Journal of Physics D: Applied Physics*, 39(18), p. R311.
11. Li, H., Xu, T., Wang, C., Chen, J., Zhou, H. and Liu, H., 2006. Annealing effect on the structure, mechanical and tribological properties of hydrogenated diamond-like carbon films. *Thin Solid Films*, 515(4), pp. 2153-2160.
12. Simpson, R.L., 1995. The thermal stability of diamond-like carbon. *Diamond and related materials*, 4(3), pp. 191-199.
13. Pastewka, L., Moser, S., Gumbsch, P. and Moseler, M., 2011. Anisotropic mechanical amorphization drives wear in diamond. *Nature materials*, 10(1), pp. 34-38.
14. Kiran, M.R., Ulla, H., Satyanarayan, M.N. and Umesh, G., 2017. Optoelectronic properties of hybrid diodes based on vanadyl-phthalocyanine and zinc oxide. *Superlattices and Microstructures*, 112, pp. 654-664.
15. Batzill, M., Katsiev, K. and Diebold, U., 2004. Tuning the oxide/organic interface: Benzene on SnO₂ (101). *Applied physics letters*, 85(23), pp. 5766-5768.
16. Hoornaert, T., Hua, Z.K. and Zhang, J.H., 2009. Hard wear-resistant coatings: A review. *Advanced tribology*, pp. 774-779.
17. https://www.platit.com/media/filer/2020/compendium_en61.pdf (accessed on 3-03-2021).

18. Trunov, M.A., Schoenitz, M. and Dreizin, E.L., 2006. Effect of polymorphic phase transformations in alumina layer on ignition of aluminium particles. *Combustion Theory and Modelling*, 10(4), pp. 603-623
19. Jeurgens, L.P.H., Sloof, W.G., Tichelaar, F.D. and Mittemeijer, E.J., 2002. Growth kinetics and mechanisms of aluminum-oxide films formed by thermal oxidation of aluminum. *Journal of applied physics*, 92(3), pp. 1649-1656.
20. Levin, I. and Brandon, D., 1998. Metastable alumina polymorphs: crystal structures and transition sequences. *Journal of the american ceramic society*, 81(8), pp. 1995-2012.
21. Ruano, O.A., Wadsworth, J. and Sherby, O.D., 2003. Deformation of fine-grained alumina by grain boundary sliding accommodated by slip. *Acta Materialia*, 51(12), pp. 3617-3634.
22. Najafi, H., Karimi, A., Dessarzin, P. and Morstein, M., 2013. Formation of cubic structured $(Al_{1-x}Cr_x)_{2+ \delta}O_3$ and its dynamic transition to corundum phase during cathodic arc evaporation. *Surface and Coatings Technology*, 214, pp. 46-52.
23. Trunov, M.A., Schoenitz, M., Zhu, X. and Dreizin, E.L., 2005. Effect of polymorphic phase transformations in Al_2O_3 film on oxidation kinetics of aluminum powders. *Combustion and flame*, 140(4), pp. 310-318.
24. Khatibi, A., Palisaitis, J., Höglund, C., Eriksson, A., Persson, P.Å., Jensen, J., Birch, J., Eklund, P. and Hultman, L., 2011. Face-centered cubic $(Al_{1-x}Cr_x)_2O_3$. *Thin Solid Films*, 519(8), pp. 2426-2429.
25. Alling, B., Khatibi, A., Simak, S.I., Eklund, P. and Hultman, L., 2013. Theoretical investigation of cubic B1-like and corundum $(Cr_{1-x}Al_x)_2O_3$ solid solutions. *Journal of Vacuum Science & Technology A: Vacuum, Surfaces, and Films*, 31(3), p. 030602.
26. Diechle, D., Stueber, M., Leiste, H., Ulrich, S. and Schier, V., 2010. Combinatorial approach to the growth of α - $(Al_{1-x}, Cr_x)_2O_3$ solid solution strengthened thin films by reactive rf magnetron sputtering. *Surface and Coatings Technology*, 204(20), pp. 3258-3264.
27. Mazurkiewicz, A. and Smolik, J., 2015. The innovative directions in development and implementations of hybrid technologies in surface engineering. *Archives of metallurgy and materials*, 60.
28. Cselle, T., Coddet, O., Galamand, C., Holubar, P., Jilek, M., Jilek, J., Luemkemann, A. and Morstein, M., 2009. Triplecoatings³[®]-New generation of PVD-Coatings for cutting tools. *Journal of machine manufacturing*, 49(E1), pp. 19-25.
29. Lümkemann, A., Beutner, M., Morstein, M., Köchig, M., Cselle, M.W.T. and Karpuschewski, B., 2014, October. A New Generation of PVD Coatings for High-Performance Gear Hobbing. *In Coatings Conference. Thessaloniki, Greece*.
30. Kano, M., Yasuda, Y., Okamoto, Y., Mabuchi, Y., Hamada, T., Ueno, T., Ye, J., Konishi, S., Takeshima, S., Martin, J.M. and Bouchet, M.D.B., 2005. Ultralow friction of DLC in presence of glycerol mono-oleate (GNO). *Tribology Letters*, 18(2), pp. 245-251.
31. Matthews, A., Leyland, A., Holmberg, K. and Ronkainen, H., 1998. Design aspects for advanced tribological surface coatings. *Surface and Coatings Technology*, 100, pp. 1-6.
32. Holmberg, K. and Matthews, A., 2009. Coatings tribology: properties, mechanisms, techniques and applications in surface engineering. *Elsevier*.
33. Rapoport, L., Leshchinsky, V., Lapsker, I., Volovik, Y., Nepomnyashchy, O., Lvovsky, M., Popovitz-Biro, R., Feldman, Y. and Tenne, R., 2003. Tribological properties of WS₂ nanoparticles under mixed lubrication. *Wear*, 255(7-12), pp. 785-793.

34. Dong, J.X. and Hu, Z.S., 1998. A study of the anti-wear and friction-reducing properties of the lubricant additive, nanometer zinc borate. *Tribology international*, 31(5), pp. 219-223.
35. Zhou, J., Yang, J., Zhang, Z., Liu, W. and Xue, Q., 1999. Study on the structure and tribological properties of surface-modified Cu nanoparticles. *Materials Research Bulletin*, 34(9), pp. 1361-1367.
36. Fan, X., Wang, L. and Xia, Y., 2015. Oil-soluble lithium salts as novel lubricant additives towards improving conductivity and tribological performance of bentone grease. *Lubrication Science*, 27(6), pp. 359-368.
37. Fathi, M., Safavi, M.S., Mahdavi, S., Mirzazadeh, S., Charkhesht, V., Mardanifar, A. and Mehdipour, M., 2021. Co-P alloy matrix composite deposits reinforced by nano-MoS₂ solid lubricant: An alternative tribological coating to hard chromium coatings. *Tribology International*, 159, p. 106956.
38. Cui, L., Lu, Z. and Wang, L., 2014. Probing the low-friction mechanism of diamond-like carbon by varying of sliding velocity and vacuum pressure. *Carbon*, 66, pp. 259-266.
39. Lettington, A.H., 1998. Applications of diamond-like carbon thin films. *Carbon*, 36(5-6), pp. 555-560.
40. Zhu, S., Cheng, J., Qiao, Z. and Yang, J., 2019. High temperature solid-lubricating materials: A review. *Tribology international*, 133, pp. 206-223.
41. Voevodin, A.A. and Zabinski, J.S., 2000. Supertough wear-resistant coatings with 'chameleon'surface adaptation. *Thin Solid Films*, 370(1-2), pp. 223-231.
42. Muratore, C. and Voevodin, A.A., 2009. Chameleon coatings: adaptive surfaces to reduce friction and wear in extreme environments. *Annual Review of Materials Research*, 39, pp. 297-324.
43. Voevodin, A.A., Muratore, C. and Aouadi, S.M., 2014. Hard coatings with high temperature adaptive lubrication and contact thermal management. *Surface and Coatings Technology*, 257, pp. 247-265.
44. Glansdorff, P. and Prigogine, I., 1970. Non-equilibrium stability theory. *Physica*, 46 (3), pp. 344-366.
45. Glansdorff, P. and Prigogine, I., 1971. Thermodynamic theory of structure, stability and fluctuations. *J. Willey & Sons*.
46. Prigogine, I. and Stengers, I., 1997. The end of certainty. *Simon and Schuster*.
47. Kondepudi, D. and Prigogine, I., 1999. Modern thermodynamics. From heat to dissipative structures. *Chichester–New York–Weinheim–Brisbane–Toronto–Singapore*.
48. Fox-Rabinovich, G. and Totten, G.E. eds., 2006. Self-organization during friction: advanced surface-engineered materials and systems design. *CRC Press*.
49. Tabor, D., 1992. Friction as a dissipative process. In *Fundamentals of friction: macroscopic and microscopic processes* (pp. 3-24). *Springer, Dordrecht*.
50. Fox-Rabinovich, G. and Totten, G.E. eds., 2006. Self-organization during friction: advanced surface-engineered materials and systems design. *CRC Press*.
51. Fox-Rabinovich, G., Kovalev, A., Gershman, I., Wainstein, D., Aguirre, M.H., Covelli, D., Paiva, J., Yamamoto, K. and Veldhuis, S., 2018. Complex behavior of nano-scale tribo-ceramic films in adaptive PVD coatings under extreme tribological conditions. *Entropy*, 20(12), p. 989.
52. Kostecki, B.I., 1970. Friction, lubrication and wear in machines. BI Kostetskiy.-K.: *Tehnika*.
53. Jacobson, S. and Hogmark, S., 2010. Tribofilms: *on the crucial importance of tribologically induced surface modifications*.

54. Salamon, P. and Sieniutycz, S. eds., 1990. Nonequilibrium Theory and Extremum Principles. *Taylor & Francis*.
55. Bershadsky, L.I., 1992. On self-organizing and concept of tribosystem self-organizing. *J. Frict. Wear*, 13, pp. 101-114.
56. Kostetsky, B.I., 1993. An evolution of the materials' structure and phase composition and the mechanisms of the self-organizing phenomenon at external friction. *J. Frict. Wear*, 14, pp. 773-783.
57. Fox-Rabinovich, G.S., Endrino, J.L., Aguirre, M.H., Beake, B.D., Veldhuis, S.C., Kovalev, A.I., Gershman, I.S., Yamamoto, K., Losset, Y., Wainstein, D.L. and Rashkovskiy, A., 2012. Mechanism of adaptability for the nano-structured TiAlCrSiYN-based hard physical vapor deposition coatings under extreme frictional conditions. *Journal of Applied Physics*, 111(6), p. 064306.
58. Kovalev, A., Wainstein, D. and Rashkovskiy, A., 2010. Investigation of anomalous physical properties of multilayer nanolaminate (TiAl) N/Cu coatings by electron spectroscopy techniques. *Surface and Interface Analysis*, 42(6-7), pp. 1361-1363.
59. Bak, P., 1996. The Discovery of Self-Organized Criticality. In *How Nature Works* (pp. 33-48). *Copernicus*, New York, NY
60. Klamecki, B.E., 1980. Wear—An entropy production model. *Wear*, 58(2), pp. 325-330.
61. Klamecki, B.E., 1980. A thermodynamic model of friction. *Wear*, 63(1), pp. 113-120.
62. Kostetsky, B.I., 1992. The structural-energetic concept in the theory of friction and wear (synergism and self-organization). *Wear*, 159(1), pp. 1-15.
63. Fox-Rabinovich, G.S., Gershman, I.S., Yamamoto, K., Biksa, A., Veldhuis, S.C., Beake, B.D. and Kovalev, A.I., 2010. Self-organization during friction in complex surface engineered tribosystems. *Entropy*, 12(2), pp. 275-288.
64. Bryant, M.D., 2010. Unification of friction and wear. *Recent Developments in Wear Prevention, Friction and Lubrication*, 248(1), pp. 159-196.
65. Zypman, F.R., Ferrante, J., Jansen, M., Scanlon, K. and Abel, P., 2003. Evidence of self-organized criticality in dry sliding friction. *Journal of Physics: Condensed Matter*, 15(12), p. L191.
66. Nosonovsky, M., 2010. Self-organization at the frictional interface for green tribology. *Philosophical Transactions of the Royal Society A: Mathematical, Physical and Engineering Sciences*, 368(1929), pp. 4755-4774.
67. Chin, J.H. and Chen, C.C., 1993. A study of stick-slip motion and its influence on the cutting process. *International journal of mechanical sciences*, 35(5), pp. 353-370.
68. Oliver, W.C. and Pharr, G.M., 1992. An improved technique for determining hardness and elastic modulus using load and displacement sensing indentation experiments. *Journal of materials research*, 7(6), pp. 1564-1583.
69. Nayar, P., Khanna, A., Kabiraj, D., Abhilash, S.R., Beake, B.D., Losset, Y. and Chen, B., 2014. Structural, optical and mechanical properties of amorphous and crystalline alumina thin films. *Thin Solid Films*, 568, pp. 19-24.
70. Boyd, E.J. and Uttamchandani, D., 2011. Measurement of the anisotropy of young's modulus in single-crystal silicon. *Journal of Microelectromechanical Systems*, 21(1), pp. 243-249.
71. Tripp, M.K., Stampfer, C., Miller, D.C., Helbling, T., Herrmann, C.F., Hierold, C., Gall, K., George, S.M. and Bright, V.M., 2006. The mechanical properties of atomic layer deposited alumina for use in micro-and nano-electromechanical systems. *Sensors and Actuators A: Physical*, 130, pp. 419-429.

72. Beake, B.D., Liskiewicz, T.W. and Smith, J.F., 2011. Deformation of Si (100) in spherical contacts—Comparison of nano-fretting and nano-scratch tests with nano-indentation. *Surface and Coatings Technology*, 206(7), pp. 1921-1926.
73. Bhushan, B., Subramaniam, V.V., Malshe, A., Gupta, B.K. and Ruan, J., 1993. Tribological properties of polished diamond films. *Journal of applied physics*, 74(6), pp. 4174-4180.
74. Ritacco, H.A., 2020. Complexity and self-organized criticality in liquid foams. A short review. *Advances in Colloid and Interface Science*, p. 102282.
75. Nosonovsky, M. and Bhushan, B., 2007. Multiscale friction mechanisms and hierarchical surfaces in nano-and bio-tribology. *Materials Science and Engineering: R: Reports*, 58(3-5), pp. 162-193.
76. Kondepudi, D. and Prigogine, I., 2014. Modern thermodynamics: from heat engines to dissipative structures. *John Wiley & Sons*.
77. Nosonovsky, M., Amano, R., Lucci, J.M. and Rohatgi, P.K., 2009. Physical chemistry of self-organization and self-healing in metals. *Physical Chemistry Chemical Physics*, 11(41), pp. 9530-9536.
78. Amiri, M., Droguett, E.L., Iyyer, N. and Naderi, M., 2015. The second law of thermodynamics and degradation of materials. *Proceedings of the Safety and Reliability of Complex Engineered Systems, Zurich, Switzerland*, pp. 7-10.
79. Nosonovsky, M. and Esche, S.K., 2008. A paradox of decreasing entropy in multiscale Monte Carlo grain growth simulations. *Entropy*, 10(2), pp. 49-54.
80. Prigogine, I., 1978. Time, structure, and fluctuations. *Science*, 201(4358), pp. 777-785.
81. Fox-Rabinovich, G.S., 2006. Principles of friction control for the surface engineered materials (pp. 3-13). *CRC Press, Taylor and Francis Group: Boca Raton, NW, USA*.
82. Prigogine, I. and Stengers, I., 2018. Order out of chaos: *Man's new dialogue with nature*. Verso Books.
83. Buldyrev, S.V., Ferrante, J. and Zypman, F.R., 2006. Dry friction avalanches: Experiment and theory. *Physical Review E*, 74(6), p. 066110.
84. Lacombe, F., Zapperi, S. and Herrmann, H.J., 2001. Force fluctuation in a driven elastic chain. *Physical Review B*, 63(10), p. 104104.
85. Bak, P., Tang, C. and Wiesenfeld, K., 1987. Self-organized criticality: An explanation of the 1/f noise. *Physical review letters*, 59(4), p. 381.
86. Nosonovsky, M. and Bhushan, B., 2009. Thermodynamics of surface degradation, self-organization and self-healing for biomimetic surfaces. *Philosophical Transactions of the Royal Society A: Mathematical, Physical and Engineering Sciences*, 367(1893), pp. 1607-1627.
87. Konicek, A.R., Grierson, D.S., Sumant, A.V., Friedmann, T.A., Sullivan, J.P., Gilbert, P.U.P.A., Sawyer, W.G. and Carpick, R.W., 2012. Influence of surface passivation on the friction and wear behavior of ultrananocrystalline diamond and tetrahedral amorphous carbon thin films. *Physical Review B*, 85(15), p. 155448.
88. Li, H., Xu, T., Wang, C., Chen, J., Zhou, H. and Liu, H., 2006. Annealing effect on the structure, mechanical and tribological properties of hydrogenated diamond-like carbon films. *Thin Solid Films*, 515(4), pp. 2153-2160.
89. Zhang, T.F., Wan, Z.X., Ding, J.C., Zhang, S., Wang, Q.M. and Kim, K.H., 2018. Microstructure and high-temperature tribological properties of Si-doped hydrogenated diamond-like carbon films. *Applied Surface Science*, 435, pp. 963-973.
90. Ferrari, A.C. and Robertson, J., 2004. Raman spectroscopy of amorphous, nanostructured, diamond-like carbon, and nanodiamond. *Philosophical Transactions of the Royal Society of London. Series A: Mathematical, Physical and Engineering Sciences*, 362(1824), pp. 2477-2512.

91. Rouhani M, Hobley J, Hong FC, Jeng YR. Spectroscopic investigation of thermally induced structural evolution of aC: H: Si film. *Applied Surface Science*. 2021 Mar 1;541:148413.
92. Mangolini, F., Hilbert, J., McClimon, J.B., Lukes, J.R. and Carpick, R.W., 2018. Thermally induced structural evolution of silicon-and oxygen-containing hydrogenated amorphous carbon: a combined spectroscopic and molecular dynamics simulation investigation. *Langmuir*, 34(9), pp. 2989-2995.
93. Scharf, T.W., Ott, R.D., Yang, D. and Barnard, J.A., 1999. Structural and tribological characterization of protective amorphous diamond-like carbon and amorphous CN x overcoats for next generation hard disks. *Journal of Applied Physics*, 85(6), pp. 3142-3154.
94. Safaie, P., Eshaghi, A. and Bakhshi, S.R., 2016. Structure and mechanical properties of oxygen doped diamond-like carbon thin films. *Diamond and Related Materials*, 70, pp. 91-97.
95. Moolsradoo, N., Abe, S. and Watanabe, S., 2011. Thermal stability and tribological performance of DLC-Si-O films. *Advances in Materials Science and Engineering*, 2011.
96. Mangolini, F., Krick, B.A., Jacobs, T.D., Khanal, S.R., Streller, F., McClimon, J.B., Hilbert, J., Prasad, S.V., Scharf, T.W., Ohlhausen, J.A. and Lukes, J.R., 2018. Effect of silicon and oxygen dopants on the stability of hydrogenated amorphous carbon under harsh environmental conditions. *Carbon*, 130, pp. 127-136.
97. Chen, X., Kato, T., Kawaguchi, M., Nosaka, M. and Choi, J., 2013. Structural and environmental dependence of superlow friction in ion vapour-deposited aC: H: Si films for solid lubrication application. *Journal of Physics D: Applied Physics*, 46(25), p. 255304.
98. Kim, J.I., Jang, Y.J., Kim, J. and Jeong, J.H., 2021. Improvement of running-in process of tetrahedral amorphous carbon film sliding against Si₃N₄ under humid air by O₂ plasma post-irradiation. *Applied Surface Science*, 538, p. 147957.
99. López-Santos, C., Yubero, F., Cotrino, J. and González-Elipe, A.R., 2011. Lateral and in-depth distribution of functional groups on diamond-like carbon after oxygen plasma treatments. *Diamond and related materials*, 20(2), pp. 49-56.
100. Wild, C. and Koidl, P., 1987. Thermal gas effusion from hydrogenated amorphous carbon films. *Applied physics letters*, 51(19), pp. 1506-1508.
101. Erdemir, A., 2001. The role of hydrogen in tribological properties of diamond-like carbon films. *Surface and Coatings Technology*, 146, pp. 292-297.

Acknowledgements

First, I wish to express my special gratitude to my supervisor senior research scientist Vitali Podgursky and co-supervisor Prof. Fjodor Sergejev for their continuous support, guidance, and encouragement throughout my PhD studies.

I would like to thank co-authors of the papers related to the thesis and colleagues in the Department of Mechanical and Industrial Engineering for their support, especially Andrei Bogatov, Maxim Yashin and Abrar Hussain, for numerous scientific discussions. My special acknowledgement goes to PhD Mart Viljus for the help with SEM measurements and technician Heinar Vagiström for help with sample preparation. I also want to thank my teachers at Tallinn University of Technology, especially Professor Emeritus Priit Kulu for the help with the preparation of my PhD thesis.

I would like to express my deep gratitude towards my parents, siblings, mother in law, relatives, and my adorable kids (Nabihah Asad and Taimoor Alamgir) for their love, patience, and encouragement at every stage of my personal and academic life. Lastly, I want to dedicate my thesis to my loving wife Dr. Eumna Tehseen, her affectionate and endlessly supporting attitude made this possible. You have been my supporting pillar and I am truly obliged for your practical and emotional support.

This study was supported by the Estonian Ministry of Education and Research under financing projects PUT 1369 “Adaptation mechanisms of diamond films in dry sliding wear” (1.01.2017–31.03.2021), and IUT19-29 “Multi-scale structured ceramic-based composites for extreme applications (1.01.2014–31.12.2019)”.

Abstract

Tribological behavior of hybrid coatings at extreme conditions

High hardness and wear resistance, low coefficient of friction and chemical inertness are the key properties of coatings used for the protection of cutting tools and moving parts. Under high-speed dry machining in air, a severe failure can occur due to an atmospheric oxygen attack of the coating surface. Therefore, one of the main challenges is the protection of the cutting tools under extreme conditions.

Previous studies of the tribological properties of diamond coatings in Tallinn University of Technology have addressed the formation of a carbonaceous layer, ripples and grooves patterns on the wear scars surface and the deflection of coatings during sliding tests. These results indicate that self-organization takes place in the tribo-system. On the other hand, an effective protection of the carbon-based coatings is required for high temperature applications. Therefore, the aim of the PhD study is to assess the effect of a thin adaptive oxide layer on the tribological properties of coatings, especially at high temperatures.

The main **objectives** of the present research are as follows.

- Development of the approach based on the preparation of a thin oxide layer on top of a coating that acts as a passivation layer against oxidation attack at high temperatures
- Investigation of the effect of oxide layer adaptability and superlubricity
- Investigation of the effect of coating deflection
- Understanding of friction and wear using the principles of self-organization and self-organized critically

The coatings were deposited by physical vapor deposition (PVD) and plasma assisted chemical vapor deposition (PACVD) methods on SCD(110) and WC-Co substrates. The thin oxide layer was prepared by the atomic layer deposition (ALD) technique on top of the coating surface. The tribological properties of the coatings were analyzed at room and elevated temperatures. Raman spectroscopy, XRD, SEM/EDS, XPS, optical microscopy, nanoscratch, nanoindentation and mechanical profilometry were used for the characterization of the specimens.

The main **outcomes** of the present research are as follows.

1. It is shown that the thermal stability of the hydrogenated amorphous carbon doped with the Si (a-C:H:Si) coating improved by the deposition of a thin Al_2O_3 layer on top of the a-C:H:Si coating.
2. The adaptation effect was demonstrated by the deposition of thin alumina layer on a-C:H:Si coatings, specifically, during the running-in period, the contact area between the tribo-pairs increases, which results in the decrease of the contact pressure.
3. The superlubricity was observed during the sliding tests on $\text{Al}_2\text{O}_3/\text{a-C:H:Si}$ at 400 °C with the CoF values < 0.01.
4. The coating deflection was observed on the hard multilayer coating (HMC) and a-C:H:Si coatings in the sliding tests. In the case of HMC, the deflection was greater in the tests at RT and 600 °C as compared to the test at 800 °C. These results are explained by the presence of the fcc-(Al,Cr) $_2\text{O}_3$ at lower temperatures. This phase is less stable as compared to α -(Al,Cr) $_2\text{O}_3$ formed at 800 °C.
5. The transition from the self-organized criticality (running-in) to self-organization (steady state) was observed on the NCD coating.

Lühikokkuvõte

Hübriidpinnete triboloogiline käitumine ekstreemsetes tingimustes

Pinnete suur kõvadus ja kulumiskindlus, väike hõõrdekoefitsient ja keemiline inertsus on võtmeomadused nende kasutamisel lõikeriistade ja kuluosade korral. Kiirloometöötlemisel kuivalt ja õhu käes võib leida aset lõikeriista rivist väljalangemine, mis on põhjustatud õhuhapniku toimest pindele. Siinjuures on oluline just kaitse oksüdatsiooni vastu ekstreemtingimustes.

Tallinna Tehnikaülikoolis läbiviidud teemantpinnete varasemad tribouuringud on näidanud süsinikusisaldavate kihtide korral säbarlaine- ja vagumustrite teket kulumisel pindadel, aga ka õhukeste teemantpinnete läbipainet liugekulumise tingimustes. Samuti on välja selgitatud teemantpinnete iseorganiseerumise võimalus tribosüsteemides. Teiselt poolt on selgunud süsiniku baasil pinnete efektiivse kaitse vajadus kõrgetemperatuursetes kasutustes. Siit tulenevalt oli seatud doktoritöö ülesandeks selgitada välja õhukese oksiidikihi mõju teemantpinnete triboomadustele, eelkõige kõrgetel temperatuuridel.

Käesoleva uuringu **põhieesmärkideks** olid:

- õhukese oksiidikihi arendus teemantpinnete pealmise kihina, mis toimiks kui passiveeriv kiht oksüdatsioonil kõrgetel temperatuuridel,
- uurida oksiidikihi adaptiivsuse mõju ja supermäärivust,
- uurida oksiidikihi läbipainde mõju,
- uurida iseorganiseerumise põhimõtetest lähtuvalt hõõrde ja kulumise protsesse.

Pinned sadestati füüsikalise (PVD) ja keemilise aursadestuse (PACVD) meetodil Si(100), monokristalse teemant- SCD(110) ja WC-Co kõvasulamalusele. Õhukene alumiiniumioksiidi (Al_2O_3) kiht saadi teemantpindel aatomkihtsadestuse (ALD) teel. Pinnete triboomadusi analüüsiti toa- ja kõrgendatud temperatuuridel. Pinnete karakteriseerimiseks kasutati Raman-spektroskoopia, XRD, SEM/EDS, XPS ja valgusmikroskoopia meetodeid, nanokriipe ja nanoindenteerimise teste ning mehaanilist profilomeetriat.

Käesoleva töö põhilised **tulemused** on järgmised:

1. Näidati, et oksiidikihi pealkandmine parandab a-C:H:Si –ga dopeeritud hüdrokeenitud amorfse süsinik pinde termostabiilsust.
2. Näidati õhukese oksiidikihi adaptiivsuse mõju teemant- ja a-C:H:Si pinnitel, eelkõige sissetöötamise perioodil, mil kontaktpindala tribopaaris suureneb, vähendades kontaktsurvet.
3. Liugekatsetel temperatuuril 400 °C täheldati oksiidikihi olemasolul Al_2O_3 /a-C:H:Si pinnete supermäärivust (hõõrdekoefitsiendi väärtused < 0.01).
4. Multikihtkõvapinnete (HMC) ja teemantpinnete korral täheldati pinnete läbipainet liugekulumisel. HMC pinde korral oli läbipaine suurem toatemperatuuril ja 600 °C juures võrreldes katsetamisega 800 °C juures. See on selgitatav fcc-(Al,Cr) $_2$ O $_3$ struktuuri väiksema stabiilsusega madalamatel temperatuuridel võrreldes a-(Al,Cr) $_2$ O $_3$ struktuuriga temperatuuril 800 °C.
5. NCD pinnete korral täheldati üleminekut iseorganiseerumiskriitilisuselt (sissetöötamise staadiumis) iseorganiseerumisele (püsiolekus).

Appendix

Publicaton I

Alamgir, A., Bogatov, A., Yashin, M. and Podgursky, V., 2019. Mechanical and tribological properties of 100-nm thick alumina films prepared by atomic layer deposition on Si (100) substrates. *Proceedings of the Estonian Academy of Sciences*, 68(2), pp. 126-130.



Mechanical and tribological properties of 100-nm thick alumina films prepared by atomic layer deposition on Si(100) substrates

Asad Alamgir*, Andrei Bogatov, Maxim Yashin, and Vitali Podgursky

Tallinn University of Technology, Department of Mechanical and Industrial Engineering, Ehitajate tee 5, 19086 Tallinn, Estonia

Received 20 December 2018, accepted 11 February 2019, available online 28 March 2019

© 2019 Authors. This is an Open Access article distributed under the terms and conditions of the Creative Commons Attribution-NonCommercial 4.0 International License (<http://creativecommons.org/licenses/by-nc/4.0/>).

Abstract. The study investigates mechanical and tribological properties of alumina (Al_2O_3) films prepared on Si(100) substrates. The 100-nm thick films were deposited by atomic layer deposition. Nanoindentation and nano-scratch tests were performed with Berkovich and sphero-conical diamond indenters, respectively. Energy-dispersive X-ray spectroscopy and optical and scanning electron microscopy were used to analyse the surface morphology and chemical composition of the thin films. X-ray diffraction was used to characterize their crystal structure. Crystallization was found to start at 1100 °C after 3 hours of annealing. The hardness and tribological properties of the alumina films were influenced by the substrate in nanoindentation and nano-scratch tests. Within the relatively low load range (5–50 mN), the coefficient of friction of Si and alumina against diamond depended on the load, most likely due to a change in the elastic/plastic deformation behaviour within the Si substrate.

Key words: nanoindentation, alumina oxide thin films, atomic layer deposition, nano-scratch, deformation.

1. INTRODUCTION

Alumina films are an important technological material used for chemical and mechanical protection of engineering components [1] and in the manufacturing of optical devices and micro-electromechanical systems. Preparation of patterned alumina films is an important aspect of modern technology to study the influence of surface textures on friction and wear [2].

Atomic layer deposition (ALD) is widely used for the preparation of alumina films [3]. Nanoindentation and nano-scratching are well-known methods to determine the mechanical properties of thin films. The nano-hardness of alumina films can vary between 6 and 12 GPa [4,5]. However, there is a lack of investigations of mechanical properties of thin alumina films by the nano-scratch method.

This study focuses on mechanical and tribological properties (within 0.2–400 mN of load) of 100-nm thick alumina films deposited on Si(100).

2. EXPERIMENTAL METHODS

The alumina thin films of 100-nm thickness were prepared on Si(100) substrates by the ALD method with subsequent annealing. The deposition temperature was 300 °C. The temperature and duration of annealing for different samples are shown in Table 1.

The nanoindentation tests were carried out by means of a nano-mechanical testing system (NanoTest, Micro Materials Ltd.) using a diamond Berkovich indenter.

The applied loads were varied between 0.2 and 0.45 mN with the increment of 0.05 mN. The nano-indentation was performed with a series of 10 indentations at each load on each sample. The mechanical properties

* Corresponding author, asadalamgir.shaikh@live.com

Table 1. Post-deposition annealing parameters of films

	Samples					
	1	2	3	4	5	6
Temperature (°C)	25	500	700	900	1100	1100
Time (h)	–	1	1	1	2	3

Table 2. Parameters for nano-scratch tests for Si(100) and Al₂O₃/Si(100) samples

Peak load (mN)	Loading rate, dL/dt (mN/s)	Scan speed, dx/dt (μm/s)	dL/dx (mN/μm)
5, 7, 10, 20, 50, 100, 200, 300, 400	5	2	2.5

of the Si substrate and alumina films, such as the hardness and elastic modulus, were determined by the Oliver–Pharr method [6]. The nano-scratch tests were performed using a sphero-conical diamond indenter with a radius of 5 μm (the tests details are listed in Table 2).

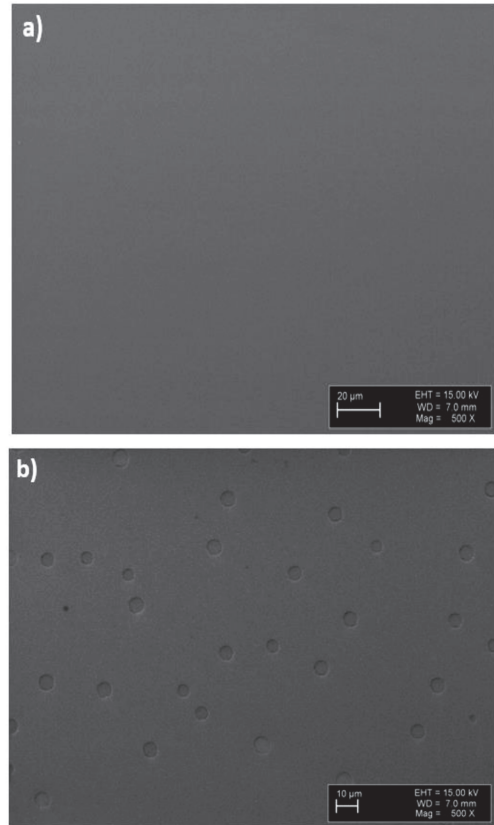
The friction force (F_x) and friction coefficient (COF) were the parameters of interest for nano-scratch tests. The surfaces of samples after the scratch tests were examined by optical microscopy.

3. RESULTS AND DISCUSSION

Scanning Electron Microscopy (SEM) images taken of the Al₂O₃ films are shown in Fig. 1. The as-deposited film (sample 1 in Table 1) has a uniform smooth layer (Fig. 1a). A similar surface morphology was observed after annealing at 500, 700, and 900 °C. The holes within the oxide layer (sample 6) can be seen in the SEM image after annealing at 1100 °C for 3 h (Fig. 1b). This demonstrates how the patterned alumina films can be prepared.

SEM images taken in the backscattered-electron (BSE) mode are shown in Fig. 2a and Fig. 2b along with the energy-dispersive X-ray spectroscopy (EDS) patterns. The spectrum taken within the hole shows a relatively strong Si signal, indicating the peeling of the film after annealing at 1100 °C for 3 h in comparison with the spectrum corresponding to the pristine alumina film surface, which possesses a strong Al peak. The X-ray diffraction (XRD) patterns taken on samples 5 and 6 indicate the formation of a crystalline structure after 3 h of annealing (Fig. 2c). The study of the literature suggests that most likely multiphase alumina was formed [7]. The structure of samples 1–5 was amorphous.

The nanohardness and Young's modulus of the Si(100) substrate were in the range of 10.6–13.2 GPa

**Fig. 1.** Surface morphology of Al₂O₃ films: (a) as-deposited and (b) annealed at 1100 °C for 3 h.

and 142–169 GPa, respectively, which is in good agreement with the literature [8]. The hardness and Young's modulus of as-deposited and annealed at 500, 700, 900, and 1100 °C alumina films were in the range of 10–13 GPa and 150–190 GPa; thus the Si(100) substrate influenced the properties of the alumina films (Table 3).

The scratch test on the Si(100) substrate, illustrated in Fig. 3, was performed at the peak load of 200 mN. The results of the scratch test are in good agreement with the literature [9]. The main transitions on the Si substrate are as follows: L_y – onset of non-elastic deformation, L_{c1} – pop-in observed by an accompanied change in the colour of the scratch track, and L_{c2} – prominent chipping observed at the edges of the track.

The behaviour of alumina film (sample 1) under the peak load of 200 mN is shown in Fig. 4a. Chipping starts at $L_{c2} = 78$ mN. The response of Al₂O₃ film

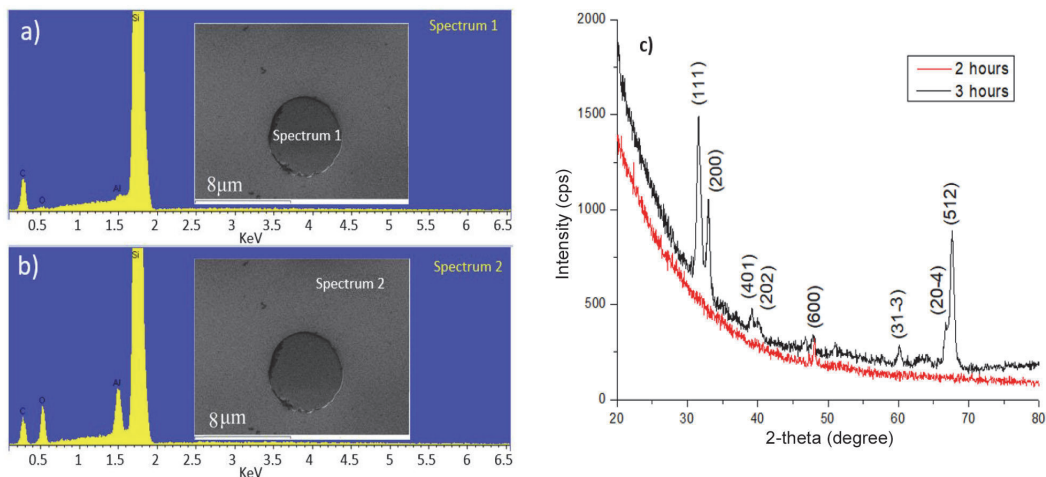


Fig. 2. BSE images and EDS spectra taken on sample 6: (a) within the hole, (b) on the film surface, and (c) XRD pattern after 2 and 3 hours of annealing at 1100 °C.

Table 3. Hardness (GPa) and Young's modulus (GPa) measured on the Si(100) and alumina films

	Si	1	2	3	4	5	6
Nanohardness	11.9 ± 1.3	10.2 ± 1	10.5 ± 1	9.9 ± 0.9	10.4 ± 0.9	12.6 ± 1.4	12 ± 0.9
Young's modulus	154.4 ± 12.9	172.3 ± 19.4	178.1 ± 19	171.0 ± 15	173.8 ± 16.7	169.6 ± 20.6	173.9 ± 20

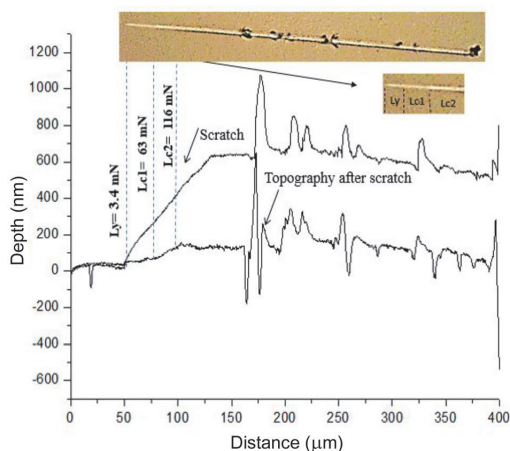


Fig. 3. Nano-scratch test on the Si substrate at the peak load of 200 mN.

(sample 6) at the peak load of 200 mN is shown in Fig. 4b; no clear LC_1 transition was observed. Chipping starts at $LC_2 = 89$ mN. There is a good correlation with the value of 63 mN (LC_1) observed on Si(100), which

shows the influence of substrate on the properties of alumina films, i.e. when severe deformation starts within the Si substrate.

Figure 5a shows that there is a correlation between the normal load and friction force. According to Amontons' law of friction, the friction force is directly proportional to the normal load $F_x = \mu N$, where F_x denotes frictional (tangential) force, N is normal load, and μ is the coefficient of friction. The COF is the coefficient of proportionality and it is independent of load [10,11]. Figure 5b shows COF versus normal load. It should be noted that the COF value increased for alumina and Si within stage 1, which is a disagreement with Amontons' law of friction. According to data shown in Figs 3 and 4, the elastic deformation as well as plastic deformation dominated in this stage. Most likely, the COF value changed due to the mainly continuous change of the elastic–plastic behaviour of Si. Therefore, contact conditions between the indenter and sample surface changed continuously as well. However, for stage 2, the COF values were nearly constant; such behaviour shows agreement with the above-mentioned law of friction.

The plastic deformation and wear (chipping) were dominant processes for stage 2 (Figs 3 and 4). The COF

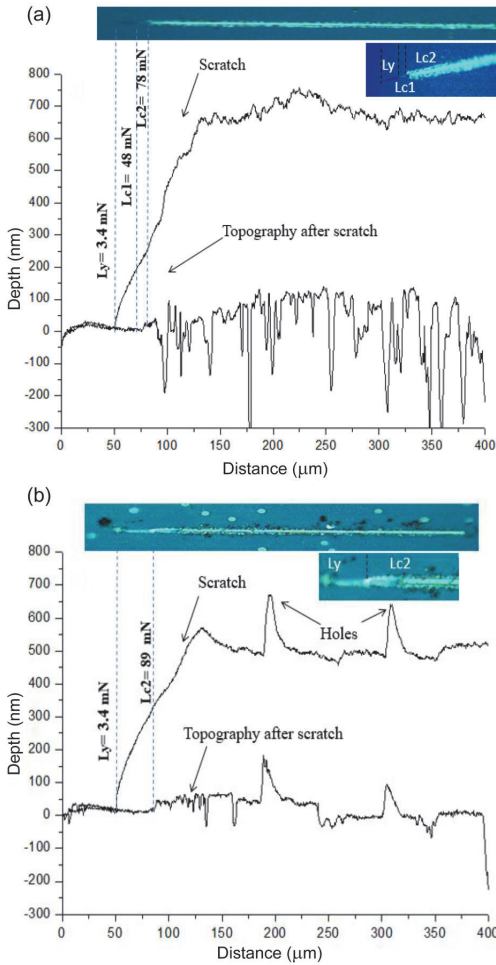


Fig. 4. Nano-scratch tests on alumina along with traces taken by means of optical microscopy: (a) as-deposited sample 1 and (b) sample 6.

for Si(100) substrate within the load range of 200–400 mN was 0.1, which is in good agreement with the literature [12]. The dependence of the COF values on the load between alumina and diamond in sliding tests was observed in previous studies as well [13]. There is a clear difference between COF values for alumina and Si for low loads (5–20 mN), where the elastic–plastic deformation dominated (Figs 3 and 4). In other words, in spite of the strong influence of the substrate observed in nanoindentation tests even for the lower loads (up to 0.45 mN), see discussion above, the tribological properties of alumina differed from those for the Si substrate in nano-scratch tests. The difference in COF values for

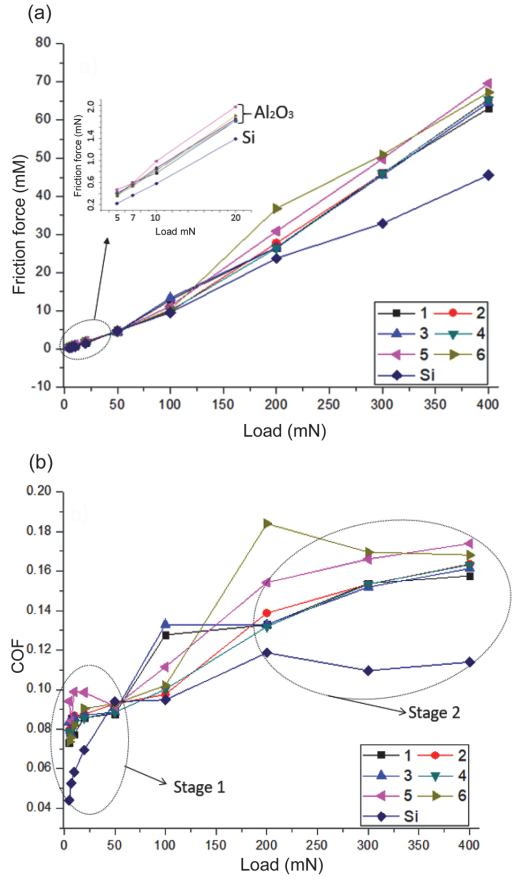


Fig. 5. Friction parameters at nano-scratch tests: (a) friction force and (b) COF versus load curves.

higher loads (200–400 mN), where severe wear was the dominant process, probably means that the alumina films were not fully delaminated from Si substrates.

4. CONCLUSIONS

Nanoindentation and nano-scratch tests were performed to evaluate the mechanical and tribological properties of thin alumina films deposited on Si(100) substrates. The measurements of hardness and Young’s modulus of Al₂O₃ thin films were influenced by the Si substrate. After annealing at 1100 °C, formation of holes within Al₂O₃ films was observed. Disagreement with Amontons’ law of friction was found for the loads in the range of 5–20 mN, which probably corresponds to a continuous change from elastic to plastic deformations within the Si

substrate. However, for the higher loads (200–400 mN), where the wear is the dominant process, a good agreement was found with Amontons' law.

ACKNOWLEDGEMENTS

This study was financially supported by the Estonian Ministry of Education and Research under target financing project IUT 19-29 'Multi-scale structured ceramic-based composites for extreme applications' and was partially supported by the European Regional Development Fund project 'Emerging orders in quantum and nanomaterials' (TK134), Estonian Academy of Sciences (SLTFYPROF), and Estonian Research Agency (PRG4).

Special thanks to Taivo Jõgiaas, PhD (Laboratory of Technology Thin Film, University of Tartu, Estonia), for supplying the samples and constructive reviewing of the manuscript.

The publication costs of this article were covered by the Estonian Academy of Sciences.

REFERENCES

1. Li, X., Diao, D., and Bhushan, B. Fracture mechanisms of thin amorphous carbon films in nanoindentation. *Acta Mater.*, 1997, **45**, 4453–4461.
2. Gachot, C., Rosenkranz, A., Hsu, S. M., and Costa, H. L. A critical assessment of surface texturing for friction and wear improvement. *Wear*, 2017, **372**, 21–41.
3. Leskelä, M. and Ritala, M. Atomic layer deposition (ALD): from precursors to thin film structures. *Thin Solid Films*, 2002, **409**(1), 138–146.
4. Miller, D. C., Foster, R. R., Jen, S. H., Bertrand, J. A., Cunningham, S. J., Morris, A. S., et al. Thermo-mechanical properties of alumina films created using the atomic layer deposition technique. *Sensor. Actuat. A-Phys.*, 2010, **164**, 58–67.
5. Tripp, M. K., Stampfer, C., Miller, D. C., Helbling, T., Herrmann, C. F., Hierold, C., et al. The mechanical properties of atomic layer deposited alumina for use in micro- and nano-electromechanical systems. *Sensor. Actuat. A-Phys.*, 2006, **130**, 419–429.
6. Oliver, W. C. and Pharr, G. M. An improved technique for determining hardness and elastic modulus using load and displacement sensing indentation experiments. *J. Mater. Res.*, 1992, **7**, 1564–1583.
7. Nayar, P., Khanna, A., Kabiraj, D., Abhilash, S. R., Beake, B. D., Losset, Y., and Chen, B. Structural, optical and mechanical properties of amorphous and crystalline alumina thin films. *Thin Solid Films*, 2014, **568**, 19–24.
8. Boyd, E. J. and Uttamchandani, D. Measurement of the anisotropy of Young's modulus in single-crystal silicon. *J. Microelectromech. S.*, 2012, **21**, 243–249.
9. Beake, B. D., Liskiewicz, T. W., and Smith, J. F. Deformation of Si(100) in spherical contacts – comparison of nano-fretting and nano-scratch tests with nano-indentation. *Surf. Coat. Tech.*, 2011, **206**, 1921–1926.
10. Wong, M. S., Meilunas, R., Ong, T. P., and Chang, R. P. H. Tribological properties of diamond films grown by plasma-enhanced chemical vapor deposition. *Appl. Phys. Lett.*, 1989, **54**, 2006–2008.
11. Bhushan, B., Subramaniam, V. V., Malshe, A., Gupta, B. K., and Ruan, J. Tribological properties of polished diamond films. *J. Appl. Phys.*, 1993, **74**, 4174–4180.
12. Bhushan, B. and Li, X. Micromechanical and tribological characterization of doped single-crystal silicon and polysilicon films for microelectromechanical systems devices. *J. Mater. Res.*, 1997, **12**, 54–63.
13. Yurkov, A. L., Skvortsov, V. N., Buyanovsky, I. A., and Matvievsky, R. M. Sliding friction of diamond on steel, sapphire, alumina and fused silica with and without lubricants. *J. Mater. Sci. Lett.*, 1997, **16**, 1370–1374.

Si(100) substraatilede aatomkihtsadestamisel valmistatud 100 nm paksusega Al₂O₃ kilede mehaanilised ja triboloogilised omadused

Asad Alamgir, Andrei Bogatov, Maxim Yashin ja Vitali Podgursky

Si(100) substraatilede sadestatud õhukeste alumiiniumoksiidi pinnete mehaaniliste ja triboloogiliste omaduste hindamiseks viidi läbi nanoindentatsioon- ning nanokriimustuste testid. Si substraat mõjub tema pinnale sadestatud õhukeste Al₂O₃ pinnete kõvadusele ja elastsusmooduli väärtusele. Pärast kuumutamist 1100 °C juures täheldati aukude moodustumist Al₂O₃ pinde sees. Lahknevus Amontonsi hõõrdumisseadusega leiti koormuste vahemikust 5–20 mN, mis võib tõenäoliselt vastata pidevale üleminekule elastselt deformatsioonilt plastsele deformatsioonile Si substraadis. Suuremate koormuste (200–400 mN) puhul, kus kulumine on domineeriv protsess, leiti Amontonsi seadusega hea vastavus.

Publication II

Bogatov, A., Podgursky, V., Vagiström, H., Yashin, M., **Shaikh, A.A.**, Viljus, M., Menezes, P.L. and Gershman, I.S., 2019. Transition from Self-Organized Criticality into Self-Organization during Sliding Si₃N₄ Balls against Nanocrystalline Diamond Films. *Entropy*, 21(11), p. 1055.

Article

Transition from Self-Organized Criticality into Self-Organization during Sliding Si₃N₄ Balls against Nanocrystalline Diamond Films

Andrei Bogatov ^{1,*}, Vitali Podgurski ¹, Heinar Vagiström ¹, Maxim Yashin ¹, Asad A. Shaikh ¹, Mart Viljus ¹, Pradeep L. Menezes ² and Iosif S. Gershman ³

¹ Department of Mechanical and Industrial Engineering, Tallinn University of Technology, Ehitajate tee 5, 19086 Tallinn, Estonia; vitali.podgurski@ttu.ee (V.P.); heinar.vagistrom@taltech.ee (H.V.); mayash@ttu.ee (M.Y.); asadalamgir.shaikh@live.com (A.A.S.); mart.viljus@taltech.ee (M.V.)

² Department of Mechanical Engineering, University of Nevada Reno, Reno, NV 89557, USA; pmenezes@unr.edu

³ Joint Stock Company Railway Research Institute, Moscow State Technological University “Stankin” (MSTU “STANKIN”), 3rd Mytischinskaya Street 10, 129851, 127994, GSP-4, Moscow, Vadkovsky lane 1, Moscow, Russia; isgershman@gmail.com

* Correspondence: andrei.bogatov@mail.ru; Tel.: +372-56506423

Received: 9 October 2019; Accepted: 24 October 2019; Published: 28 October 2019



Abstract: The paper investigates the variation of friction force (F_x) during reciprocating sliding tests on nanocrystalline diamond (NCD) films. The analysis of the friction behavior during the run-in period is the focus of the study. The NCD films were grown using microwave plasma-enhanced chemical vapor deposition (MW-PECVD) on single-crystalline diamond SCD(110) substrates. Reciprocating sliding tests were conducted under 500 and 2000 g of normal load using Si₃N₄ balls as a counter body. The friction force permanently varies during the test, namely F_x value can locally increase or decrease in each cycle of sliding. The distribution of friction force drops (dF_x) was extracted from the experimental data using a specially developed program. The analysis revealed a power-law distribution $f^{-\mu}$ of dF_x for the early stage of the run-in with the exponent value (μ) in the range from 0.6 to 2.9. In addition, the frequency power spectrum of F_x time series follows power-law distribution $f^{-\alpha}$ with α value in the range of 1.0–2.0, with the highest values (1.6–2.0) for the initial stage of the run-in. No power-law distribution of dF_x was found for the later stage of the run-in and the steady-state periods of sliding with the exception for periods where a relatively extended decrease of coefficient of friction (COF) was observed. The asperity interlocking leads to the stick-slip like sliding at the early stage of the run-in. This tribological behavior can be related to the self-organized criticality (SOC). The emergence of dissipative structures at the later stages of the run-in, namely the formation of ripples, carbonaceous tribolayer, etc., can be associated with the self-organization (SO).

Keywords: NCD; friction; self-organized criticality; self-organization

1. Introduction

Amonton’s law states that friction force is linearly related to the normal load:

$$F_x = kF_z \quad (1)$$

where F_x is friction force, k —coefficient of friction (COF) and F_z —normal load. On the other hand, friction is a complex phenomenon involving a number of processes, including deformation and fracture of surface asperities, adhesion, abrasion, chemical interactions, tribolayer formation, etc. These

processes contribute to friction at different scales (nano-, micro- and macroscale) and hierarchy levels (molecular, surface asperity, component) [1]. Therefore, the frictional systems are essentially not strictly linear, because the COF may depend on many factors including normal load.

The energy (W) induced by external loading (mechanical work) is accumulated into the tribosystem (ΔE) and converted into the heat (Q).

$$W = Q + \Delta E, \quad (2)$$

The accumulated energy can be consumed by different processes including wear of material and generation of self-organizing (SO) dissipative structures (DS). SO with DS can influence the friction and wear [2].

Entropy production ($\partial S/\partial t$) is a useful concept for characterization of friction and wear, which are dissipative and irreversible processes. The entropy production of a system is the sum of the entropy production of processes occurring within the system. Moreover, according to the second law of thermodynamics, it is impossible to distinguish a part of the system at the macro-, micro- or nanoscale, in which the entropy production would be negative [3]:

$$\frac{d_i S}{dt} = \sum_n \frac{d_i S_{n\text{micro}}}{dt} = \sum_n \frac{d_i S_{n\text{nano}}}{dt}. \quad (3)$$

In systems far from thermodynamic equilibrium, entropy production can decrease due to SO with formation of DS. SO with DS can occur only after loss of thermodynamic stability [4]. The stability conditions for the thermodynamic system are given in the variational form by

$$\frac{\partial}{\partial t}(\delta^2 S) \geq 0, \quad (4)$$

where $\delta^2 S$ is the second variation of entropy. When Equation (4) is not fulfilled, SO can occur [5]. The SO is often characterized by the formation of a thin tribolayer at the friction surface [2]. It is estimated that more than 90% of the externally induced energy (ΔE in (2)) can be accumulated within the film surface [2,6]. In our previous work, the sliding of nanocrystalline diamond (NCD) films against Si_3N_4 balls was investigated [7]; it was shown that the initial polishing mechanism could not be related with SO, and SO can occur only after a run-in period. The formation of carbonaceous tribolayer, regular ripple patterns on the film surface and plastic deformation of the entire film during sliding, are examples of the SO structures [8].

Experimental and theoretical studies show that there are systems with many degrees of freedom, which can evolve into self-organized critical (SOC) state. This state is characterized by the release of energy through rapid relaxation processes (avalanches). The relation between the avalanche size (A) and the number of avalanches of the same size (n) can be described by the power law:

$$n = A^{-\mu}, \quad (5)$$

where μ is an exponent characterizing the distribution of avalanches with different sizes [9,10]. A well-known example of the SOC system is a sand pile model [11] where grains of sand are randomly placed into a pile until the slope reaches a critical value. Further addition of grains triggers an avalanche affecting adjacent grains. Nosonovsky et al. [5] state that unlike SO systems, SOC systems are constantly “tuned” to a state whereby an avalanche can be initiated again.

Another example of the SOC system is a stick-slip friction between rubbing surfaces [9,12,13]. An indication of SOC is the power-law distribution of friction force drops (dF_x) [9]. Some authors suggest strengthening conditions for SOC, namely the presence of frequency power spectra of F_x time series and the existence of stationary state at long times [12,14].

The wear on diamond films is a load- and velocity-dependent process [15,16]. The most influential factors are anisotropy of mechanical and tribological properties [17], the ambient atmosphere [18,19], surface morphology [20,21], etc. It was suggested that due to considerable shear stress present at the

diamond-counter body interface, it becomes energetically more favorable for the diamond bonding to rehybridize to the sp^2 configuration [22,23], thus contributing to formation of an amorphous carbonaceous lubricating tribolayer [15,24]. The surface morphology of diamond films plays a vital role during the run-in period in sliding wear tests, namely surface asperities interlock with counter body surface asperities, resulting in material fracture followed by micro-plowing and self-polishing wear mechanisms on the diamond film surfaces [20,21,25,26].

It is worth mentioning the hierarchical character of the wear of the diamond films. The Hertz contact pressure is calculated on the macro-level (i.e., mm), corresponding to the contact tribology [27]. However, different processes occurring on contact spots (hot-spots) between the ball and surface asperities are aspects of the asperity tribology (micro-level, i.e., μm) [27]. The characteristic sizes of ripple patterns observed in wear tracks on diamond films are in nanometer to micrometer ranges, as the length of a ripple can reach several microns and more, and the height is in nm range [8,26]. Formation of an amorphous carbonaceous lubricating layer due to stress-induced mechanochemical amorphization [15] and passivation of dangling bonds of carbon atoms produced during sliding by species from the ambient environment [14] occur on the atomic scale.

The present study aims to investigate the distribution of the friction force drops obtained after sliding tests with Si_3N_4 balls against nanocrystalline diamond (NCD) films grown on single-crystalline diamond SCD(110) substrates (NCD/SCD(110)). It allows us to carry out a more detailed analysis of friction behavior during the initial run-in period and to show early stages of formation of dissipative structures.

2. Materials and Methods

The NCD films (samples n2–n9) were grown on the SCD(110) substrates using the microwave plasma-enhanced chemical vapor deposition (MW-PECVD) method, see details in our previous study [28]. The coating thickness was 2.2 (samples n4 and n5), 8 (n6 and n7), 10.5 (n2 and n3), 14 (n9) and 22.5 μm (n8), respectively (Table 1). The root mean square surface roughness (S_q) was evaluated using atomic force microscopy (Bruker MultiMode[®] 8 AFM). Scanning electron microscopy images were obtained using Zeiss EVO[®] MA 15 system with LaB_6 cathode in secondary electron mode, accelerating voltage 15 kV, working distance 5–7 mm.

Table 1. Thickness and surface roughness of samples and normal loads used in the tribological tests.

Sample	n4	n5	n6	n7	n2	n3	n9	n8
Normal load [g]	500	2000	500	2000	500	2000	500	2000
Coating thickness [μm]	2.2			8		10.5	14	22.5
Roughness S_q [μm]	33		55		56		66	78

Reciprocating sliding tests [29] were performed by means of CETR[®] UMT-2 tribometer using Si_3N_4 balls (surface roughness $R_a = 0.012 \mu\text{m}$, data provided by the manufacturer, REDHILL[®]). The displacement distance was 1 mm, frequency 5 Hz, and normal load was 500 and 2000 g (Table 1). The duration of tests was 600, 1200, 1800, 7200 and 14,400 s. Tests were conducted at room temperature and relative humidity of 35%.

Tangential or friction (F_x) and normal (F_z) forces, displacement distance, duration of the test, and COF values were recorded in a text file in the course of the reciprocating sliding test. An example of F_x behavior in a reciprocating sliding test is shown in Figure 1. Friction force drops are marked with a bold line on the plot. The number and size of F_x drops can differ per each half cycle. Because the direction of motion changes periodically, the friction force sign changes every half cycle. Therefore, friction force values measured in the vicinity of the points where the velocity is equal to zero should be excluded from the analysis (Figure 1). In the present study, the main focus is on the distribution of smaller dF_x values. However, the width of the excluded time intervals can influence only the number

of the highest dFx values. In other words, the analysis did not reveal the dependence of the distribution of Fx drops on excluded time interval width.

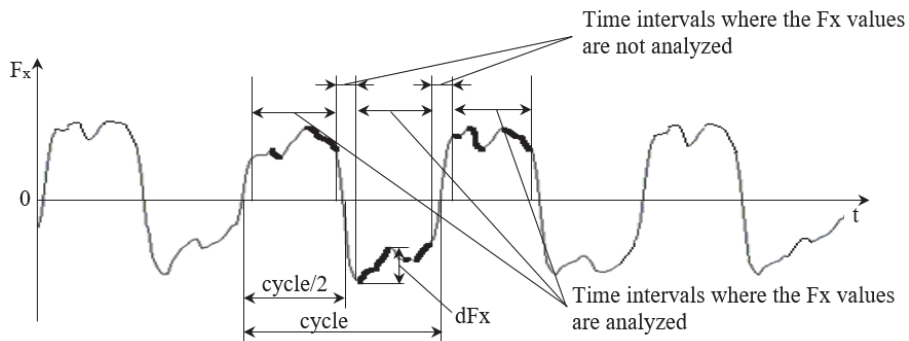


Figure 1. Example of friction force (Fx) behavior in reciprocating sliding test and data selection used in analysis.

The frequency power spectrum of Fx time series was calculated using Statistica® software.

3. Results and Discussion

Figure 2 shows COF vs. time curves obtained on the NCD/SCD(110) specimen n3. The shape of the curves differs for different tests, although no test conditions were changed. The reason for the variation of the shape of the COF curves was discussed in our previous work [7]. It was found that two typical types of COF vs. time curves are observed in sliding tests on the diamond films at room temperature due to bifurcation occurring after the initial run-in. The number of spikes of different intensity is particularly high during the first 800 s of sliding indicating frictional instabilities.

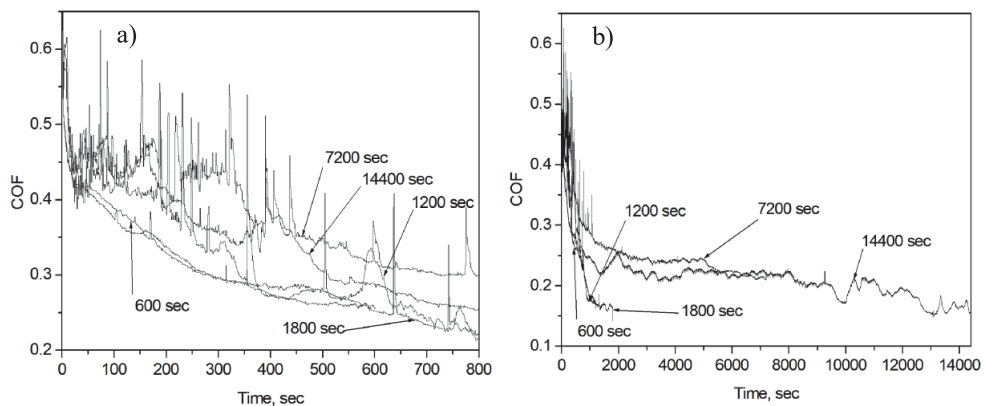


Figure 2. Coefficient of friction (COF) vs. time curves obtained on sample n3. Test duration is 600, 1200, 1800, 7200 and 14,400 s: first 800 s (a) and full-length (b).

Investigation of the surface of the wear scars revealed the formation of ripple patterns within the wear scars similar to ones observed in our previous studies [7,26]. A specific interest of the present investigation was an estimation of the initial sliding period when the first ripples start to form on the surface. Therefore, shorter sliding tests were carried out as well. Figure 3 shows SEM images taken of the surface of the wear scars after the sliding tests on sample n3. The duration of the tests was between 600 and 14,400 s, and the normal load was 2000 g. A network of ripples was observed

after the first 600 s of sliding and for all following stages of the sliding regardless of the test duration. No fragmentation of the network into isolated ripples as well as disappearance of ripples was found. Formation of some ripples on top of the surface asperities can probably be expected before 600 s of sliding as well. Smoothing of NCD surface and formation of the continuous network of ripples on the surface was found after 1800 s of sliding (Figure 3d). There is an influence of the test duration on the shape and density of the ripples, compare for instance Figure 3c,e. It is worth stressing that the formation of ripple patterns is a continuous process, i.e., new patterns continuously formed in the course of the increase of the wear scar depth. There is a difference between the ripple pattern morphology observed in the present study and on the NCD films prepared on Si(100) substrate [7]. Namely, a network of interconnected ripples that was formed at the early stage of sliding was finally disintegrated into isolated ripples at the later stage. The understanding of the mechanisms causing morphological changes during sliding needs further research, which should include development of the self-organization theory, estimation of the influence of substrate properties and the structure of the diamond films.

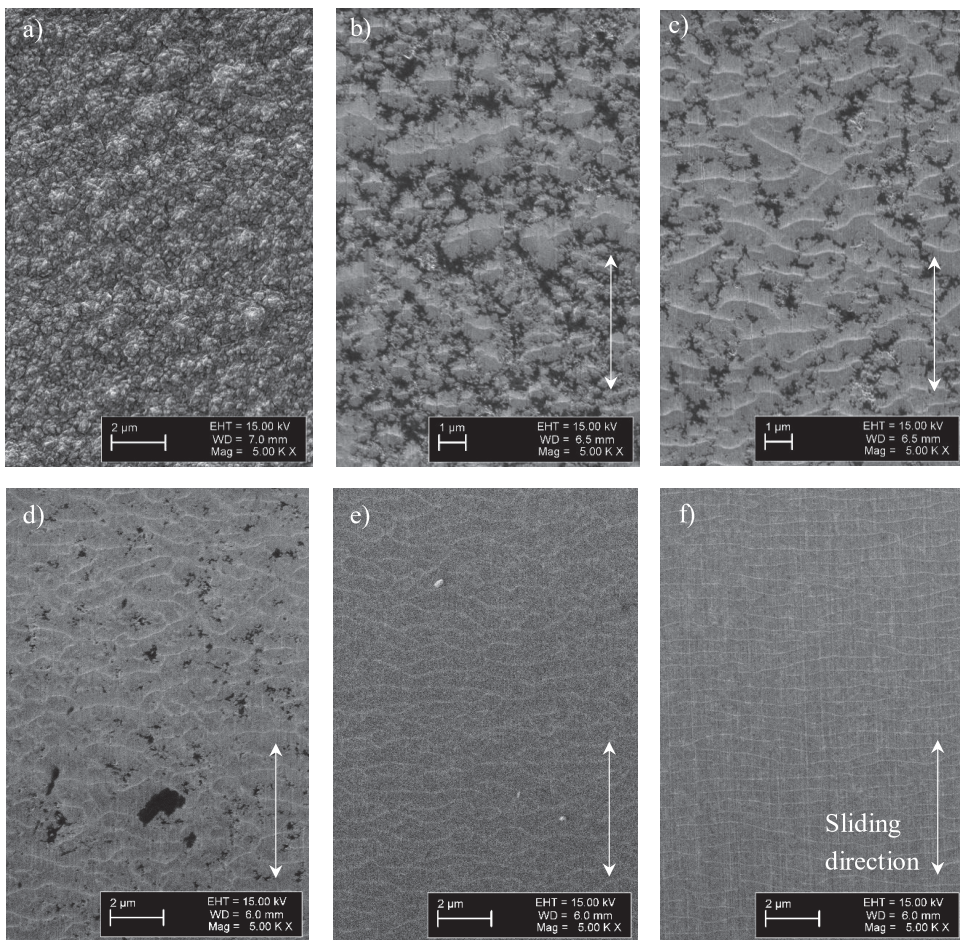


Figure 3. Ripple patterns observed on sample n3: pristine surface (a) and wear scars surface after the tests with the load of 2000 g and sliding time of 600 (b), 1200 (c), 1800 (d), 7200 (e) and 14,400 s (f).

The characteristic behavior of F_x value during a sliding cycle is shown in Figure 4. A common feature is the existence of F_x peaks at the beginning (peak 1) and the end (peak 2) of the half cycle. The peak at the beginning is due to the fact that the coefficient of static friction is always greater than the coefficient of sliding friction. In most cases, the height of peak 1 is smaller than that of peak 2, and the height of both peaks is highest for the initial period of the run-in, i.e., for 0–600 s of sliding. The height of both peaks continuously decreases for longer periods of sliding and finally remains approximately constant after 1800 cycles. The variation of F_x value indicates stick-slip motion during sliding (Figures 1 and 4).

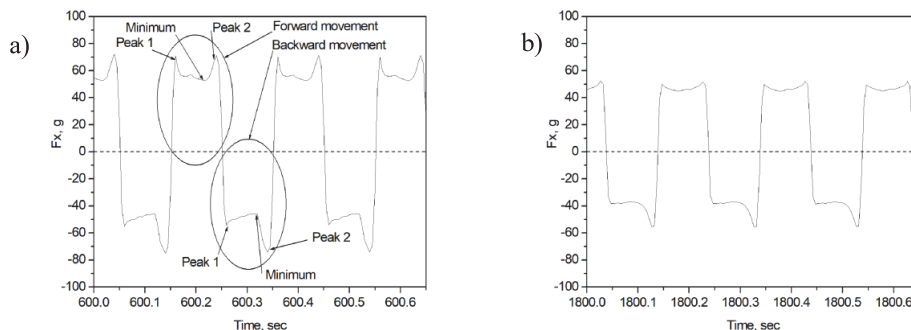


Figure 4. F_x vs. time curves recorded in the test with 2000 g of load after 600 (a) and 1800 s (b) of sliding on sample n3.

The distribution of dF_x was extracted from the experimental data (Figure 5). The distributions obtained after the tests with 2000 g of load are shifted to the higher values of dF_x in contrast to the distributions for 500 g of load (Figure 5b). This could indicate the existence of a threshold in the stick-slip system, which resembles the threshold for a sand pile slope angle in the “sand pile model” when a sudden avalanche occurs [5]. The type of distributions of F_x drops (or dF_x) was estimated for different periods of sliding tests. For all samples under investigation (n2–n9), the behavior of log-log plots for the initial run-in period (0–600 s) was linear, i.e., it follows power-law distribution $f^{-\mu}$ with exponent μ , see examples for samples n3 and n5 (Figure 6a,c). The μ value varied in the range of 0.6–2.9. This may indicate a presence of SOC in dry sliding friction between NCD and Si_3N_4 during the initial run-in period [9]. However, the log-log distributions of dF_x obtained for other time intervals do not show power-law behavior, see examples for the period from 6600 to 7200 s of sliding (Figure 6b,d).

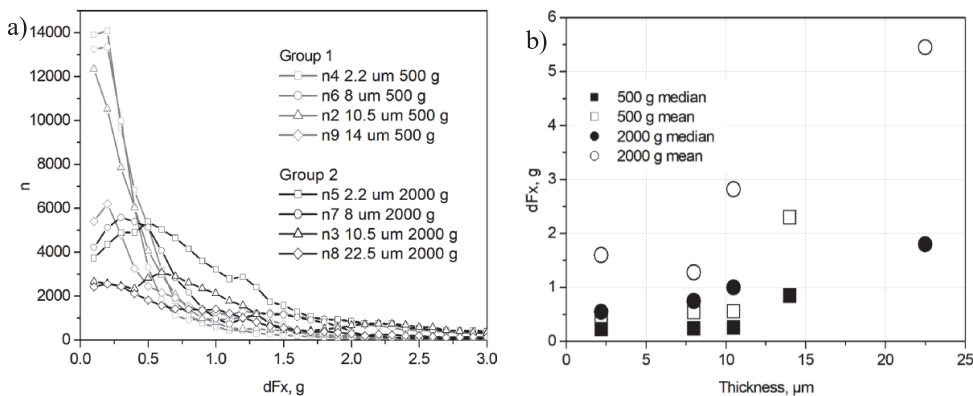


Figure 5. Distributions of dF_x obtained for the first 600 s of the 1800 s length tests with the load of 500 and 2000 g (a) and median and mean values of the same distributions (b).

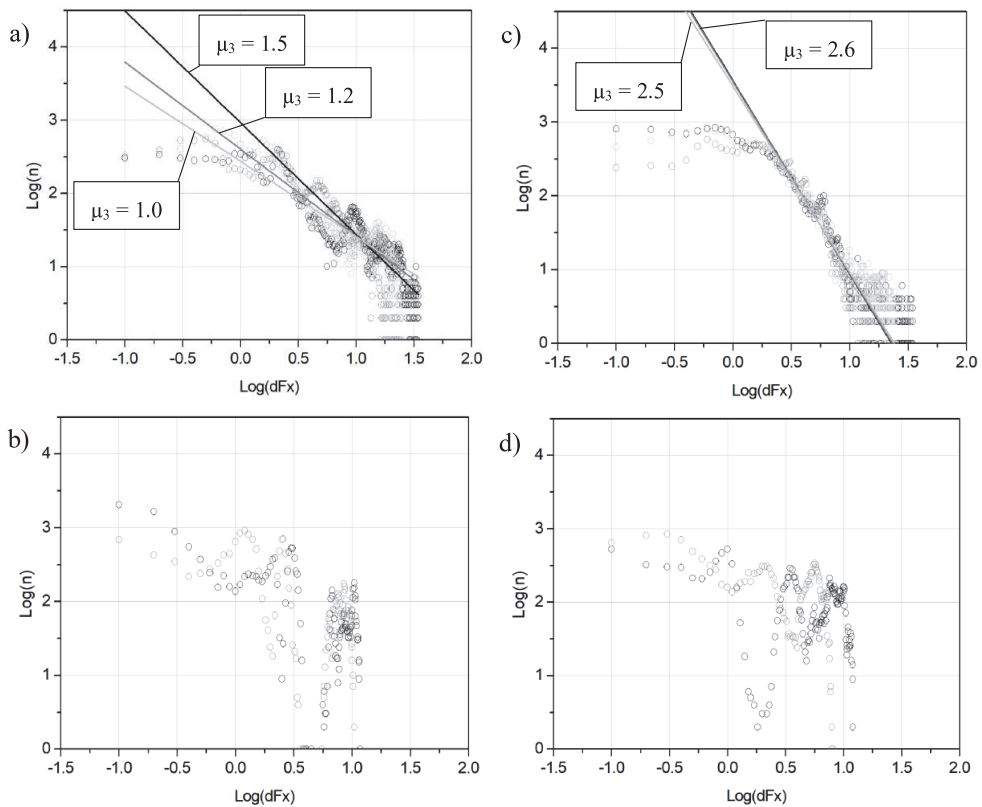


Figure 6. Log-log distributions of dFx for samples n_3 and n_5 (10.5 and 2.2 μm) after the next periods of sliding: n_3 0–600 s (a), n_3 6600–7200 s (b), n_5 0–600 s (c) and n_5 6600–7200 s (d). The data were obtained after 1800, 7200 and 14,400 s tests with 2000 g of load.

The frequency power spectrum density of Fx time series was calculated as well, and the results are shown in Figure 7. The $f^{-\alpha}$ behavior was found with α value between 1.0 and 2.0. Values in the range of 1.5–2.0 were found for the initial run-in (0–600 s) and periods with a fast decrease of the COF value (Figure 8). These values are in good agreement with data in the literature [9]. For the sliding period between 600–1200 s, the α value varies in the range of 1.0–2.0, which is different from the period corresponding to the first 600 s of sliding. It was also found that the α value was about 1.0–1.2 for the sliding period, where the COF value only slightly varied, i.e., during a steady-state period of sliding (Figure 8). For some periods of sliding the $f^{-\alpha}$ behavior was undetectable.

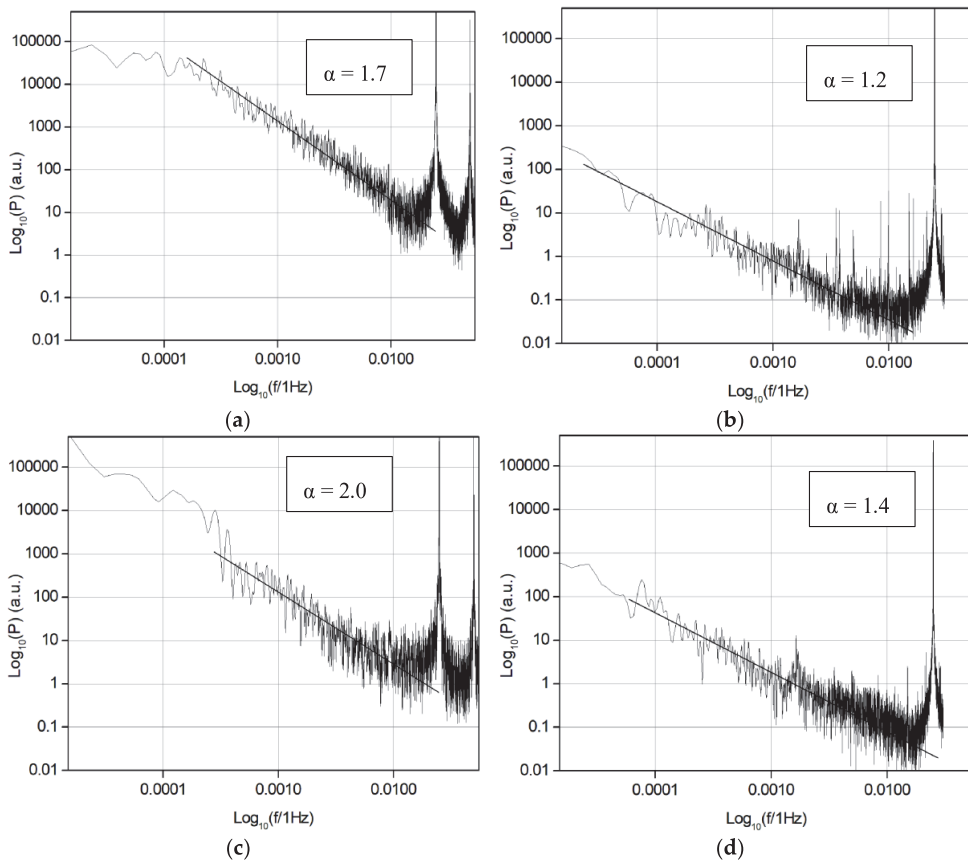


Figure 7. Frequency power spectra for samples n3 and n5 (10.5 and 2.2 μm). The data obtained after the 14,400 s tests with 2000 g of load and analyzed for the next periods of sliding: n3 0–600 s (a), n3 6600–7200 s (b), n5 0–600 s (c) and n5 6600–7200 s (d).

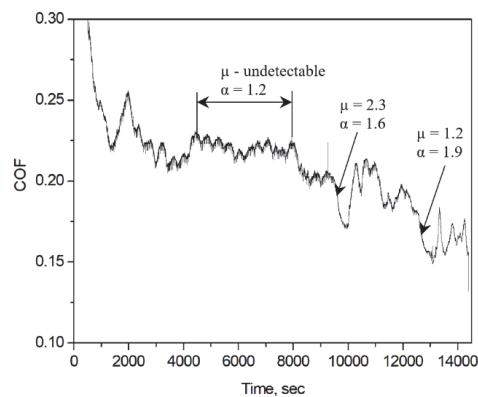


Figure 8. COF vs. time curve obtained on sample n3 (test for 14,400 s shown in Figure 2) and the values of exponents μ and α for different periods of sliding.

The power law distribution of dFx can be observed after the initial run-in period as well, namely for the time intervals where the COF value notably changes, probably due to instabilities during sliding.

For instance, two characteristic periods with a relatively fast decrease of the COF value can be found between 9500–10,000 and 12,000–13,000 s of sliding (Figure 8). Therefore, the tribological system can exist in a SOC state.

The averaged exponent μ estimated for the initial run-in period (0–600 s) is shown in Figure 9. The statistics are obtained on samples (n2–n9) after the sliding tests with different durations; however, only the first part of sliding curves (i.e., first 600 s) were taken into account. The μ value tends to decrease with increasing coating thickness. The roughness of the thicker films is higher than that of thinner ones (Table 1) and the value of friction drops increases with the increase of film thickness (Figure 5b). In other words, mechanical interlocking between counter body asperities is a crucial aspect for the understanding of SOC, in agreement with the conclusion by Zypman et al. [12]. The α value tends to decrease as well with increasing film thickness or increasing surface roughness (Figure 10).

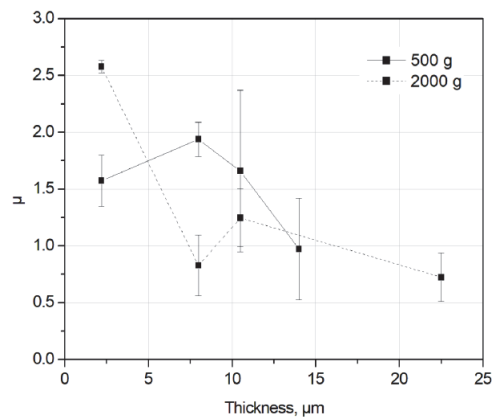


Figure 9. Averaged exponent μ vs. coating thickness for the run-in period (0–600 s).

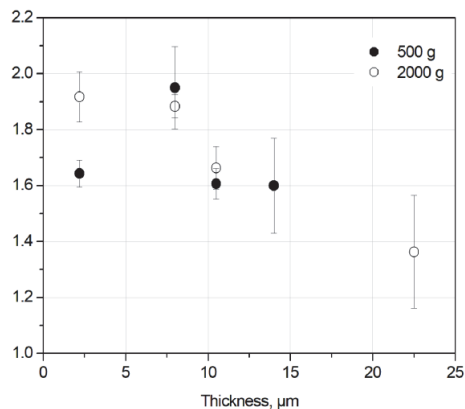


Figure 10. Averaged exponent α vs. coating thickness for the run-in period (0–600 s).

However, the results of the present work differ in some aspects from the results obtained by Zypman et al. [12]. Namely, no power law dFx distribution was found during the steady-state sliding period. This discrepancy can be explained by formation of dissipative (self-organized) structures on the surface of NCD films during sliding. No tribolayer formation and effect of self-organization were discussed in the mentioned study, i.e., the tribological system investigated in the present work differs from one investigated by Zypman et al. [12].

It was mentioned in the Introduction that in order to initiate SO the system must lose thermodynamic stability. The dissipated energy needed to start up this process can be high. In the present study, SOC can be associated with a process that triggers SO. SOC can occur locally to dissipate more energy within a particular place on the surface. The initial run-in period can be characterized by fracture of asperities and self-polishing wear mechanisms, assuming that morphological changes first occur on top of the largest surface asperities, i.e., the dissipation of friction energy takes place locally. This can facilitate formation of DS. The evidence of local formation of ripples on the top of diamond grains can be found in our previous study on microcrystalline diamond films [30]. In other words, the ripples as an indication of DS form at the places where initial SOC effect took place locally. In the course of sliding, SOC occurs subsequently at the smaller asperities, which finally leads to the formation of ripple patterns on the entire surface of the wear scar. Carbonaceous tribolayer forms during these processes, which leads to a lower COF value and smoother sliding for the steady-state period of the tests (compare Figure 2a,b).

The SOC and SO can be distinguished by a different way of releasing mechanical energy induced by external work. SOC is related to the process of energy release through the avalanches, however, dissipation of energy through the formation of tribolayer, ripples formation, etc., on the surface occurs in the case of SO. SOC is characterized by the passage of processes with a positive production of entropy, i.e., the production of entropy increases. SO is characterized by the passage of processes with negative entropy production, i.e., entropy production decreases. In addition, there is a subtle difference between the SOC and SO. As was mentioned in the Introduction, the SOC system is permanently “tuned” to a state whereby an avalanche can be initiated again. In the case of SO with DS, it was found that the formation of ripple patterns is a permanent process, i.e., they are formed at different depths of the wear scars; however, no time gap exists during the sliding when there are no ripples on the wear scar surface. The formation of a new carbonaceous tribolayer is a continuous repeatable process as well [31]. In the present work, the SOC corresponds to initial fracture and polishing of materials or severe wear. In the case of SO, the formation of DS accumulates energy; therefore, only a part of external work is consumed by wear.

Furthermore, it is worth comparing mechanical interlocking with the seizure, which was considered as unconstructive SO in our previous study [7]. A seizure is related to the possibility of the system stopping sliding and was related to an increased adhesion between the counter bodies [2]. SOC investigated in the present study can be related to the mechanical interlocking between counter body asperities, and there is a threshold in stick-slip when the body cannot move. Therefore, it demonstrates the inherent similarity between mechanical interlocking (SOC) and seizure (SO). In addition, it was found that adhesive wear is probably the leading wear mechanism after the run-in period [7], i.e., the wear mechanisms like fracture and initial polishing occurring at the initial run-in (see Introduction) continuously change into adhesive wear.

4. Conclusions

The distribution of friction force drops during reciprocating sliding on NCD/SCD(110) samples against Si_3N_4 balls was analyzed. The power-law type of friction force drops distribution was observed at the initial run-in period of the sliding tests, i.e., during the first 600 s of sliding. This indicates the presence of SOC. The value of exponent μ depends on the roughness of the NCD films. The formation of dissipative structures starts during later stages of the run-in period, i.e., SOC continuously changes into SO. The SOC was not found during the steady-state regime of sliding with an exception for periods where instabilities in sliding occur.

The transition from SOC during the run-in period of sliding to SO during the steady-state period observed in the present study indicates an existence of a class of tribological systems with specific behavior. It differs, for instance, from systems where SOC was found for the steady-state period of sliding.

Author Contributions: Conceptualization, V.P.; methodology, V.P.; software, H.V.; validation, A.B.; formal analysis, A.B., V.P.; investigation, A.B., M.Y., A.A.S., M.V.; resources, V.P.; data curation, A.B.; writing—original draft preparation, A.B.; writing—review and editing, A.B., V.P., P.L.M., I.S.G.; visualization, A.B.; supervision, V.P.; project administration, V.P.; funding acquisition, V.P., I.S.G.

Funding: The work was supported by institutional research funding IUT-19-29 and PUT 1369 of the Estonian Ministry of Education and Research, and grant no. 14.574.21.0179 with unique identification number RFMEFI57417 × 0179 of the Ministry of Science and Higher Education of the Russian Federation.

Acknowledgments: We would like to acknowledge our colleagues V. Ralchenko and V. Sedov for the growth of NCD films on SCD(110) substrates.

Conflicts of Interest: The authors declare no conflict of interest.

References

- Nosonovsky, M.; Bhushan, B. Multiscale friction mechanisms and hierarchical surfaces in nano- and bio-tribology. *Mater. Sci. Eng. R* **2007**, *58*, 162–193. [[CrossRef](#)]
- Fox-Rabinovich, G.S. Principles of friction control for surface-engineered materials. In *Self-Organization during Friction: Advanced Surface-Engineered Materials and Systems Design*; Fox-Rabinovich, G.S., Totten, G.E., Eds.; CRC Press: Boca Raton, FL, USA, 2006; p. 5.
- Kondepudi, D.; Prigogine, I. *Modern Thermodynamics: From Heat Engines to Dissipative Structures*; John Wiley & Sons: New York, NY, USA, 1999; pp. 89–90.
- Kondepudi, D.; Prigogine, I. *Modern Thermodynamics: From Heat Engines to Dissipative Structures*; John Wiley & Sons: New York, NY, USA, 1999; pp. 427–431.
- Nosonovsky, M.; Bhushan, B. Thermodynamics of surface degradation, self-organization and self-healing for biomimetic surfaces. *Philos. Trans. R. Soc. A* **2009**, *367*, 1607–1627. [[CrossRef](#)] [[PubMed](#)]
- Gershman, J.S.; Bushe, N.A. Thin films and self-organization during friction under the current collection conditions. *Surf. Coat. Technol.* **2004**, *186*, 405–411. [[CrossRef](#)]
- Podgursky, V.; Bogatov, A.; Yashin, M.; Sobolev, S.; Gershman, I.S. Relation between self-organization and wear mechanisms of diamond films. *Entropy* **2018**, *20*, 279. [[CrossRef](#)]
- Bogatov, A.; Podgursky, V.; Raadik, A.T.; Kamjula, A.R.; Hantschel, T.; Tsigkourakos, M.; Kulu, P. Investigation of morphology changes on nanocrystalline diamond film surfaces during reciprocating sliding against Si₃N₄ balls. *Key Eng. Mater.* **2014**, *604*, 126–129. [[CrossRef](#)]
- Buldyrev, S.V.; Ferrante, J.; Zypman, F. Dry friction avalanches: Experiment and theory. *Phys. Rev. E* **2006**, *74*, 066110. [[CrossRef](#)] [[PubMed](#)]
- Lacombe, F.; Zapperi, S.; Herrmann, H.J. Force fluctuation in a driven elastic chain. *Phys. Rev. B* **2001**, *63*, 104104. [[CrossRef](#)]
- Bak, P.; Tang, C.; Wiesenfeld, K. Self-organized criticality: An explanation of 1/f noise. *Phys. Rev. Lett.* **1987**, *59*, 381–384. [[CrossRef](#)] [[PubMed](#)]
- Zypman, F.R.; Ferrante, J.; Jansen, M.; Scanlon, K.; Abel, P. Evidence of self-organized criticality in dry sliding friction. *J. Phys. Condens. Matter.* **2003**, *15*, L191–L196. [[CrossRef](#)]
- Slanina, F. Collective behaviour of asperities in dry friction at small velocities. *Phys. Rev. E* **1999**, *59*, 3947–3953. [[CrossRef](#)]
- Konicek, A.R.; Grierson, D.S.; Sumant, A.V.; Friedmann, T.A.; Sullivan, J.P.; Gilbert, P.U.P.A.; Sawyer, W.G.; Caprick, R.W. Influence of surface passivation on the friction and wear behavior of ultrananocrystalline diamond and tetrahedral amorphous carbon thin films. *Phys. Rev. B* **2012**, *85*, 155448–1–155448–13. [[CrossRef](#)]
- Pastewka, L.; Moser, S.; Gumbsch, P.; Moseler, M. Anisotropic mechanical amorphization drives wear in diamond. *Nat. Mater.* **2011**, *10*, 34–38. [[CrossRef](#)] [[PubMed](#)]
- Hird, J.R.; Field, J.E. Diamond polishing. *Proc. R. Soc. A* **2004**, *460*, 3547–3568. [[CrossRef](#)]
- El-Dasher, B.S.; Gray, J.J.; Tringe, J.W.; Biener, J.; Hamza, A.V. Crystallographic anisotropy of wear on a polycrystalline diamond surface. *Appl. Phys. Lett.* **2006**, *88*, 241915–1–241915–3. [[CrossRef](#)]
- Erdemir, A.; Halter, M.; Fenske, G.R.; Zuiker, C.; Csencsits, R.; Krauss, A.R.; Gruen, D.M. Friction and wear mechanisms of smooth diamond films during sliding in air and dry nitrogen. *Tribol. Trans.* **1997**, *40*, 667–675. [[CrossRef](#)]
- Gardos, M.N.; Solano, B.L. The effect of environment on the tribological properties of polycrystalline diamond films. *J. Mater. Res.* **1990**, *5*, 2599–2609. [[CrossRef](#)]

20. Abreu, C.S.; Amaral, M.; Fernandes, A.J.S.; Oliveira, F.J.; Silva, R.F.; Gomes, J.R. Friction and wear performance of HFCVD nanocrystalline diamond coated silicon nitride ceramics. *Diam. Relat. Mater.* **2006**, *15*, 739–744. [[CrossRef](#)]
21. Bhushan, B.; Subramaniam, V.V.; Malshe, A.; Gupta, B.K.; Ruan, J. Tribological properties of polished diamond films. *J. Appl. Phys.* **1993**, *74*, 4174–4180. [[CrossRef](#)]
22. Van Bowelen, F.M.; Enckevort, W.J.P. A simple model to explain the anisotropy of diamond polishing. *Diam. Relat. Mater.* **1999**, *8*, 840–844. [[CrossRef](#)]
23. Van Bowelen, F.M.; Field, J.E.; Brown, L.M. Electron microscopy analysis of debris produced during diamond polishing. *Philos. Mag.* **2003**, *83*, 839–856. [[CrossRef](#)]
24. Chromik, R.R.; Winfrey, A.L.; Lüning, J.; Nemanich, R.J.; Wahl, K.J. Run-in behavior of nanocrystalline diamond coatings studied by in situ tribometry. *Wear* **2008**, *265*, 477–489. [[CrossRef](#)]
25. Holmberg, K.; Ronkainen, H.; Laukkanen, A.; Wallin, K. Friction and wear of coated surfaces – scales, modelling and simulation of tribomechanisms. *Surf. Coat. Technol.* **2007**, *202*, 1034–1049. [[CrossRef](#)]
26. Podgursky, V.; Hantschel, T.; Bogatov, A.; Kimmari, E.; Antonov, M.; Viljus, M.; Tsigkourakos, M.; Vandervorst, W.; Buijnsters, J.G.; Raadik, A.T.; et al. Rippling on wear scar surfaces of nanocrystalline diamond films after reciprocating sliding against ceramic balls. *Tribol. Lett.* **2014**, *55*, 493–501. [[CrossRef](#)]
27. Ronkainen, H.; Koskinen, J.; Varjus, S.; Holmberg, K. Load-carrying capacity of coating/substrate systems for hydrogen-free and hydrogenated diamond-like carbon films. *Tribol. Lett.* **1999**, *6*, 63–73. [[CrossRef](#)]
28. Podgursky, V.; Bogatov, A.; Yashin, M.; Viljus, M.; Bolschakov, A.P.; Sedov, V.; Volobujeva, O.; Mere, A.; Raadik, T.; Ralchenko, V. A comparative study of the growth dynamics and tribological properties of nanocrystalline diamond films deposited on the (110) single crystal diamond and Si(100) substrates. *Diam. Relat. Mater.* **2018**, *92*, 159–167. [[CrossRef](#)]
29. Brostow, W.; Hagg Lobland, H.E. *Materials: Introduction and Applications*; John Wiley & Sons: New York, NY, USA, 2017; pp. 391–427.
30. Bogatov, A.; Traksmaa, R.; Podgursky, V. Changes in surface morphology, deflection and wear of microcrystalline diamond film observed during sliding tests against Si₃N₄ balls. *Key Eng. Mater.* **2016**, *674*, 145–151. [[CrossRef](#)]
31. Podgursky, V.; Bogatov, A.; Sobolev, S.; Viljus, M.; Sedov, V.; Ashkinazi, E.; Ralchenko, V. Effect of nanocrystalline diamond films deflection on wear observed in reciprocating sliding tests. *J. Coat. Sci. Technol.* **2016**, *3*, 109–115. [[CrossRef](#)]





Publication III

Alamgir, A., Yashin, M., Bogatov, A., Viljus, M., Traksmaa, R., Sondor, J., Lümke­mann, A., Sergejev, F. and Podgursky, V., 2020. High-temperature tribological performance of hard multilayer TiN-AlTiN/nACo-CrN/AlCrN-AlCrO-AlTiCrN coating deposited on WC-Co substrate. *Coatings*, 10(9), p. 909.

Article

High-Temperature Tribological Performance of Hard Multilayer TiN-AlTiN/nACo-CrN/AlCrN-AlCrO-AlTiCrN Coating Deposited on WC-Co Substrate

Asad Alamgir ^{1,*} , Maxim Yashin ¹, Andrei Bogatov ¹, Mart Viljus ¹, Rainer Traksmaa ¹, Jozef Sondor ², Andreas Lümkemann ³, Fjodor Sergejev ¹ and Vitali Podgursky ¹ 

¹ Department of Mechanical and Industrial Engineering, Tallinn University of Technology, Ehitajate tee 5, 19086 Tallinn, Estonia; mayash@ttu.ee (M.Y.); andrei.bogatov@mail.ru (A.B.); mart.viljus@taltech.ee (M.V.); rainer.traksmaa@taltech.ee (R.T.); fjodor.sergejev@taltech.ee (F.S.); vitali.podgurski@ttu.ee (V.P.)

² LISS a.s., Coating center PLATIT, Dopravní 2603, 756 61 Rožnov pod Radhoštěm, Czech Republic; j.sondor@liss.cz

³ PLATIT AG, Eichholzstrasse 9, CH-2545 Selzach, Switzerland; a.luemkemann@platit.com

* Correspondence: asad.shaikh@taltech.ee; Tel.: +372-58791387

Received: 8 September 2020; Accepted: 18 September 2020; Published: 22 September 2020



Abstract: Mechanical and tribological properties of the hard-multilayer TiN-AlTiN/nACo-CrN/AlCrN-AlCrO-AlTiCrN coating deposited on WC-Co substrate were investigated. The sliding tests were carried out using ball-on-disc tribometer at room (25 °C) and high temperatures (600 and 800 °C) with Al₂O₃ balls as counterpart. Nano-scratch tests were performed at room temperature with a sphero-conical diamond indenter. The surface morphology and chemical composition were investigated with scanning electron microscopy (SEM), energy-dispersive spectrometry (EDS) and in-situ high-temperature X-ray diffraction (HT-XRD). The phase transition from fcc-(Al,Cr)₂O₃ into α -(Al,Cr)₂O₃ was observed at about 800 °C. The results of the tribological tests depends on the temperature, the lowest apparent and real wear volumes were observed on the coating after the test at 800 °C along with the smallest coefficient of friction (COF). The plastic deformation of the coating was confirmed in sliding and nano-scratch tests. The nano-scratch tests revealed the dependence of COF value on the temperature of the sliding tests.

Keywords: multilayer coating; high temperature tribology; nano-scratch

1. Introduction

To achieve industrial demands, several advanced coating structures such as multi-component [1,2], nanocomposite [3], gradient [4,5] and multilayer structures [6,7] have been developed. Multilayer structure combines the advantages of component sublayers. The substitutional defects may form at the interface of adjacent layers in multilayered coatings, which results in the generation of strain energy preventing the movement of dislocations [8]. The stress concentrations act as crack inhibitors and thus improve the fracture resistance [9]. Therefore, multilayer structure is one of the widely used and convenient approach for practical applications of coating [10–12].

The nitride-based coatings are characterized by high hardness, high melting temperature, good fracture toughness, chemical and physical stability. The TiN coating has been extensively used to protect cutting tools, due to their superior mechanical properties. However, TiN failed because of coating surface oxidation occurring during the cutting process. The issue of surface oxidation was solved by the addition of Al in TiN, which leads to formation of thin protective alumina layer on the coating surface. The Al atoms substitute Ti atoms in TiN lattice. The lattice distortion leads to the increase of the hardness and thus improve the abrasive wear resistance of TiAlN [13,14]. The (nc-Ti_{1-x}Al_xN)/(α -Si₃N₄)

(nACo) coating is the nanocomposite coating of nanocrystalline nc-AlTiN grains embedded into amorphous α -Si₃N₄ matrix, which results in high hardness and good resistance to abrasive wear. The AlCrN coating was developed based on binary CrN coating [15]. The addition of Al into the CrN coating improves oxidation resistance, chemical stability and mechanical properties [16,17]. The deposition of AlCrO ((Al,Cr)₂O₃) improves the stability of the whole system at elevated temperature and reduces chemical affinity between the tool and workpiece in cutting process. Finally, the AlTiCrN coating was used as an adaptive layer [18,19]. Tribological adaptability plays a significant role in improving the tribological properties of hard coatings. The adaptability of the tribological system can be achieved, for instance, by increasing the chemical complexity of coating [20,21].

The substrate effects significantly on the tribological behavior of the coating, for instance, soft coating on hard substrate and the hard coating on soft substrate exhibit different tribological behaviors [22]. The load-carrying capacity is an ability to withstand pressure in the film/substrate system without the loss of the system functionality [23]. The film deflection phenomenon was investigated in our previous studies where the diamond films were deposited on the Si and single crystal diamond substrates [24–26]. The deflection of diamond film deposited on the Si substrate was observed in sliding tests. It is expected that during the cutting a high load experienced by coating. However, in spite of the importance of load-carrying capacity for the characterization of coated tools, this property remains insufficiently investigated, particularly, for multilayer hard coatings.

In the present study, the mechanical and tribological properties of hard-multilayers TiN-AlTiN/nACo-CrN/AlCrN-AlCrO-AlTiCrN coating were investigated at elevated temperatures under ambient environment conditions.

2. Materials and Methods

The TiN-AlTiN/nACo-CrN/AlCrN-AlCrO-AlTiCrN coating was deposited on polished WC-Co substrates (\varnothing 13 mm, height 5 mm, $R_a = 0.05 \mu\text{m}$) using physical vapor deposition (PVD) rotating cathodes arc Platit[®] π 411 system. The Ti, AlTi (33 at.% Ti), AlCr (45 at.% Cr) and AlSi (18 at.% Si) cathodes were used for the deposition of coating. The TiN-AlTiN/nACo layers were deposited at 550 °C and CrN/AlCrN-AlCrO-AlTiCrN at 570 °C, the total thickness of coating was 3.6 μm . The thickness and hardness of layers are shown in Table 1. The thickness of coating was measured by the calo-test (BAQ[®]) method.

Table 1. Thickness and hardness of the coating layers deposited on WC-Co substrate.

Substrate	Layers	Coating	Thickness (μm)	Nano Hardness (GPa)
WC-Co	1	TiN	0.2	24–26 *
	2	AlTiN/nACo	2.0	36–38 */39–41 *
	3	CrN/AlCrN	0.6	21–23 */36–38 *
	4	(Al,Cr) ₂ O ₃ (fcc and α phases)	0.5	24–25 ** and 28 **
	5	AlTiCrN	0.3	36–38 *

*—the hardness values adopted from Platit [27]. **—the hardness values adopted from Khatabi et al. [28].

The tribological behavior of coating was investigated using a ball-on-disc CERT tribometer (manufacturer Bruker[®] UMT-2, Billerica, MA, USA). The samples were subjected to tests at room (RT) (25 °C) and high temperatures (600 and 800 °C). All tests were performed under ambient conditions using Al₂O₃ (alumina) balls from REDHILL[®] with \varnothing 6 mm as the counterbody, with the normal load of 10 N. The speed of rotation was 300 rpm, the wear track radius was 4 mm, the total sliding distance was 5400 m and the duration of each test was 3 h.

The cross-section area of the wear scars was measured using mechanical profilometer (Mahr Perthometer[®], Göttingen, Germany) at four different positions to calculate the wear volume.

The nano-scratch tests were performed with ultra-low drift nano-mechanical test system (NanoTest, Micro Materials Ltd.[®], Wrexham, UK) with a sphero-conical diamond indenter with a tip radius of 5 μm . All tests were performed as multi-pass experiments (3-scans: topography–scratch–topography) that were subsequently analyzed in the NanoTest software to determine the on-load and residual depth. The total length of scratch tests was 300 μm and load applied for scratch after scanning the distance of 50 μm . The progressive load with loading rate of 5 mN/s was applied up to the reaching of the peak load, the details of the tests are presented in Table 2. The elastic/plastic behavior of coating, wear and coefficient of friction (COF) were the prime interest in nano-scratch tests.

Table 2. Nano-scratch tests parameters.

Peak Load (mN)	Loading Rate, dL/dt (mN/s)	Scan Speed, dx/dt ($\mu\text{m/s}$)	dL/dx (mN/ μm)
5, 10, 15, 20, 50, 75, 100, 150, 200, 250, 300, 400	5	2	2.5

The optical microscope and scanning electron microscope (SEM) were used for investigation of the surface morphology. The SEM images were taken by the (Hitachi[®] TM-1000 system, Tokyo, Japan) and the (Zeiss[®] EVO MA-15 system, Oberkochen, Germany) with LaB6 cathode in secondary electron mode, applying an accelerating voltage of 10–15 kV and 6.5–5.8 mm working distance. The chemical composition of the coating was investigated by energy dispersion X-ray spectroscopy (EDS) and high-temperature in-situ X-ray diffraction (HT-XRD) using a (Rigaku[®] Cu $K\alpha$ radiation, Tokyo, Japan) with the heating rate of 20 $^{\circ}\text{C}/\text{min}$ and the temperature range between RT and 1200 $^{\circ}\text{C}$.

3. Results and Discussion

Figure 1a shows the SEM image of pristine surface, spherical and shapeless microdroplets and surface cavities can be observed. The HT-XRD patterns collected between RT and 1200 $^{\circ}\text{C}$ with an interval of 100 $^{\circ}\text{C}$ are shown in Figure 1b. There is no significant difference between the patterns corresponding to as-deposited and annealed up to 700 $^{\circ}\text{C}$ coating, the XRD peaks correspond to the fcc-(Al_{1-x}Cr_x)_{2+ δ} (fcc-(Al,Cr)₂O₃) [29], WC-Co [30] and cubic AlTiCrN (c-AlTiCrN) coating [28]. The formation of fcc-(Al,Cr)₂O₃ grown on top of c-AlTiCrN layer is in agreement with the study of Najafi H. et al. [29], namely, the XRD peak at 43.5 $^{\circ}$ was found after the preparation of fcc-(Al,Cr)₂O₃ at 550 $^{\circ}\text{C}$ on the cubic CrN layer. The growth and mechanical properties of the fcc-(Al,Cr)₂O₃ oxide deposited by magnetron sputtering was investigated by Khatibi A. et al. [28], the nano hardness was 24–25 GPa. The XRD peaks corresponding to the α -(Al,Cr)₂O₃ phase can be observed under heating from 800 to 1200 $^{\circ}\text{C}$ (Figure 1b). The presence of α -(Al,Cr)₂O₃ indicates phase transition from fcc to α phase at 800 $^{\circ}\text{C}$. The relative intensity of the peak at 43.5 $^{\circ}$ decreases steadily at the higher temperatures and an increase of the intensity of the peaks corresponding to the α phase can be seen.

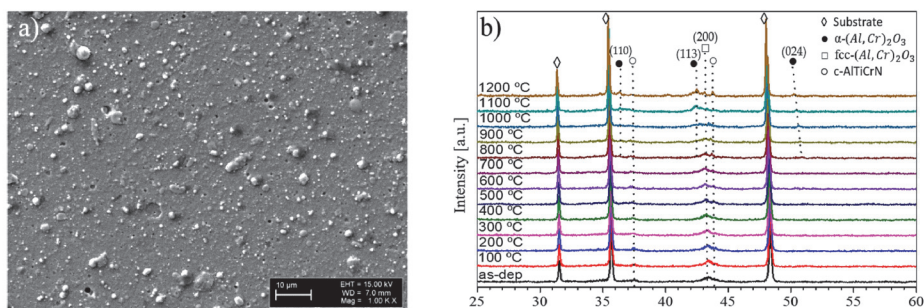


Figure 1. SEM image taken on pristine coating surface (a) and (b) HT-XRD patterns.

Figure 2 shows the COF versus cycles curves recorded during the sliding tests at RT, 600, and 800 °C. The steady-state regime without significant run-in-period was found from the beginning of the test at RT. The initial and final COF values are approximately equal to 0.7. The run-in-periods of 10,000 and 15,000 cycles were found for the tests at 600 and 800 °C, respectively. The COF value of 0.9 was highest during the running-in period in the test at 600 °C. Finally, at the end of the test at 600 °C, the COF value is similar to the one observed at RT. At the highest temperature 800 °C, the COF value fluctuation during the running-in period follows by the continuous decrease with final stabilization about 0.45. The difference in COF values at the end of the tests (RT and 600 °C in opposite to 800 °C) is due to contact between fcc-(Al,Cr)₂O₃ and ball (RT and 600 °C) and α-(Al,Cr)₂O₃ and ball (800 °C). The COF behavior observed in the present study shows a good correlation with the results of Santeccchia et al. [31] found in the sliding tests at room and high temperatures. The noise and peaks can be observed in Figure 2. In the case of test at RT, the noisy period lasts for about 20,000 cycles and in the tests at 600 and 800 °C for 8000 and 15,000 cycles, respectively. The noise and peaks can indicate a seizure at the beginning of the sliding tests in analogy with the results of our previous study on the diamond films deposited on Si wafer [26]. The variations in COF value were observed for all tests in the range of 17,000–37,000 cycles, indicating probably that the AlTiCrN layer was worn out and the contact between alumina layer and ball was formed in the course of the tests.

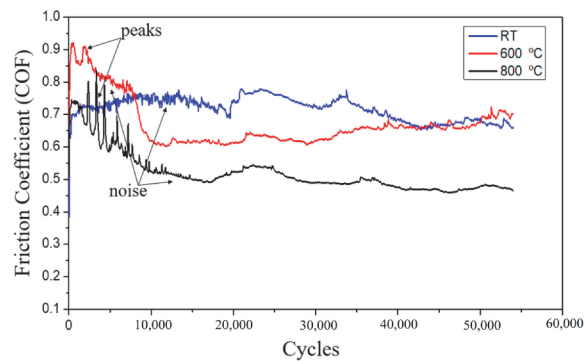


Figure 2. COF versus cycles curves taken at RT, 600 and 800 °C.

Figures 3 and 4 show the wear scar depth profiles on the coating and the SEM images taken on the wear scars of coating and balls surface after the tests at RT, 600 and 800 °C. After the test at RT, a relatively smooth wear scar profile can be found in Figure 3a. The wear scar depth is about 0.7 μm, which indicates that at the end of the test a contact was between the ball and (Al,Cr)₂O₃ layer, i.e., the second layer ((Al,Cr)₂O₃) was partially worn out. Several discontinues grooves were observed on the wear scar surface, see Figure 3b. The width of the wear scar was largest after the test at 600 °C, as well as the presence of grooves within the wear scar was observed (Figure 3e). The roughness of the wear scars surface was highest after the test at 800 °C (Figure 3g,h). The higher roughness of the wear scar after the test at 800 °C indicates significant changes in wear mechanisms as compared with the tests at RT and 600 °C.

Two different areas within the wear scars can be distinguished, which are denoted by I and II Figure 3. The area I is located in the central part and the area II at the border of the wear scar. The area II is shown in more detail in Figure 4. Within this area, the severe wear of the coating was not initiated and only a ball surface plowing was occurred. The analysis suggests that probably ploughing of the outer part of the alumina ball takes place on the hard particles produced during the deposition of the AlTiCrN coating Figure 1a. The comparison of the shape of line scans in (Figure 3a,d,g) with corresponding SEM images in (Figure 3b,e,h) suggest that the plastic deformation of coating occurs in the course of the sliding tests. In spite of the brittle nature of the hard coating, due to probably

relatively small thickness and large area of the coating, the coating can be plastically deformed without cracks formation.

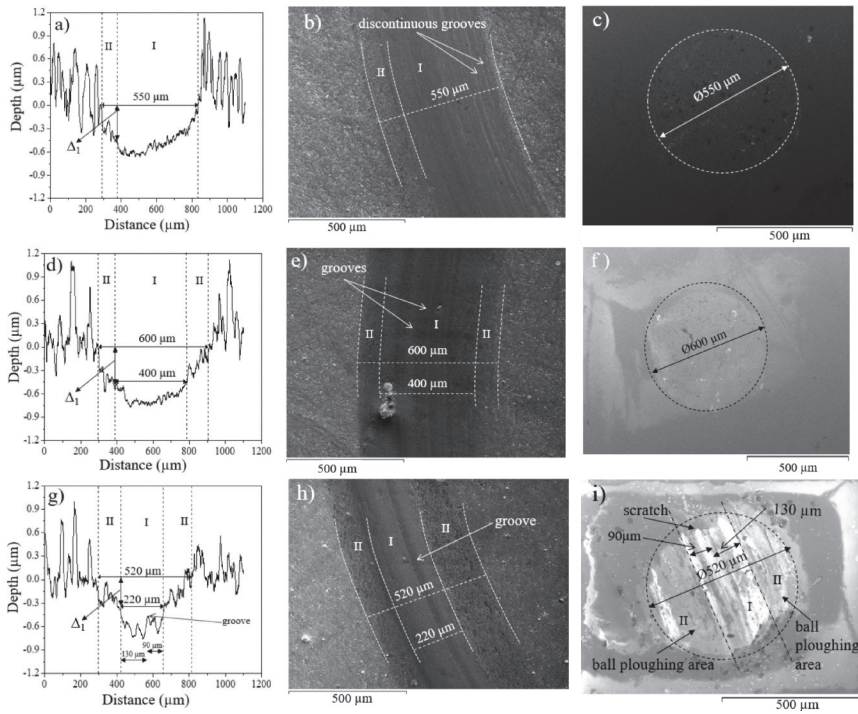


Figure 3. Wear scar depth profiles on the coating and alumina balls after sliding tests: (a–c) RT, (d–f) 600 and (g–i) 800 °C.

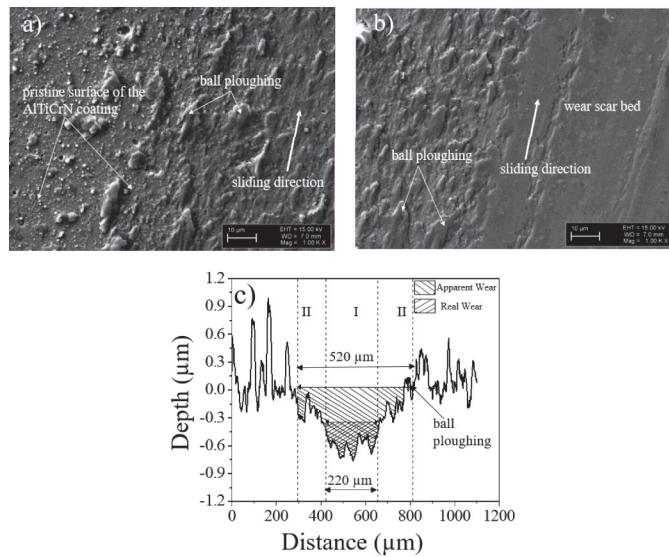


Figure 4. SEM images of the sample tested at 800 °C: (a) pristine surface and region II, (b) regions II and I (see Figure 3g,h) and (c) apparent and real wear volumes.

The deformation of the coating was taken into account for the calculation of the wear volume, see Figures 4c and 5. The apparent wear volume should be distinguished from the real one. The apparent wear volume is a sum of the real wear volume and the volume corresponding to the deformation of the coating as shown in Figure 4c. The apparent wear volume was highest after the tests at RT and 600 °C, as well as these wear volumes for both tests are very similar. The smallest apparent wear volume was observed after the test at 800 °C. The real wear volume was smallest for the same test as well. The real wear volume after the test at RT was unable to estimate correctly, therefore it is not shown in Figure 5.

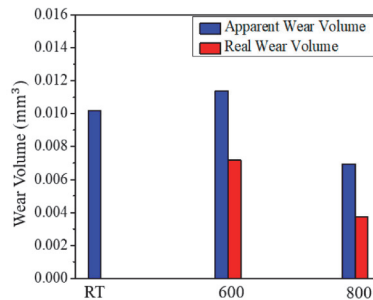


Figure 5. Apparent and real wear volumes after the sliding tests at RT, 600 and 800 °C.

Figure 6 shows the EDS data taken on the pristine surface of the coating and within the wear scars after the tests at RT, 600 and 800 °C. The content of oxygen increases, and vice versa the content of nitrogen (presented in AlTiCrN layer) decreases with respect to temperature (Figure 6a). The formation of protective alumina layer can be related with this observation. The EDS data taken within the wear scars on coating shows a presence of a remarkably higher concentration of oxygen, as compared with pristine surface, and the concentration of nitrogen is negligible (Figure 6b). The EDS data allows to conclude that at the end of the tribological tests, the ball was in contact with $(Al,Cr)_2O_3$ layer (Table 1). This conclusion is in good agreement with the deepest valley in line scans in Figure 3, where the depth varied between 0.7–0.75 μm independent of the temperature of the test.

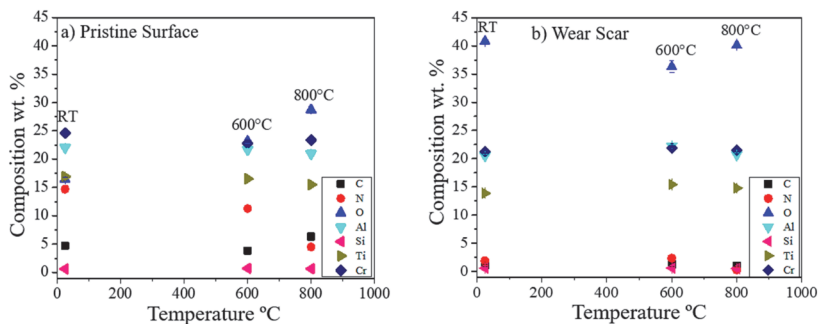


Figure 6. EDS data taken on (a) the coating pristine surface and (b) wear scars surface after the tests at different temperatures.

The nano-scratch tests were performed on the pristine surface of coating after sliding tests at different temperatures. Figure 7 shows the results of the scratch test taken on the coating after the sliding test at 800 °C and the optical micrograph of scratch track. The elastic and plastic deformation and wear of the coating surface can be observed without visible cracks formation. The result shows that the total coating surface deviation during the scratch scan ($\Delta_3 = 0.82\text{--}1.14 \mu\text{m}$ in Table 3) is relatively high in comparison with the thickness of coating, i.e., 3.6 μm . The deviation due to plastic deformation

and the wear (Δ_2) is the distance between the line scans corresponding to the 1st and 2nd topography scans (Figure 7), i.e., 0.25–0.49 μm (Table 3). The wear is relatively small, thus Δ_2 corresponds mostly to the plastic deformation of the coating, see scratch track in Figure 7. The Δ_1 values shown in Figure 3 correspond to the bending of the area II, i.e., the area where only the ball ploughing was observed. The Δ_1 and Δ_2 values are quite similar due to likely plastic deformation of the coating in both types of tests, i.e., in sliding and nano-scratch tests (Table 3).

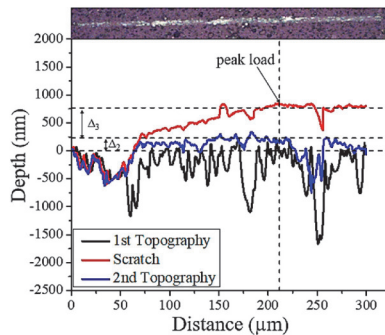


Figure 7. Nano-scratch test with scratch track at 400 mN of the peak load taken on the pristine surface of the sample tested at 800 °C in sliding test.

Table 3. Δ_1 , Δ_2 and Δ_3 values obtained after sliding and nano-scratch tests.

Samples	Δ_1 (nm)	Δ_2 (nm)	Δ_3 (nm)
RT	480	480	1010
600 °C	450	490	1140
800 °C	350	250	820

Figure 8 shows the COF value between the coating and the diamond indenter measured for different loads. The COF values (0.12–0.15) observed after the tests at high temperatures correlate with the results of our previous study performed on alumina thin films using the nano-scratch technique with diamond indenter [32]. The low-load (up to the 100 mN) friction behavior is similar independent of the temperature of the sliding tests. It could be probably due to fact that the surface of the coating is relatively rough (Figures 1 and 7) and under the lower loads the COF depends mostly on the surface roughness. In fact, the topography scans are made using small load (0.1 mN). At the higher load there is a difference between the samples tested at RT and at 600 and 800 °C. The difference between COF values can be due to formation of thicker alumina layer on top of the samples tested at 600 and 800 °C, as well as under higher load the stronger adhesion between the diamond indenter and coating surface takes place. This oxide layer can be partially scratched out during the scratch scan. The EDS results confirm that oxide layer is formed on top of AlTiCrN layer at high temperature (Figure 6a).

The mechanical and tribological properties of the coating tested at high temperatures differs from the ones at RT. Formation of the thin oxide layer on the top of the AlTiCrN coating leads to the decrease of COF value between the ball and oxidized AlTiCrN surface in high temperature sliding tests (Figure 2). On the other hand, COF value increases between diamond indenter and oxidized AlTiCrN surface in nano-scratch tests at room temperature (Figure 8). In the sliding tests, the AlTiCrN layer was continuously worn out with following formation of the contact between the alumina ball and (Al,Cr)₂O₃ layer (Table 1) in the later stages of sliding. These tests show also the difference between the wear mechanisms of the (Al,Cr)₂O₃ layer against alumina ball. The transformation from fcc-(Al,Cr)₂O₃ to α -(Al,Cr)₂O₃ phase takes place at 800 °C. The highest coating deflection was observed on the samples tested at RT and 600 °C, i.e., when there is no phase transformation from fcc to α phase. In the case

of RT and 600 °C, the relatively smooth wear scars surface on the coating and the ball were found, however after the test at 800 °C the surface was rougher (Figure 3). It indicates the change in wear mechanisms at 800 °C, due to probably increase in the hardness of α -(Al,Cr)₂O₃ and decreasing of the deflection of the whole coating system. The Al₂O₃ ball ploughing on the hard AlTiCrN surface peculiarities was found which can result in the noise and peaks in the COF value in sliding tests (Figure 2). In addition, relatively high deformation of the coating was found during the sliding and nano-scratch tests, therefore it suggests that the surface deformation in tribological tests can result in seizure particularly at the early stages of the sliding. Similar phenomena like deflection of the coating, noise and peaks in the COF value and seizure were observed on the diamond films prepared on Si and tested in the sliding tests [26]. Therefore, the effect of deformation of the coating due to high contact pressure between the coating and counterbody can play important role in wear processes.

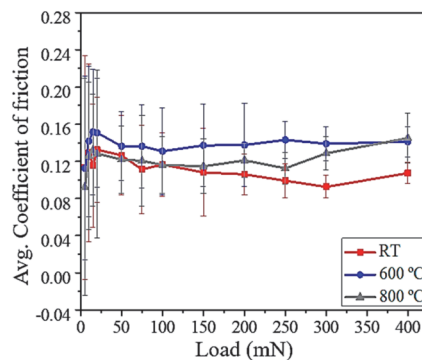


Figure 8. Coefficient of friction (COF) versus load measured in nano-scratch tests.

4. Conclusions

The mechanical and tribological properties of TiN-AlTiN/nACo-CrN/AlCrN-AlCrO-AlTiCrN coating were evaluated at RT and high temperatures (600 and 800 °C). The increase of wear resistance for coating tested at 800 °C was found due to the formation of the protective oxide layer on top of AlTiCrN and phase transformation within the (Al,Cr)₂O₃ layer leading in increase of hardness of this oxide layer and decrease of deflection of the whole coating system. The relatively higher deflection was observed on the samples tested at RT and 600 °C.

The COF value measured in nano-scratch tests between the AlTiCrN layer and diamond indenter is different for the samples heated at different temperatures. Due to formation of the thin oxide layer on the AlTiCrN layer, the COF value is higher for the samples heated at higher temperatures as compare with the sample tested at RT. The coating surface deflection during the scratch test can be significant, i.e., about the 1/3 of the coating thickness at the peak load of 400 mN.

In conclusion, due to high contact pressure between the coating and counterbody, the deformation of coating plays important role in wear processes.

Author Contributions: Conceptualization, V.P.; methodology, V.P.; validation, M.Y. and A.B.; formal analysis, A.A. and V.P.; investigation, A.A., M.Y., M.V., and R.T.; resources, V.P.; data curation, A.A.; writing—original draft preparation, A.A.; writing—review and editing, A.A., J.S., A.L., F.S., and V.P.; visualization, A.A.; supervision, V.P.; project administration, V.P.; funding acquisition, V.P. All authors have read and agreed to the published version of the manuscript.

Funding: This study was financially supported by the Estonian Ministry of Education and Research under target financing project PUT1369 (Adaptation mechanisms of diamond films in dry sliding wear).

Conflicts of Interest: The authors declare no conflict of interest.

References

1. Malinovskis, P.; Fritze, S.; Riekehr, L.; von Fieandt, L.; Cedervall, J.; Rehnlund, D.; Nyholm, L.; Lewin, E.; Jansson, U. Synthesis and characterization of multicomponent (CrNbTaTiW)C films for increased hardness and corrosion resistance. *Mater. Des.* **2018**, *149*, 51–62. [[CrossRef](#)]
2. Johansson, K.; Riekehr, L.; Fritze, S.; Lewin, E. Multicomponent Hf-Nb-Ti-V-Zr nitride coatings by reactive magnetron sputter deposition. *Surf. Coat. Technol.* **2018**, *349*, 529–539. [[CrossRef](#)]
3. Bobzin, K.; Brögelmann, T.; Kruppe, N.C.; Carlet, M. Nanocomposite (Ti,Al,Cr,Si)N HPPMS coatings for high performance cutting tools. *Surf. Coat. Technol.* **2019**, *378*, 124857. [[CrossRef](#)]
4. Tong, M.; Fu, Q.; Zhou, L.; Feng, T.; Li, H.; Li, T.; Li, K. Ablation behavior of a novel HfC-SiC gradient coating fabricated by a facile one-step chemical vapor co-deposition. *J. Eur. Ceram. Soc.* **2018**, *38*, 4346–4355. [[CrossRef](#)]
5. Wang, Y.; Su, D.; Ji, H.; Li, X.; Zhao, Z.; Tang, H. Gradient structure high emissivity MoSi₂-SiO₂-SiOC coating for thermal protective application. *J. Alloys Compd.* **2017**, *703*, 437–447. [[CrossRef](#)]
6. Zhang, D.; Qi, Z.; Wei, B.; Shen, H.; Wang, Z. Microstructure and corrosion behaviors of conductive Hf/HfN multilayer coatings on magnesium alloys. *Ceram. Int.* **2018**, *44*, 9958–9966. [[CrossRef](#)]
7. Wang, T.; Jin, Y.; Bai, L.; Zhang, G. Structure and properties of NbN/MoN nano-multilayer coatings deposited by magnetron sputtering. *J. Alloys Compd.* **2017**, *729*, 942–948. [[CrossRef](#)]
8. Pogrebnyak, A.D.; Beresnev, V.M.; Bondar, O.V.; Postolnyi, B.O.; Zaleski, K.; Coy, E.; Jurga, S.; Lisovenko, M.O.; Konarski, P.; Rebouta, L.; et al. Superhard CrN/MoN coatings with multilayer architecture. *Mater. Des.* **2018**, *153*, 47–59. [[CrossRef](#)]
9. Veprek, S. Recent search for new superhard materials: Go nano! *J. Vac. Sci. Technol. A Vac. Surf. Film.* **2013**, *31*, 050822. [[CrossRef](#)]
10. Luo, Q.; Wang, S.C.; Zhou, Z.; Chen, L. Structure characterization and tribological study of magnetron sputtered nanocomposite nc-TiAlV(N,C)/a-C coatings. *J. Mater. Chem.* **2011**, *21*, 9746–9756. [[CrossRef](#)]
11. Ma, G.; Lin, G.; Gong, S.; Liu, X.; Sun, G.; Wu, H. Mechanical and corrosive characteristics of Ta/TaN multilayer coatings. *Vacuum* **2013**, *89*, 244–248. [[CrossRef](#)]
12. Morant, C.; Garcia-Manyes, S.; Sanz, F.; Sanz, J.M.; Elizalde, E. Nanotribological properties of CN/TiCN/TiN/Si multilayer as determined by AFM. *Nanotechnology* **2005**, *16*. [[CrossRef](#)]
13. Arndt, M.; Kacsich, T. Performance of new AlTiN coatings in dry and high speed cutting. *Surf. Coat. Technol.* **2003**, *163*, 674–680. [[CrossRef](#)]
14. Chang, Y.Y.; Chang, C.P.; Kao, H.Y. High temperature oxidation resistance of multilayered Al₃Ti_{1-x}N/CrN coatings. *Thin Solid Films* **2011**, *519*, 6716–6720. [[CrossRef](#)]
15. Zhou, H.; Zheng, J.; Gui, B.; Geng, D.; Wang, Q. AlTiCrN coatings deposited by hybrid HIPIMS/DC magnetron co-sputtering. *Vacuum* **2017**, *136*, 129–136. [[CrossRef](#)]
16. Hsieh, J.H.; Tan, A.L.K.; Zeng, X.T. Oxidation and wear behaviors of Ti-based thin films. *Surf. Coat. Technol.* **2006**, *201*, 4094–4098. [[CrossRef](#)]
17. Höling, A.; Hultman, L.; Odén, M.; Sjölen, J.; Karlsson, L. Mechanical properties and machining performance of Ti_{1-x}Al_xN-coated cutting tools. *Surf. Coat. Technol.* **2005**, *191*, 384–392. [[CrossRef](#)]
18. Fox-Rabinovich, G.S.; Yamamoto, K.; Veldhuis, S.C.; Kovalev, A.I.; Dosbaeva, G.K. Tribological adaptability of TiAlCrN PVD coatings under high performance dry machining conditions. *Surf. Coat. Technol.* **2005**, *200*, 1804–1813. [[CrossRef](#)]
19. PalDey, S.; Deevi, S.C. Single layer and multilayer wear resistant coatings of (Ti,Al)N: A review. *Mater. Sci. Eng. A* **2003**, *342*, 58–79. [[CrossRef](#)]
20. Fox-Rabinovich, G.S.; Yamamoto, K.; Veldhuis, S.C.; Kovalev, A.I.; Shuster, L.S.; Ning, L. Self-adaptive wear behavior of nano-multilayered TiAlCrN/WN coatings under severe machining conditions. *Surf. Coat. Technol.* **2006**, *201*, 1852–1860. [[CrossRef](#)]
21. Gershman, I.; Gershman, E.I.; Mironov, A.E.; Fox-Rabinovich, G.S.; Veldhuis, S.C. Application of the self-organization phenomenon in the development of wear resistant materials—A review. *Entropy* **2016**, *18*, 385. [[CrossRef](#)]
22. Holmberg, K.; Ronkainen, H.; Laukkanen, A.; Wallin, K. Friction and wear of coated surfaces-scales, modelling and simulation of tribomechanisms. *Surf. Coat. Technol.* **2007**, *202*, 1034–1049. [[CrossRef](#)]

23. Bell, T.; Dong, H.; Sun, Y. Realising the potential of duplex surface engineering. *Tribol. Int.* **1998**, *31*, 127–137. [[CrossRef](#)]
24. Podgursky, V.; Bogatov, A.; Sobolev, S.; Viljus, M.; Sedov, V.; Ashkinazi, E.; Ralchenko, V. Effect of nanocrystalline diamond films deflection on wear observed in reciprocating sliding tests. *J. Coat. Sci. Technol.* **2016**, *3*, 109–115. [[CrossRef](#)]
25. Podgursky, V.; Bogatov, A.; Yashin, M.; Viljus, M.; Bolshakov, A.P.; Sedov, V.; Volobujeva, O.; Mere, A.; Raadik, T.; Ralchenko, V. A comparative study of the growth dynamics and tribological properties of nanocrystalline diamond films deposited on the (110) single crystal diamond and Si(100) substrates. *Diam. Relat. Mater.* **2019**, *92*, 159–167. [[CrossRef](#)]
26. Podgursky, V.; Bogatov, A.; Yashin, M.; Sobolev, S.; Gershman, I.S. Relation between self-organization and wear mechanisms of diamond films. *Entropy* **2018**, *20*, 279. [[CrossRef](#)]
27. Platit. Portfolio. Available online: https://www.platit.com/media/filer/2020/short_catalog-en.pdf (accessed on 1 January 2020).
28. Khatibi, A.; Palisaitis, J.; Höglund, C.; Eriksson, A.; Persson, P.O.; Jensen, J.; Birch, J.; Eklund, P.; Hultman, L. Face-centered cubic $(Al_{1-x}Cr_x)_2O_3$. *Thin Solid Films* **2011**, *519*, 2426–2429. [[CrossRef](#)]
29. Najafi, H.; Karimi, A.; Dessarzin, P.; Morstein, M. Formation of cubic structured $(Al_{1-x}Cr_x)_{2+8}O_3$ and its dynamic transition to corundum phase during cathodic arc evaporation. *Surf. Coat. Technol.* **2013**, *214*, 46–52. [[CrossRef](#)]
30. Forsén, R.; Johansson, M.P.; Odén, M.; Ghafoor, N. Effects of Ti alloying of AlCrN coatings on thermal stability and oxidation resistance. *Thin Solid Films* **2013**, *534*, 394–402. [[CrossRef](#)]
31. Santecchia, E.; Cabibbo, M.; Hamouda, A.; Musharavati, F.; Popelka, A.; Spigarelli, S. Investigation of the temperature-related wear performance of hard nanostructured coatings deposited on a S600 high speed steel. *Metals* **2019**, *9*, 332. [[CrossRef](#)]
32. Alamgir, A.; Bogatov, A.; Yashin, M.; Podgursky, V. Mechanical and tribological properties of 100-nm thick alumina films prepared by atomic layer deposition on Si(100) substrates. *Proc. Est. Acad. Sci.* **2019**, *68*, 125–129. [[CrossRef](#)]






© 2020 by the authors. Licensee MDPI, Basel, Switzerland. This article is an open access article distributed under the terms and conditions of the Creative Commons Attribution (CC BY) license (<http://creativecommons.org/licenses/by/4.0/>).

Publication IV

Podgursky, V., **Alamgir, A.**, Yashin, M., Jõgiaas, T., Viljus, M., Raadik, T., Danilson, M., Sergejev, F., Lümekemann, A., Kluson, J. and Sondor, J., 2021. High-Temperature Tribological Performance of Al₂O₃/aC: H: Si Coating in Ambient Air. *Coatings*, 11(5), p. 495.

Article

High-Temperature Tribological Performance of Al₂O₃/a-C:H:Si Coating in Ambient Air

Vitali Podgursky ¹, Asad Alamgir ^{1,*}, Maxim Yashin ¹, Taivo Jõgiaas ², Mart Viljus ¹, Taavi Raadik ³, Mati Danilson ³, Fjodor Sergejev ¹, Andreas Lümekemann ⁴, Jan Kluson ⁵, Jozef Sondor ⁶ and Andrei Bogatov ¹

¹ Department of Mechanical and Industrial Engineering, Tallinn University of Technology, Ehitajate tee 5, 19086 Tallinn, Estonia; vitali.podgurski@taltech.ee (V.P.); maximyash92@gmail.com (M.Y.); mart.viljus@taltech.ee (M.V.); fjodor.sergejev@taltech.ee (F.S.); andrei.bogatov@mail.ru (A.B.)

² Institute of Physic, University of Tartu, W. Ostwaldi 1, 50411 Tartu, Estonia; taivo.jogiaas@ut.ee

³ Department of Materials and Environmental Technology, Tallinn University of Technology, Ehitajate tee 5, 19086 Tallinn, Estonia; taavi.raadik@taltech.ee (T.R.); mati.danilson@taltech.ee (M.D.)

⁴ PLATIT AG, Eichholzstrasse 9, 2545 Selzach, Switzerland; a.luemkemann@platit.com

⁵ PLATIT a.s., Prumyslova 3020/3, 787 01 Sumperk, Czech Republic; j.kluson@platit.com

⁶ LISS a.s., Coating Center PLATIT, Dopravní 2603, 756 61 Rožnov pod Radhoštěm, Czech Republic; j.sondor@liss.cz

* Correspondence: asad.shaikh@taltech.ee

Abstract: The study investigates thermal stability and high temperature tribological performance of a-C:H:Si diamond-like carbon (DLC) coating. A thin alumina layer was deposited on top of the a-C:H:Si coating to improve the tribological performance at high temperatures. The a-C:H:Si coating and alumina layer were prepared using plasma-activated chemical vapour deposition and atomic layer deposition, respectively. Raman and X-ray photoelectron spectroscopy were used to investigate the structures and chemical compositions of the specimens. The D and G Raman peaks due to sp² bonding and the peaks corresponding to the trans-polyacetylene (t-Pa) and sp bonded chains were identified in the Raman spectra of the a-C:H:Si coating. Ball-on-disc sliding tests were carried out at room temperature and 400 °C using Si₃N₄ balls as counter bodies. The a-C:H:Si coating failed catastrophically in sliding tests at 400 °C; however, a repeatable and reproducible regime of sliding with a low coefficient of friction was observed for the Al₂O₃/a-C:H:Si coating at the same temperature. The presence of the alumina layer and high stress and temperature caused structural changes in the bulk a-C:H:Si and top layers located near the contact area, leading to the modification of the contact conditions, delivering of extra oxygen into the contact area, reduction of hydrogen effusion, and suppression of the atmospheric oxidation.

Keywords: diamond-like carbon; alumina; thermal stability; adaptation; tribology; wear



check for updates

Citation: Podgursky, V.; Alamgir, A.; Yashin, M.; Jõgiaas, T.; Viljus, M.; Raadik, T.; Danilson, M.; Sergejev, F.; Lümekemann, A.; Kluson, J.; et al. High-Temperature Tribological Performance of Al₂O₃/a-C:H:Si Coating in Ambient Air. *Coatings* **2021**, *11*, 495. <https://doi.org/10.3390/coatings11050495>

Academic Editor: Kevin Plucknett

Received: 1 April 2021

Accepted: 21 April 2021

Published: 23 April 2021

Publisher's Note: MDPI stays neutral with regard to jurisdictional claims in published maps and institutional affiliations.



Copyright: © 2021 by the authors. Licensee MDPI, Basel, Switzerland. This article is an open access article distributed under the terms and conditions of the Creative Commons Attribution (CC BY) license (<https://creativecommons.org/licenses/by/4.0/>).

1. Introduction

The minimisation of heat generation, friction, and wear demand in industry is an essential issue for sustainable development [1]. Carbon-based coatings have wide industrial applications (aerospace, automotive, machine tools, medical implants, etc. [1,2]) owing to their low coefficient of friction (COF) for different types of friction pairs, good mechanical properties, and chemical inertness. The challenge is that these properties should be retained during intensive use of such coatings under aggressive conditions (temperature, atmosphere, irradiation, etc.).

The tribological performance of carbon-based coatings is sensitive to their properties (hardness, internal stress, adhesion, thermal stability, oxidation resistance, surface roughness, etc.) and test conditions (sliding regimes, atmosphere, temperature, etc.). In addition to the preparation of carbon-based coatings using different deposition techniques, there are some straightforward approaches to modifying the structure of the coatings. First, the surface and bulk properties can be changed by doping, annealing, and irradiation.

Second, modification of the surface properties of the coating can be accomplished by using different lubricants and ambient environments, post-treatment of the surface by plasma, deposition of thin adaptive layers, etc. Third, the properties of the coating can be changed in situ in tribological tests owing to mechanochemical processes. The frictional heat dissipated within the coating and high stress within the contact area can cause changes in the coating structure.

The main components of the structure of diamond-like carbon (DLC) and tetrahedral amorphous carbon (ta-C) are the networks of sp^2 and sp^3 bonds and impurities (H, O, N, Si, Ti, W, etc.). Inclusions of sp -hybridised trans-polyacetylene (t-Pa) and poly(p-phenylene vinylene) chains were revealed in an a-C:H coating by resonant Raman scattering [3]. Longer and shorter t-Pa chains were found in DLC [4], and the formation of two types of sp -hybridised chains (cumulene and polyyne) were reported by Ravagnan et al. [5].

The sp^2 and sp^3 bonds play a key role in the unique mechanical and tribological properties of DLC and ta-C coatings. The crucial parameters are the sp^3 content, clustering and orientation of the sp^2 phase, cross-sectional nanostructures, and hydrogen content [6]. High internal stress occurs in DLC coatings because of the large fraction of highly tensile-strained sp^3 C–C bonds [7]. It is accepted that the sp^3 bond network affects the thermal stability and mechanical properties (hardness, Young's modulus) of DLC and ta-C coatings [6,8,9]. The configuration of the order/disorder within the sp^2 phase can also influence the mechanical properties [10]. At a relatively low temperature (200–300 °C), the graphitisation or transformation of sp^3 to sp^2 bonds occurs in DLC coatings [11–13]. Stress-induced graphitisation can also occur because of the high contact pressure in sliding tests [9]. High hardness, surface smoothness, and viscoelasticity/viscoplasticity are properties that strongly influence the tribological behaviour of DLC coatings [14–17]. The passivation of dangling bonds by different agents (H, hydroxyl (–OH), carboxyl (–COOH), etc.), graphitisation, and the formation of a self-generated easy-shearing transfer layer consisting of carbon-based structures, oxides, water, etc., are the main mechanisms explaining the excellent tribological properties of DLC and ta-C coatings, including superlubricity (COF < 0.01 [18]) [14,19–23]. Hydrogen and oxygen thus play important roles in understanding the friction mechanisms of DLC and ta-C coatings.

There is increasing interest in improving the thermal stability, oxidation resistance, and tribological properties of carbon-based materials under harsh conditions. One of the most successful approaches is doping the a-C:H coating with Si. Low internal stress, good adhesion [24], and enhanced thermal stability have been observed for a-C:H:Si coatings [25,26], and a high load-bearing capacity was demonstrated for a Si-doped DLC coating at room temperature (RT) [27]. The high temperature tribological properties of DLC and Si-doped DLC depends on numbers of factors, for instance, applied load, sliding distance, wear scar radius, counterbody material, etc. [24–26]. A significant fraction of C–Si bonds forms within the a-C:H matrix, which inhibits the formation of strained C–C bonds. This reduces the probability of sp^3 to sp^2 transformation, resulting in higher thermal stability [7]. Further improvements in the thermal stability and tribological properties have been achieved by doping a-C:H with both silicon and oxygen to form an a-C:H:Si:O structure [28–30]. It was reported in a seminal publication [29] that under low Earth orbit conditions, a-C:H:Si:O was more stable than an a-C:H coating. It was stressed that good tribological properties, thermal stability, and suppression of oxidation are caused by the formation of a SiO_2 layer on top of a-C:H:Si and a-C:H:Si:O, in contrast to the a-C:H coating. Oxygen preferentially bonds to silicon in the a-C:H:Si:O coating, forming small local amorphous clusters of a-Si:O [7]. An increase in the hardness and residual stress was observed for an oxygen-doped Si-free a-C:H:O coating, in contrast to the a-C:H coating [31].

Annealing and surface treatment with oxygen-containing gases are used to modify the properties of DLC, ta-C, diamond coatings, etc. Annealing leads to the effusion of hydrogen from a-C:H at 200–300 °C, graphitisation, and the release of internal stress [11,12,32]. Annealing of a Si-doped DLC coating in air causes the formation of a SiO_2 layer on top of the DLC, which results in good tribological properties at room and high temperatures [26,33].

High-energy oxygen plasma treatment such as reactive ion etching (RIE) can be used to etch the surface and modify the surface roughness [34,35]. Oxygen plasma etching of carbon-based coatings enhances the scratch resistance owing to sp^3 bond formation [36]. Improvements in the running-in properties and enhanced surface energy were found on low-energy oxygen plasma-treated ta-C specimens as compared with those treated with high-energy plasma [34]. This difference was explained by the interplay between the chemical reactions and physical collisions during irradiation. A reduced COF value was observed after the oxygen plasma treatment of a Si-doped DLC coating [37]. Improved tribological performance was also observed after the oxygen plasma treatment of a Si-free DLC coating [38]. Oxygen functional groups, including hydroxyl, were found on DLC coatings [38,39], and enhanced surface energy and hydrophilicity were reported after oxygen plasma treatment of DLC coatings [39].

The influence of nitrogen impurities on the structure and properties of DLC and ta-C coatings can be expected during annealing in ambient air and in sliding tests at high temperatures. The increase in the sp^2 bond content, release of the stress, and improvement in the adhesion to Si and CoCrMo alloys were revealed for nitrogen-doped DLC coatings [40,41].

The search strategy for systems exhibiting reduced friction and wear can involve investigating adaptive systems. These systems can self-organise (SO) under specific conditions [42,43]. Soft alloys such as babbitt alloys on relatively hard substrates can significantly increase the contact area, thus decreasing the contact pressure and wear rate at the initial stage of running-in. The initial period determines the tribological behaviour during the subsequent stages of sliding (hereditary effect). Thin oxide layers can have lower hardness (approximately 8.8 GPa for SiO_2 [44] and 10 GPa for amorphous Al_2O_3 [45]) than the DLC, ta-C, and diamond coatings; thus, they can be considered adaptive layers. For instance, it was found that the hardness of a Si-doped DLC coating after oxygen plasma treatment decreased owing to the formation of silicon oxide on top of the coating [37]. In conclusion, a thin silicon oxide film formed on top of a Si-doped DLC coating can be considered an adaptive layer with good lubricating properties that suppresses the atmospheric oxidation of the DLC coating. It should be stressed that different types of silicon oxide (Si_2O , SiO , Si_2O_3 , SiO_2) can be formed on Si-doped DLC coatings [46], and the role of each type of oxide should be specified in detail to explain these functionalities.

Alumina possesses many advantageous properties, including high thermal and chemical resistance and retained hardness at elevated temperatures [47]. A thin Al_2O_3 layer was deposited by atomic layer deposition (ALD) on nanocrystalline diamond (NCD) films, and improved oxidation resistance and thermal stability were demonstrated [48].

In the present preliminary study, a thin Al_2O_3 film (200 nm thick) deposited on top of an a-C:H:Si coating was considered an adaptive multifunctional layer. Improved tribological performance was expected because of modification of the contact conditions during running-in, delivery of extra oxygen into the contact area, reduction of hydrogen effusion, and suppression of the atmospheric oxidation of the a-C:H:Si coating.

2. Materials and Methods

The a-C:H:Si coatings were synthesised by plasma-activated chemical vapour deposition (PACVD) using an arc cathode physical vapour deposition (PVD) unit (Pi411) (PLATIT[®], Grenchen, Switzerland) with a PACVD option containing an MF bias supply (150–350 kHz range) and process gases (C_2H_2 and Si-containing precursor). The coating process started with Ar and metal ion etching, followed by Cr/CrN-based adhesion layer deposition via arc evaporation. The a-C:H:Si coating thickness and Si content in the coating were $1.0 \pm 0.1 \mu m$ and $<5 \text{ at.}\%$, respectively. Typical hardness values of a-C:H:Si were $26.5 \pm 1.5 \text{ GPa}$. The a-C:H:Si coating was deposited on polished WC-Co substrates ($\varnothing 13 \text{ mm}$, height 5 mm, $R_a = 0.05 \mu m$).

ALD was used to prepare Al_2O_3 films. The deposition was conducted in a flow-type reactor (Picosun R200, Espoo, Finland) at $300 \text{ }^\circ C$ using trimethylaluminum (TMA, $Al_2(CH_3)_6$) water as the precursor, and nitrogen as the purge gas. The pressure was

10 mbar (1 kPa). The precursor pulse lengths were 0.1/4/0.1/10 s for TMA/N₂/H₂O/N₂, respectively. After 2000 cycles, the thickness of the Al₂O₃ film was 200 nm. A spectroscopic ellipsometer (SemilabSopraGES-5E, Budapest, Hungary) was used to measure the film thickness, using 365 and 633 nm wavelengths at an angle of 75° on Si(100) reference substrates. Fitting was performed using the Cauchy approximation.

A ball-on-disc tribometer (Bruker® UMT-2, Billerica, MA, USA) equipped with a high-temperature chamber with a rotary drive was used to investigate the tribological behaviour of the specimens. Ø 10 mm Si₃N₄ balls (RedHill®, Prague, Czech Republic) were used as counterbodies. The hardness, Young's modulus, and Poisson ratio of the balls were 1400–1700 HV, 310 GPa, and 0.27, respectively. Wear tests at RT and 400 °C were carried out on the a-C:H:Si and Al₂O₃/a-C:H:Si coatings. The normal load was 2 N, the speed of rotation was 200 rpm, and the wear track diameter was 3 mm. The samples were heated to 400 °C at a heating rate of 5 °C/min, and this temperature was stabilised for 45 min before the sliding test. In total, two sliding tests (for 180 and 5 min, respectively) for each type of specimen were carried out at RT. In the case of the tests at 400 °C, three tests were carried out (two for 180 min and one for 5 min) on the a-C:H:Si specimens and four tests (two for 180 min, one for 60 min, and one for 5 min) for the Al₂O₃/a-C:H:Si specimens. Humidity was 45% ± 5%.

The depth, width, and shape of the wear scars were investigated using stylus profilometry (Mahr Perthometer®, Göttingen, Germany). Five line scans were taken across each wear scar, and an average line scan was obtained. The apparent volume (V) of the wear scar was estimated using the formula $V = S \times l$, where the cross-sectional area is S and the wear scar length is l .

Micro-Raman spectroscopy, X-ray photoelectron spectroscopy (XPS), and scanning electron microscopy (SEM) were used to evaluate the chemical structure and to monitor the morphology of the native and wear scar surfaces. Raman measurements were carried out using a Horiba LabRAM HR800 (Horiba®, Kyoto, Japan) Micro-Raman system equipped with a cooled multichannel CCD detection system in the backscattering configuration with a spectral resolution better than 1 cm⁻¹. A Nd: YAG laser (wavelength $\lambda = 514$ nm) was used for excitation. The spot size was around 5 microns in diameter and spectra accumulation time was 60 s. The composition was studied using XPS in a Kratos Analytical AXIS ULTRA DLD (Kratos Analytical Ltd., Manchester, UK) spectrometer fitted with a monochromatic Al K _{α} X-ray source and an achromatic Mg K _{α} /Al K _{α} dual-anode X-ray source. A monochromatic Al K _{α} anode (1486.6 eV) operated at 150 W and 15 kV was used. A 180° hemispherical energy analyser with a mean radius of 165 mm was operated using a hybrid lens mode at a pass energy of 160 eV for survey spectra, 20 eV for regions, and 40 eV for regions acquired for the depth profile. XPS spectra were recorded at a 90° takeoff angle from the surface of the sample holder using an aperture field of view Ø 220 μ m. The samples were mounted on stainless steel 130 × 15 mm² sample bar. Binding energy values were calculated based on the C 1s peak at 284.6 eV. For surface cleaning and bulk composition information, a Minibeam I ion (Ar⁺) source (1 kV, 10 mA, 120 s per cycle) was used. The SEM images were taken using a (Zeiss EVO® MA—15 system, Oberkochen, Germany) with an LaB6 cathode in secondary electron mode, applying an accelerating voltage of 10–15 kV and a 6.5–8.5 mm working distance.

3. Results

3.1. Morphology and Tribological Properties

Figure 1 shows the surface morphologies of the a-C:H:Si and Al₂O₃/a-C:H:Si coatings. The alumina layer grew conformally, that is, it resembled the morphology of the a-C:H:Si surface. Similar alumina growth was observed on the NCD film [48]. The morphological peculiarities can be observed on the Al₂O₃/a-C:H:Si coating surface.

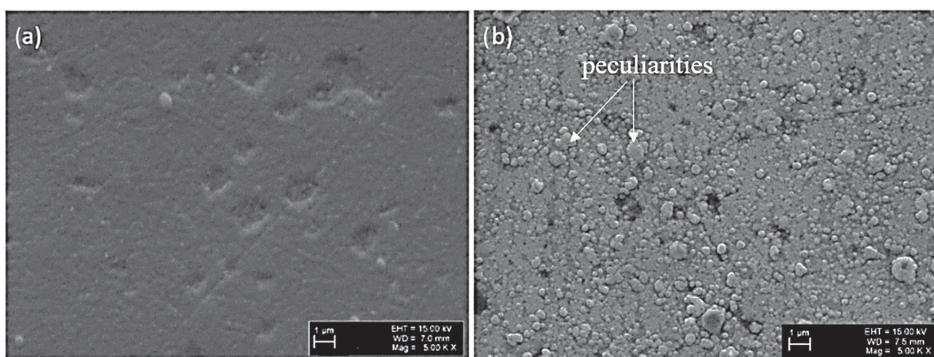


Figure 1. SEM images of the native surface of coatings (a) a-C:H:Si and (b) Al₂O₃/a-C:H:Si.

Figure 2 shows the COF versus cycle curves obtained at RT and 400 °C. The COF values for both types of specimens (a-C:H:Si and Al₂O₃/a-C:H:Si) are very similar for the tests at RT, approximately 0.06–0.1. In other words, the thin alumina layer did not strongly influence the friction behaviour of a-C:H:Si. After reaching the smallest value at the beginning of the test, the COF value slowly increased during subsequent periods of sliding. In contrast to the tests at RT, significant changes occurred in the tests at 400 °C. In the case of the a-C:H:Si coating, coating failure occurred at the beginning of the tests after a short running-in period. The tests were repeated three times (the 5 min test is not shown), and the same friction behaviour was observed. However, in the case of the Al₂O₃/a-C:H:Si coating, relatively stable periods of sliding were revealed, with a COF value of less than 0.03, and some periods had a super-low COF of less than 0.01 (Figure 2b). The extended time tests were repeated three times. A short running-in period was found in the case of the test at RT, which was practically absent from the tests at 400 °C. This shows that the contact between the a-C:H:Si surface and the Si₃N₄ ball was already established at the beginning of the tests.

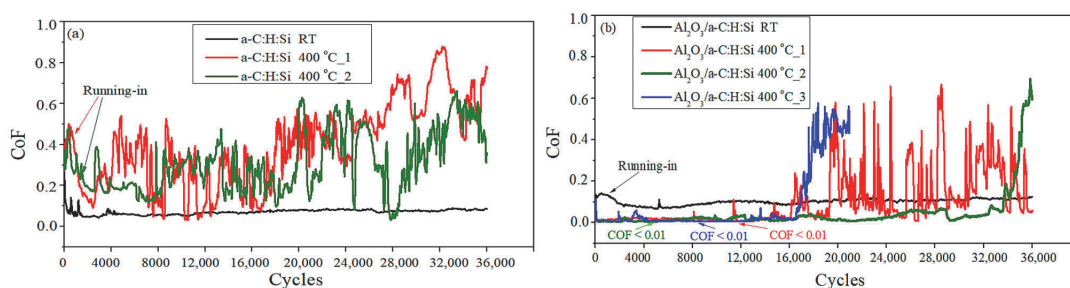


Figure 2. COF versus cycles curves taken on the (a) a-C:H:Si and (b) Al₂O₃/a-C:H:Si coatings.

Figure 3 shows SEM images of the wear scars observed on the a-C:H:Si and Al₂O₃/a-C:H:Si coatings after the sliding tests at RT and 400 °C. The smooth wear surfaces are formed on both coatings after sliding for 180 min at RT. The alumina islands can be seen on the Al₂O₃/a-C:H:Si coating as well (Figure 3b). In the case of the a-C:H:Si coating, islands of the a-C:H:Si coating and the surface of WC-Co substrate can be seen after the test at 400 °C, in spite of uniform a-C:H:Si coating surface for the Al₂O₃/a-C:H:Si specimen.

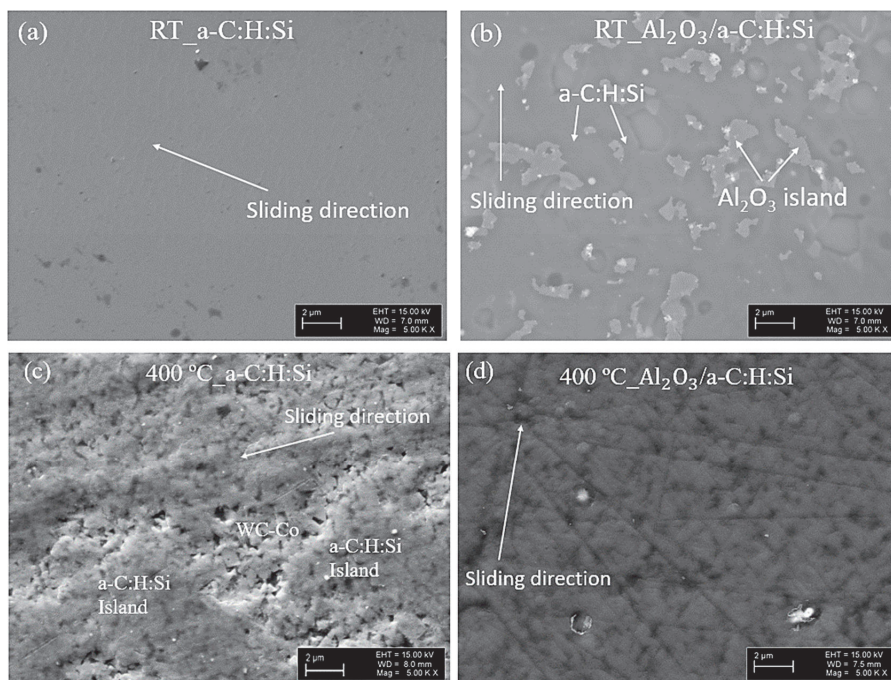


Figure 3. SEM images of wear scars after sliding tests at (a,b) RT for 180 min and (c,d) 400 °C for 5 min.

Figure 4 shows line scans taken across the wear scars. The shape and width of the wear scars obtained after the tests at RT differ between the a-C:H:Si and Al₂O₃/a-C:H:Si coatings. The wear scar widths on the a-C:H:Si and Al₂O₃/a-C:H:Si coatings after the 5-min tests were approximately 200 and 310 μm, respectively. The wear scar was narrower and deeper for the a-C:H:Si specimen and wider and shallower for Al₂O₃/a-C:H:Si after the 180-min tests. The increase in contact area on Al₂O₃/NCD in contrast to an NCD film was also observed in sliding tests at RT [48]. These results demonstrate the adaptation effect mentioned earlier, that is, that an increase in the contact area leads to decreasing contact pressure. The hardness of the Si₃N₄ balls was higher than that of the thin alumina layer, thus it is unlikely that the increased wear scar width was caused by abrasive wear of the balls. The depth of the wear scar was approximately 0.8 μm for the a-C:H:Si coating, which is close to the coating thickness. However, in the case of the Al₂O₃/a-C:H:Si coating, an approximately 0.4 μm-thick a-C:H:Si layer was removed (Figure 4d).

Therefore, a longer lifetime can be expected for the Al₂O₃/a-C:H:Si coating in contrast to the a-C:H:Si coating at RT. The wear scar was also significantly wider after the 5 min test at 400 °C than after the 180 min test at RT for the Al₂O₃/a-C:H:Si coating (Figures 4d and 5b). These results could indicate structural changes within the a-C:H:Si coating, most likely owing to a-C:H:Si graphitisation and decreased hardness [11,26].

The apparent wear volumes were measured on the a-C:H:Si and Al₂O₃/a-C:H:Si specimens (Figure 6). The calculation of the wear volume loss assumed an alumina layer thickness of 200 nm (Figures 4 and 5). The wear volume measured on the a-C:H:Si layer (black colour in Figure 6) was larger for the a-C:H:Si coating than for the Al₂O₃/a-C:H:Si coating after the 180 min tests at RT. The wear volume was largest after the 5 min sliding test at 400 °C on the a-C:H:Si coating owing to the coating failure (Figure 5a). It should be stressed that the reduced hardness of a-C:H:Si at high temperature increased the wear scar width for the Al₂O₃/a-C:H:Si coating (Figure 5b). Therefore, the apparent wear volume loss may increase owing to the plastic deformation of the a-C:H:Si layer [49].

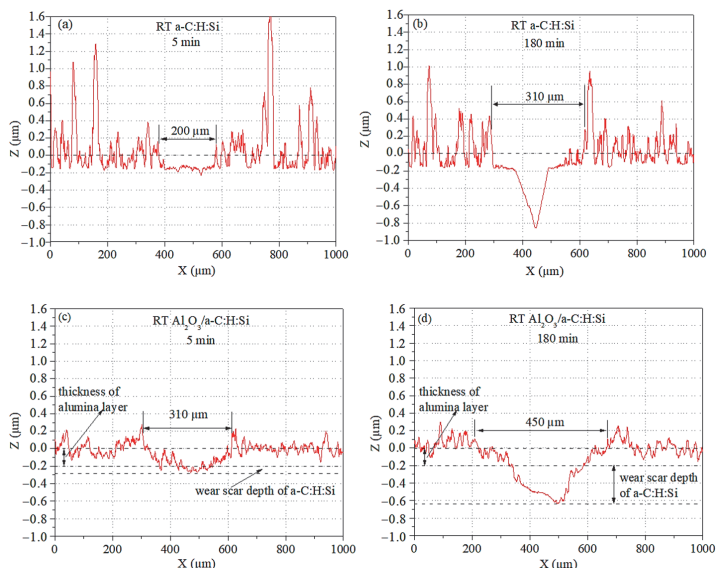


Figure 4. Wear scars line profiles taken on the (a,b) a-C:H:Si and (c,d) Al₂O₃/a-C:H:Si coatings after the (a,c) 5 and (b,d) 180 min tests at RT.

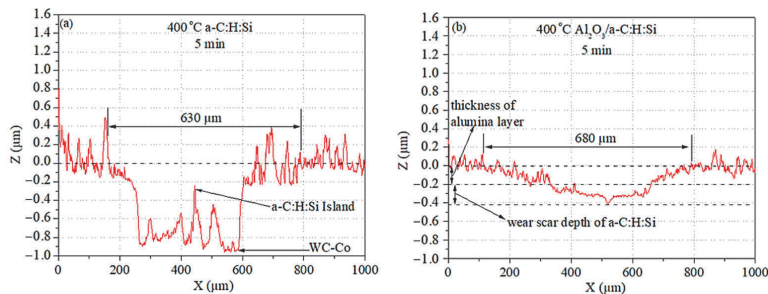


Figure 5. Wear scars line profiles taken on the (a) a-C:H:Si and (b) Al₂O₃/a-C:H:Si coatings after the 5 min sliding tests at 400 °C.

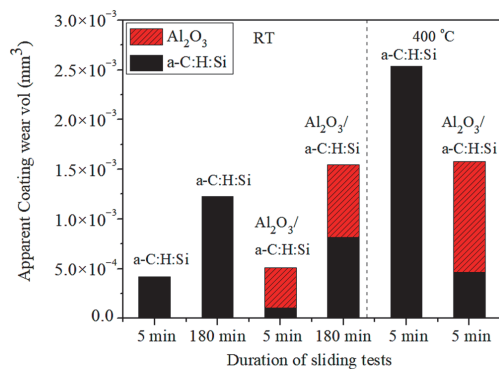


Figure 6. Apparent wear volumes measured on the a-C:H:Si and Al₂O₃/a-C:H:Si coatings.

3.2. Raman and XPS Analyses

Raman spectra were obtained for the native and wear scar surfaces of the a-C:H:Si coating after the sliding tests at RT (Figure 7a). Two characteristic D and G peaks indicated sp^2 structure ordering, that is, the D mode (1365 cm^{-1}) was active in the presence of disorder, and the G mode (1545 cm^{-1}) indicated the presence of well-ordered graphite [6]. Raman peaks corresponding to vibrational modes in t-Pa (1054 cm^{-1}) and sp-bonded chains ($1900\text{--}2200\text{ cm}^{-1}$) were also observed. The shape and position of the Raman peaks in the spectra of the native and wear scar surfaces after the 5 and 180 min tests at RT were quite similar. In the case of the $\text{Al}_2\text{O}_3/\text{a-C:H:Si}$ coating (Figure 7c), the peak positions were similar to those observed for the a-C:H:Si coating, except that the G peak shifted to 1532 cm^{-1} after the 180 min sliding test. The Raman spectrum of the native a-C:H:Si surface differed from that after heating at high temperatures. The G peak shifted to 1558 cm^{-1} , and formation of a shoulder (arrow in Figure 7b) was observed after heating at $400\text{ }^\circ\text{C}$. The G peak shifted to a higher value (1612 cm^{-1}) after the 5 min test at $400\text{ }^\circ\text{C}$ (Figure 7b), which indicates the impact of mechanochemical processes on the a-C:H:Si structure. For the sake of clarity, Raman measurements were repeated for at least three different locations within the wear scar, and similar spectra were recorded (Figure 7b). However, in the case of the $\text{Al}_2\text{O}_3/\text{a-C:H:Si}$ coating, no further G peak shift was observed after the 5 min test at $400\text{ }^\circ\text{C}$ (Figure 7d). The peak positions and shapes were similar to those observed in the Raman spectrum of the native surface of the a-C:H:Si coating after heating at $400\text{ }^\circ\text{C}$ (Figure 7b).

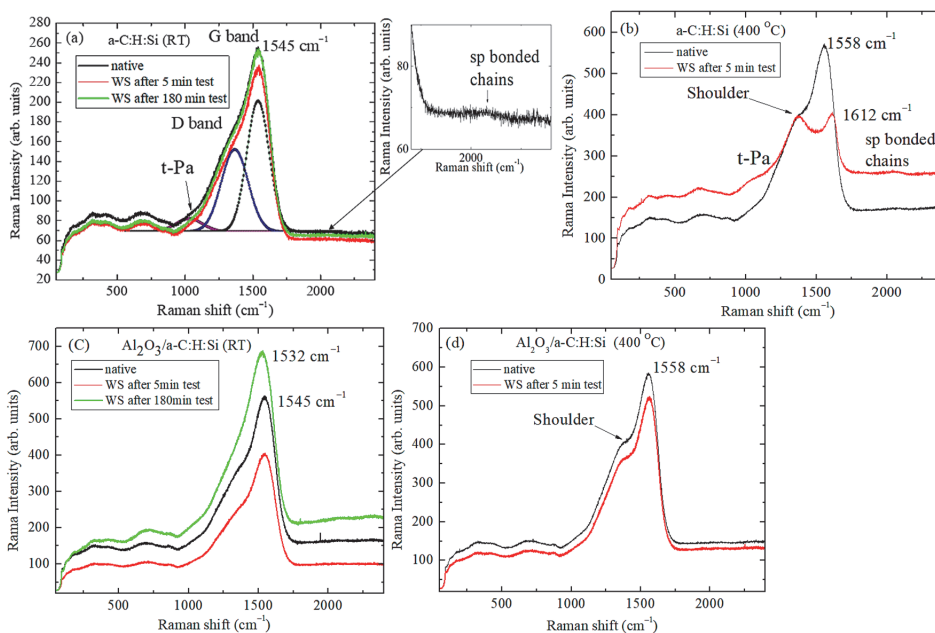


Figure 7. Raman spectra taken on the native surface and within the wear scars after the 5 and 180 min tests at RT and $400\text{ }^\circ\text{C}$ on the (a,b) a-C:H:Si and (c,d) $\text{Al}_2\text{O}_3/\text{a-C:H:Si}$ coatings. The insert shows the peak $1900\text{--}2200\text{ cm}^{-1}$ corresponding to sp-bonded chains. Deconvolution of Raman spectra of the native a-C:H:Si is shown.

The C 1s XPS spectra were recorded on the a-C:H:Si native surface (Figure 8). The peaks corresponded to C–C sp^2 , C–C sp^3 , C–O, C=O, C–N, O–C=O and COO–R bonds [46,50,51]. sp^3 surface enrichment and increased intensity of the XPS spectrum shoulder corresponding to the bonds formed between carbon, nitrogen, and oxygen atoms were observed after heating at $400\text{ }^\circ\text{C}$ (Figure 8b). Figure 9 shows the XPS spectra taken on the surface of the wear scars after the sliding tests at RT and $400\text{ }^\circ\text{C}$. The intensity

ratio between the XPS signal intensity related to the a-C:H:Si coating (convolution of the C–C sp^2 and sp^3 peaks) and the intensity of the peak corresponding to C–O, C=O, etc., bonds is higher for a-C:H:Si than for the $Al_2O_3/a-C:H:Si$ coating. The C–C sp^2 and sp^3 XPS signals can be more strongly shielded on the $Al_2O_3/a-C:H:Si$ coating by a thicker and more uniformly distributed layer formed by agents such as C–O, C=O, etc.

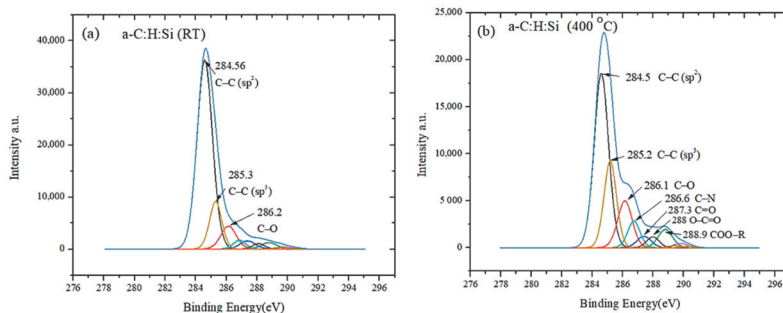


Figure 8. C1s XPS spectra taken on the a-C:H:Si coating native surface at (a) RT and (b) 400 °C.

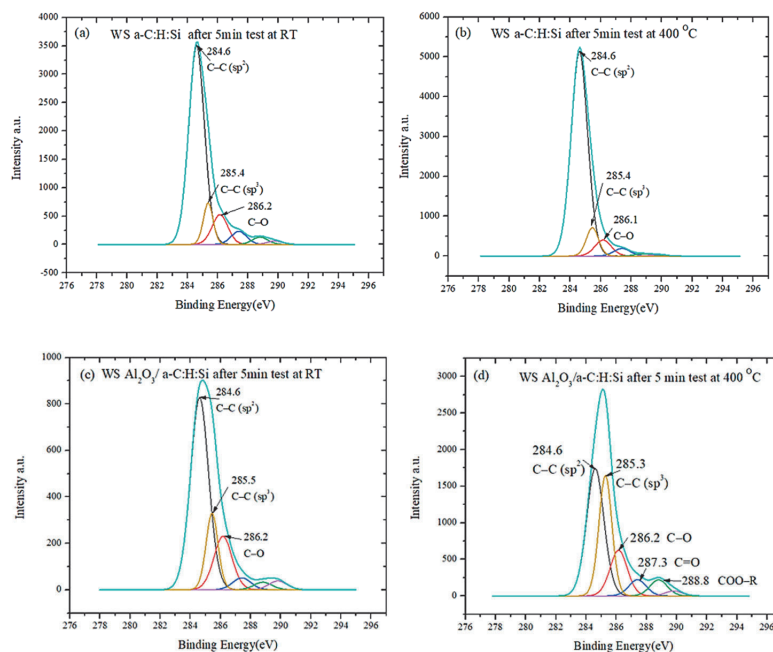


Figure 9. C 1s XPS spectra taken within the wear scars after the 5 min tests at RT and 400 °C on the (a,b) a-C:H:Si and (c,d) $Al_2O_3/a-C:H:Si$ coatings.

Figures 10 and 11 show the O 1s and Si 2p XPS spectra, respectively. The O 1s XPS spectra were quite similar for both types of specimens. It is expected that the XPS signal indicates electrons released from oxygen bonded mainly with C, H, Si, Al, and N atoms. The stronger peak at 531.6 eV after the heating of a-C:H:Si at 400 °C can be observed in contrast to the $Al_2O_3/a-C:H:Si$ coating. Closely spaced spin-orbit components ($\Delta = 0.63$ eV) formed an asymmetrical Si 2p peak at 100.5–100.6 eV, which corresponds to Si–C bonds in a-C:H:Si [52]. The broad Si 2p XPS spectra indicate the presence of several types of silicon oxide with different chemical states of Si ($Si^{1+}(Si_2O)$, $Si^{2+}(SiO)$, $Si^{3+}(Si_2O_3)$, and

Si⁴⁺(SiO₂) [46]. Due to the likely a-C:H:Si oxidation and formation of the silicon oxides, the Si–C peak intensity decreased after heating at 400 °C (Figure 11a). The Si 2p XPS spectra taken within the wear scars after the sliding test at 400 °C showed the strongest peaks located at 102.5–103.2 eV, which could indicate the formation of stoichiometric SiO₂ oxide. However, there is a difference between the Si 2p XPS spectra of the a-C:H:Si and Al₂O₃/a-C:H:Si coatings (Figure 11a,b, respectively). For example, the strongest peak in the spectrum taken on the Al₂O₃/a-C:H:Si surface is located at 102.5 eV, in contrast to 103.2 eV for a-C:H:Si. The Si 2p XPS spectra may also have been influenced by the Si₃N₄ ball wear debris during the sliding tests.

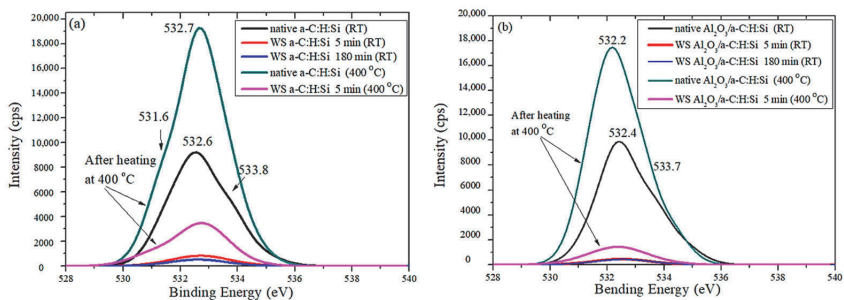


Figure 10. O 1s XPS spectra taken within the native and wear scars surfaces after sliding tests at RT and 400 °C on the (a) a-C:H:Si and (b) Al₂O₃/a-C:H:Si coatings.

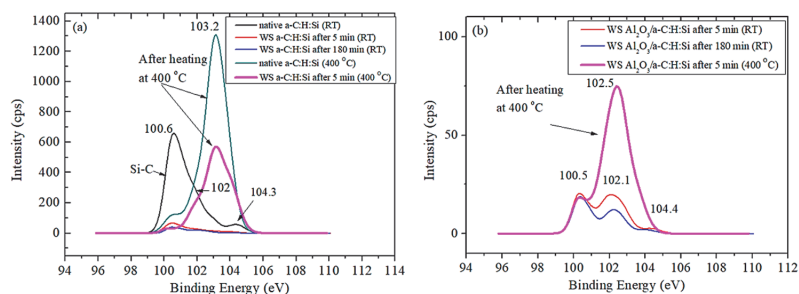


Figure 11. Si 2p XPS spectra taken within the native and wear scars surfaces after the sliding tests at RT and 400 °C on the (a) a-C:H:Si and (b) Al₂O₃/a-C:H:Si coatings.

Figure 12 shows the N 1s XPS spectra. In the case of the a-C:H:Si coating, the peak at 402.1 eV (N–O) [51] was observed after the 5 min sliding test at 400 °C.

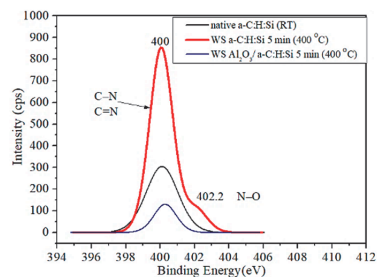


Figure 12. N 1s XPS spectra taken within the native and wear scars surfaces after the 5 min tests at RT and 400 °C on the a-C:H:Si and Al₂O₃/a-C:H:Si coatings.

4. Discussion

Figure 13 shows the results of the Raman and XPS investigations of the sp^2 and sp^3 bond contents in the coatings. In the case of the a-C:H:Si coating, the intensity ratios of the D and G peaks (I_D/I_G ratio) are similar for the Raman spectra taken on the native surface and within the wear scars after the 5 and 180 min sliding tests at RT (Figure 13a). For the same specimens, the sp^2/sp^3 ratios of the corresponding XPS peak intensities were similar (Figure 13b). Therefore, these results suggest that mechanochemical processes occurring during sliding tests at RT did not affect the sp^2 and sp^3 hybridised bonding networks in the bulk and on the surface of the a-C:H:Si coating. This demonstrates the high stability of the a-C:H:Si structure in sliding tests at RT. However, the investigation of the a-C:H:Si native surface after heating at 400 °C shows that the sp^2 and sp^3 contents in the bulk and on the surface changed in different ways. In contrast to the investigations at RT, the analysis of the I_D/I_G ratio suggests an increase in the sp^2 content in the bulk; however, the XPS data showed a decrease in the sp^2 content on the surface and sp^3 surface enrichment. The sp^3 surface enrichment after annealing in air owing to preferable etching of the sp^2 bonds located within the grain boundaries has been found on diamond films [48,53]. The release of carbon from the a-C:H:Si surface during annealing at 400 °C was observed by Rouhani et al. [46].

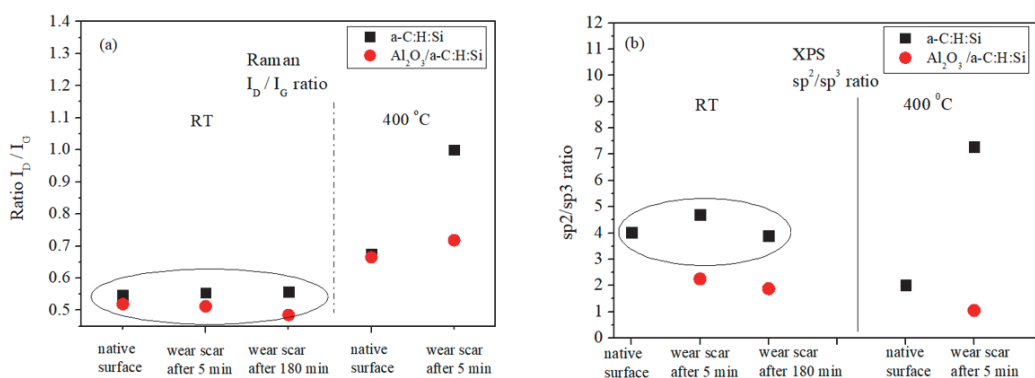


Figure 13. Summary of the results of (a) Raman and (b) XPS investigations.

In the case of the Al₂O₃/a-C:H:Si coating, comparison of the I_D/I_G ratios obtained for the native and wear scar surfaces after the 5 and 180 min tests showed that this ratio also remained stable at RT (Figure 13a). However, the I_D/I_G ratio tended to decrease for the 180 min test as compared with the measurements on the native surface and wear scar after the 5 min test, which indicates likely surface sp^3 enrichment within the wear scar. The XPS investigation supports this conclusion (Figure 13b), as well as the G peak shift to 1532 cm^{-1} observed after 180 min (Figure 7c). The extra oxygen delivered by the alumina layer seems to have caused surface sp^3 enrichment in the wear scars after the sliding tests at RT on the Al₂O₃/a-C:H:Si coating owing to mechanochemical processes. This conclusion is in good agreement with the increased sp^3 bond content in the oxygen-doped carbon-based coating [31,36].

In the case of the a-C:H:Si and Al₂O₃/a-C:H:Si coatings, the increased I_D/I_G ratio suggests an increase in the sp^2 content for both types of specimens after the 5 min tests at 400 °C (Figure 13a). The thermally and mechanochemically induced processes intensified the a-C:H:Si graphitisation. However, the increase in the sp^2 bond content was significantly higher for the a-C:H:Si coating than for Al₂O₃/a-C:H:Si coating, and a shift of the G peak to 1612 cm^{-1} was observed for the a-C:H:Si coating (Figure 7b). This shift could indicate an increase in the number of defects, formation of a graphene sheet owing to graphite slicing, and formation of double bonds between carbon atoms [54]. There was a significant

difference between the a-C:H:Si and Al₂O₃/a-C:H:Si coatings, namely, sp³ enrichment of the wear scar surface on the Al₂O₃/a-C:H:Si coating after the 5 min test at 400 °C (Figure 13b).

The results of the Raman and XPS investigations suggest that the interaction between the a-C:H:Si surface and atmospheric oxygen differed from the interaction with the oxygen in alumina. It is expected that the alumina layer suppressed atmospheric oxygen diffusion to the a-C:H:Si surface [48].

To summarise, improvements in the tribological properties and thermal stability were observed in sliding tests at RT and 400 °C for the Al₂O₃/a-C:H:Si coating in comparison with the a-C:H:Si coating. First, an increase in the contact area and sp³ surface enrichment within the wear scar was observed in the tests at RT and 400 °C. The alumina layer was considered the adaptive layer. The adaptation effect was manifested owing to the use of a relatively soft and thin alumina layer, resulting in the increased contact area. The delivery of extra oxygen to the contact area led to increased sp³ content within the thin tribolayer, which improved the thermal stability and increased the hardness and internal stress of the tribolayer [28–31,36]. In addition, it was shown in a study on an Al₂O₃/NCD film [48] that the alumina layer is the atmospheric oxygen diffusion barrier layer. These factors determine the running-in conditions and tribological performance during extended time tests (hereditary effects). The decreased contact pressure owing to the increased contact area and improved mechanical properties of the thin tribolayer led to the better tribological behaviour of Al₂O₃/a-C:H:Si coating in contrast to the a-C:H:Si coating.

Second, carbon surface hydroxylation (C–OH termination) results in better tribological properties [38]. This type of surface passivation improves surface hydrophilicity and the absorption of atmospheric water vapour [39]. The super-low COF value for the a-C:H:Si coating with a low Si concentration (3.6 at.%–11.4 at.%) is explained by the formation of additional Si–OH hydrophilic bonds. Under ambient humid conditions (30%–60% humidity), water and oxygen absorbed by the surface form a well-ordered easily shared layer-like film, resulting in low friction [17]. In addition, higher surface energies for a-C:H:Si and ta-C coating surfaces after oxygen plasma treatment have been reported [34,39], which means higher surface wettability, which leads to more uniform water distribution along the surface. This, in turn, is likely to be beneficial for the formation of a layer-like water structure on the a-C:H:Si surface. In conclusion, it is expected that the hydrophilicity and wettability of Al₂O₃/a-C:H:Si within the wear scar area can be improved owing to the extra oxygen delivered by the alumina layer. This interpretation is supported by the XPS investigation, as discussed in Section 3.2.

Third, silicon oxide affects the tribological behaviour of DLC coatings. The XPS study revealed several types of silicon oxide formed within the wear scar. The influence of a particular type of oxide should be investigated in more detail.

Fourth, the mechanism of hydrogen effusion may differ between the a-C:H:Si and Al₂O₃/a-C:H:Si coatings because of the alumina layer and a specific tribolayer layer formed on Al₂O₃/a-C:H:Si during the sliding tests. Upon thermal treatment, the hydrogen content decreases owing to the release of hydrogen and hydrocarbons (C_nH_x) [32]. The mechanisms of hydrogen diffusion in alumina usually consider the diffusion of H atoms or H⁺ ions [55]. The hydrogen diffusion coefficient in alumina has a certain value; therefore, the hydrogen effusion in the Al₂O₃/a-C:H:Si coating can be suppressed by the alumina layer. In the case of hydrocarbons, it was found that the pore size in a-C:H strongly influences diffusion [32]. Thus, hydrocarbon diffusion through alumina can be limited as well. In conclusion, the alumina layer can be considered a hydrogen diffusion barrier layer.

5. Conclusions

A comparative study of the tribological properties of the a-C:H:Si and Al₂O₃/a-C:H:Si coatings at RT and 400 °C was performed. After 180 min sliding tests at RT, a wider and shallower wear scar was found on the Al₂O₃/a-C:H:Si coating in contrast to the a-C:H:Si coating. The smaller depth indicates that the a-C:H:Si coating lifetime can be increased by

preparing an Al₂O₃/a-C:H:Si structure. The alumina layer changes the contact conditions and influences the running-in behaviour owing to the increased contact area and decreased contact pressure (adaptation effect). The chemical composition in the contact area can also be changed owing to the extra oxygen delivered by the alumina layer. The results demonstrate the hereditary effect and the initial contact conditions strongly influence the tribological performance of the extended time tests.

The thermal stability of the a-C:H:Si coating can be improved by deposition of an alumina layer. The a-C:H:Si coating was unstable in sliding tests at 400 °C; however, a stable low-friction regime of sliding over 80–160 min was observed for the Al₂O₃/a-C:H:Si coating. The chemical composition of the tribolayer on Al₂O₃/a-C:H:Si differed from that of the a-C:H:Si coating after the sliding tests at 400 °C. An increase in the sp³ bond content was observed for the Al₂O₃/a-C:H:Si coating; therefore, better mechanical and thermal properties of the tribolayer formed on an Al₂O₃/a-C:H:Si coating are expected. The extra oxygen in the contact area improved the structure and properties of the passivation layer formed on the a-C:H:Si surface, resulting in low friction.

Further investigations are needed to continue efforts towards understanding the mutual influence between the test conditions and the DLC and alumina layer properties.

Author Contributions: Conceptualization, V.P. and A.A.; methodology, V.P.; software, A.A. and M.Y.; validation, A.B. and A.A.; formal analysis, V.P.; and A.A.; investigation, A.A.; T.J.; T.R.; M.V. and M.D.; resources, V.P.; data curation, A.A.; writing—original draft preparation, V.P.; and A.A.; writing—review and editing, F.S.; J.S.; A.L.; and J.K.; visualization, A.A.; supervision, V.P.; project administration, V.P.; funding acquisition, V.P. All authors have read and agreed to the published version of the manuscript.

Funding: This research was funded by the Estonian Ministry of Education and Research under financing projects PUT 1369 and TK134 “Emerging orders in quantum and nanomaterials”.

Institutional Review Board Statement: Not applicable.

Informed Consent Statement: Not applicable.

Data Availability Statement: Not applicable.

Conflicts of Interest: The authors declare no conflict of interest.

References

- Holmberg, K.; Erdemir, A. Influence of tribology on global energy consumption, costs and emissions. *Friction* **2017**, *5*, 263–284. [[CrossRef](#)]
- Kowalski, S. The influence of selected PVD coatings on fretting wear in a clamped joint based on the example of a rail vehicle wheel set. *Ekspolatacja Niezawodn. Maint. Reliab.* **2017**, *20*, 1–8. [[CrossRef](#)]
- Rybachuk, M.; Bell, J. Electronic states of trans-polyacetylene, poly(p-phenylene vinylene) and sp-hybridised carbon species in amorphous hydrogenated carbon probed by resonant Raman scattering. *Carbon* **2009**, *47*, 2481–2490. [[CrossRef](#)]
- Mulazzi, E.; Brivio, G.P.; Faulques, E.; Lefrant, S. Experimental and theoretical raman results in transpolyacetylene. *Solid State Commun.* **1983**, *46*, 851–855. [[CrossRef](#)]
- Ravagnan, L.; Manini, N.; Cinquanta, E.; Onida, G.; Sangalli, D.; Motta, C.; Devetta, M.; Bordoni, A.; Piseri, P.; Milani, P. Effect of axial torsion on sp carbon atomic wires. *Phys. Rev. Lett.* **2009**, *102*, 245502. [[CrossRef](#)]
- Ferrari, A.C.; Robertson, J. Raman spectroscopy of amorphous, nanostructured, diamond-like carbon, and nanodiamond. *Philos. Trans. R. Soc. A Math. Phys. Eng. Sci.* **2004**, *362*, 2477–2512. [[CrossRef](#)]
- Hilbert, J.; Mangolini, F.; McClimon, J.; Lukes, J.; Carpick, R. Si doping enhances the thermal stability of diamond-like carbon through reductions in carbon-carbon bond length disorder. *Carbon* **2018**, *131*, 72–78. [[CrossRef](#)]
- Dongping, L.; Baoxiang, C.; Yanhong, L. Structures of diamond-like carbon films. *Plasma Sci. Technol.* **2006**, *8*, 285–291. [[CrossRef](#)]
- Kalish, R.; Lifshitz, Y.; Nugent, K.; Prawer, S. Thermal stability and relaxation in diamond-like-carbon. A Raman study of films with different sp³ fractions (ta-C to a-C). *Appl. Phys. Lett.* **1999**, *74*, 2936–2938. [[CrossRef](#)]
- Rybachuk, M.; Bell, J.M. The effect of sp² fraction and bonding disorder on micro-mechanical and electronic properties of a-C:H films. *Thin Solid Film.* **2007**, *515*, 7855–7860. [[CrossRef](#)]
- Li, H.; Xu, T.; Wang, C.; Chen, J.; Zhou, H.; Liu, H. Annealing effect on the structure, mechanical and tribological properties of hydrogenated diamond-like carbon films. *Thin Solid Film.* **2006**, *515*, 2153–2160. [[CrossRef](#)]
- Tallant, D.; Parmeter, J.; Siegal, M.; Simpson, R. The thermal stability of diamond-like carbon. *Diam. Relat. Mater.* **1995**, *4*, 191–199. [[CrossRef](#)]

13. Pastewka, L.; Moser, S.; Gumbsch, P.; Moseler, M. Anisotropic mechanical amorphization drives wear in diamond. *Nat. Mater.* **2010**, *10*, 34–38. [[CrossRef](#)] [[PubMed](#)]
14. Yu, Q.; Chen, X.; Zhang, C.; Luo, J. Influence factors on mechanisms of superlubricity in DLC films: A review. *Front. Mech. Eng.* **2020**, *6*, 65. [[CrossRef](#)]
15. Țucureanu, V.; Matei, A.; Avram, A.M. FTIR spectroscopy for carbon family study. *Crit. Rev. Anal. Chem.* **2016**, *46*, 502–520. [[CrossRef](#)] [[PubMed](#)]
16. Fontaine, J.; Loubet, J.L.; Mogne, T.L.; Grill, A. Superlow friction of diamond-like carbon films: A relation to viscoplastic properties. *Tribol. Lett.* **2004**, *17*, 709–714. [[CrossRef](#)]
17. Chen, X.; Kato, T.; Kawaguchi, M.; Nosaka, M.; Choi, J. Structural and environmental dependence of superlow friction in ion vapour-deposited a-C:H:Si films for solid lubrication application. *J. Phys. D Appl. Phys.* **2013**, *46*, 255304. [[CrossRef](#)]
18. Kano, M.; Yasuda, Y.; Okamoto, Y.; Mabuchi, Y.; Hamada, T.; Ueno, T.; Ye, J.; Konishi, S.; Takeshima, S.; Martin, J.M.; et al. Ultralow friction of DLC in presence of glycerol mono-oleate (GNO). *Tribol. Lett.* **2005**, *18*, 245–251. [[CrossRef](#)]
19. Holmberg, K.; Ronkainen, H.; Laukkanen, A.; Wallin, K. Friction and wear of coated surfaces—Scales, modelling and simulation of tribomechanisms. *Surf. Coat. Technol.* **2007**, *202*, 1034–1049. [[CrossRef](#)]
20. Erdemir, A. The role of hydrogen in tribological properties of diamond-like carbon films. *Surf. Coat. Technol.* **2001**, *146*–*147*, 292–297. [[CrossRef](#)]
21. Zeng, Q.; Eryilmaz, O.; Erdemir, A. Superlubricity of the DLC films-related friction system at elevated temperature. *RSC Adv.* **2015**, *5*, 93147–93154. [[CrossRef](#)]
22. Kano, M.; Martin, J.M.; Yoshida, K.; Bouchet, M.I.D.B. Super-low friction of ta-C coating in presence of oleic acid. *Friction* **2014**, *2*, 156–163. [[CrossRef](#)]
23. Kuwahara, T.; Romero, P.A.; Makowski, S.; Wehnacht, V.; Moras, G.; Moseler, M. Mechano-chemical decomposition of organic friction modifiers with multiple reactive centres induces superlubricity of ta-C. *Nat. Commun.* **2019**, *10*, 151. [[CrossRef](#)]
24. Ikeyama, M.; Nakao, S.; Miyagawa, Y. Effects of Si content in DLC films on their friction and wear properties. *Surf. Coat. Technol.* **2005**, *191*, 38–42. [[CrossRef](#)]
25. Baba, K.; Hatada, R.; Flege, S.; Ensinger, W. Deposition of silicon-containing diamond-like carbon films by plasma-enhanced chemical vapour deposition. *Surf. Coat. Technol.* **2009**, *203*, 2747–2750. [[CrossRef](#)]
26. Zhang, T.F.; Wan, Z.X.; Ding, J.C.; Zhang, S.; Wang, Q.M.; Kim, K.H. Microstructure and high-temperature tribological properties of Si-doped hydrogenated diamond-like carbon films. *Appl. Surf. Sci.* **2018**, *435*, 963–973. [[CrossRef](#)]
27. Wang, J.; Pu, J.; Zhang, G.; Wang, L. Interface architecture for superthick carbon-based films toward low internal stress and ultrahigh load-bearing capacity. *ACS Appl. Mater. Interfaces* **2013**, *5*, 5015–5024. [[CrossRef](#)] [[PubMed](#)]
28. Moolsradoo, N.; Abe, S.; Watanabe, S. Thermal stability and tribological performance of DLC-Si-O films. *Adv. Mater. Sci. Eng.* **2011**, *2011*, 1–7. [[CrossRef](#)]
29. Mangolini, F.; Krick, B.A.; Jacobs, T.D.; Khanal, S.R.; Streller, F.; McClimon, J.B.; Hilbert, J.; Prasad, S.V.; Scharf, T.W.; Ohlhausen, J.A.; et al. Effect of silicon and oxygen dopants on the stability of hydrogenated amorphous carbon under harsh environmental conditions. *Carbon* **2018**, *130*, 127–136. [[CrossRef](#)]
30. Zhang, D.; Li, S.; Zuo, X.; Guo, P.; Ke, P.; Wang, A. Structural and mechanism study on enhanced thermal stability of hydrogenated diamond-like carbon films doped with Si/O. *Diam. Relat. Mater.* **2020**, *108*, 107923. [[CrossRef](#)]
31. Safaie, P.; Eshaghi, A.; Bakhshi, S.R. Structure and mechanical properties of oxygen doped diamond-like carbon thin films. *Diam. Relat. Mater.* **2016**, *70*, 91–97. [[CrossRef](#)]
32. Wild, C.; Koidl, P. Thermal gas effusion from hydrogenated amorphous carbon films. *Appl. Phys. Lett.* **1987**, *51*, 1506–1508. [[CrossRef](#)]
33. Yang, B.; Zheng, Y.; Zhang, B.; Wei, L.; Zhang, J. The high-temperature tribological properties of Si-DLC films. *Surf. Interface Anal.* **2012**, *44*, 1601–1605. [[CrossRef](#)]
34. Kim, J.-I.; Jang, Y.-J.; Kim, J.; Jeong, J.H. Improvement of running-in process of tetrahedral amorphous carbon film sliding against Si₃N₄ under humid air by O₂ plasma post-irradiation. *Appl. Surf. Sci.* **2021**, *538*, 147957. [[CrossRef](#)]
35. Fredriksson, H.; Chakarov, D.; Kasemo, B. Patterning of highly oriented pyrolytic graphite and glassy carbon surfaces by nanolithography and oxygen plasma etching. *Carbon* **2009**, *47*, 1335–1342. [[CrossRef](#)]
36. Guo, M.; Diao, D.; Fan, X.; Yang, L.; Yu, L. Scratch behavior of re-structured carbon coating by oxygen plasma etching technology for magnetic disk application. *Surf. Coat. Technol.* **2014**, *251*, 128–134. [[CrossRef](#)]
37. Choi, J.; Nakao, S.; Ikeyama, M.; Kato, T. Effect of oxygen plasma treatment on the tribological properties of Si-DLC coatings. *Phys. Status Solid* **2008**, *5*, 956–959. [[CrossRef](#)]
38. Jongwannasiri, C.; Watanabe, S. Tribological behavior of O₂ and CF₄ plasma post-treated diamond-like carbon films under dry air and in a high relative humidity environment. *Surf. Coat. Technol.* **2016**, *306*, 200–204. [[CrossRef](#)]
39. López-Santos, C.; Yubero, F.; Cotrino, J.; González-Elipse, A. Lateral and in-depth distribution of functional groups on diamond-like carbon after oxygen plasma treatments. *Diam. Relat. Mater.* **2011**, *20*, 49–56. [[CrossRef](#)]
40. Corona-Gomez, J.; Shiri, S.; Mohammadtaheri, M.; Yang, Q. Adhesion enhancement of DLC on CoCrMo alloy by diamond and nitrogen incorporation for wear resistant applications. *Surf. Coat. Technol.* **2017**, *332*, 120–127. [[CrossRef](#)]
41. Rao, X.; Yang, J.; Chen, Z.; Yuan, Y.; Chen, Q.; Feng, X.; Qin, L.; Zhang, Y. Tuning C–C sp²/sp³ ratio of DLC films in FCVA system for biomedical application. *Bioact. Mater.* **2020**, *5*, 192–200. [[CrossRef](#)]

42. Fox-Rabinovich, G.S. Principles of friction control for surface-engineered materials. In *Self-Organization during Friction. Advanced Surface-Engineered Materials and Systems Design*; Fox-Rabinovich, G.S., Totten, G.E., Eds.; CRC Press: Boca Raton, FL, USA, 2006; pp. 3–12.
43. Podgursky, V.; Bogatov, A.; Yashin, M.; Sobolev, S.; Gershman, I.S. Relation between self-organization and wear mechanisms of diamond films. *Entropy* **2018**, *20*, 279. [[CrossRef](#)] [[PubMed](#)]
44. Li, H.; Vlassak, J.J. Determining the elastic modulus and hardness of an ultra-thin film on a substrate using nanoindentation. *J. Mater. Res.* **2009**, *24*, 1114–1126. [[CrossRef](#)]
45. Jögiaas, T.; Zabels, R.; Tamm, A.; Merisalu, M.; Hussainova, I.; Heikkilä, M.; Mändar, H.; Kukli, K.; Ritala, M.; Leskelä, M. Mechanical properties of aluminum, zirconium, hafnium and tantalum oxides and their nanolaminates grown by atomic layer deposition. *Surf. Coat. Technol.* **2015**, *282*, 36–42. [[CrossRef](#)]
46. Rouhani, M.; Hobley, J.; Hong, F.C.-N.; Jeng, Y.-R. Spectroscopic investigation of thermally induced structural evolution of a-C:H:Si film. *Appl. Surf. Sci.* **2020**, *541*, 148413. [[CrossRef](#)]
47. Åstrand, M.; Selinder, T.; Fietzke, F.; Klostermann, H. PVD- Al_2O_3 -coated cemented carbide cutting tools. *Surf. Coat. Technol.* **2004**, *188–189*, 186–192. [[CrossRef](#)]
48. Podgursky, V.; Yashin, M.; Jögiaas, T.; Viljus, M.; Alamgir, A.; Danilson, M.; Bogatov, A. high temperature tribological properties of Al_2O_3 /NCD films investigated under ambient air conditions. *Coatings* **2020**, *10*, 175. [[CrossRef](#)]
49. Alamgir, A.; Yashin, M.; Bogatov, A.; Viljus, M.; Traksmaa, R.; Sondor, J.; Lümekemann, A.; Sergejev, F.; Podgursky, V. High-temperature tribological performance of hard multilayer TiN-AlTiN/nACo-CrN/AlCrN-AlCrO-AlTiCrN coating deposited on WC-Co Substrate. *Coatings* **2020**, *10*, 909. [[CrossRef](#)]
50. Mangolini, F.; Hilbert, J.; McClimon, J.B.; Lukes, J.R.; Carpick, R.W. Thermally induced structural evolution of silicon- and oxygen-containing hydrogenated amorphous carbon: A combined spectroscopic and molecular dynamics simulation investigation. *Langmuir* **2018**, *34*, 2989–2995. [[CrossRef](#)] [[PubMed](#)]
51. Scharf, T.W.; Ott, R.D.; Yang, D.; Barnard, J.A. Structural and tribological characterization of protective amorphous diamond-like carbon and amorphous CN_x overcoats for next generation hard disks. *J. Appl. Phys.* **1999**, *85*, 3142–3154. [[CrossRef](#)]
52. XPS Interpretation of Silicon. Available online: <https://xpsimplified.com/elements/silicon.php> (accessed on 1 April 2021).
53. Pu, J.-C.; Wang, S.-F.; Sung, J.C. High-temperature oxidation behavior of nanocrystalline diamond films. *J. Alloy. Compd.* **2010**, *489*, 638–644. [[CrossRef](#)]
54. Kudin, K.N.; Ozbas, B.; Schniepp, H.C.; Prud'Homme, R.K.; Aksay, I.A.; Car, R. Raman spectra of graphite oxide and functionalized graphene sheets. *Nano Lett.* **2008**, *8*, 36–41. [[CrossRef](#)] [[PubMed](#)]
55. Doremus, R.H. Diffusion in alumina. *J. Appl. Phys.* **2006**, *100*, 101301. [[CrossRef](#)]

Curriculum vitae

Personal Data

Name: Asad Alamgir Shaikh
Date of birth : 31.08.1988
Place of birth: Hyderabad
Citizenship: Pakistan

Contact data

Email: asad.shaikh@taltech.ee

Education

2017–2021 Tallinn University of Technology – PhD
2015–2017 National University of Science and Technology MISIS – MSC (Master of Engineering)
2009–2012 Dawood University of Engineering and Technology – BSC (Bachelor of Engineering)

Language competence

Urdu Native speaker
English Fluent
Russian Basic

Professional employment

2017–2018 Tallinn University of Technology, Department of Mechanical and Industrial Engineering, Early Stage Researcher
2013–2015 Quality control engineering at hot forging and heat treatment plant

Involvement in research projects

IUT19–29 Multi-scale structured ceramic-based composites for extreme applications
PUT1369 Adaptation mechanisms of diamond films in dry sliding wear

Elulookirjeldus

Isikuandmed

Nimi: Asad Alamgir Shaikh
Sünniaeg: 31.08.1988
Sünnikoht: Hyderabad
Kodakondsus: Pakistan

Kontaktandmed

E-post: asad.shaikh@taltech.ee

Hariduskäik

2017–2021 Tallinna Tehnikaülikool – PhD
2015–2017 National University of Science and Technology MISIS – MSC
(Tehnikateaduse magister)
2009–2012 Dawood University of Engineering and Technology – BSC
(Tehnikateaduse bakalaureus)

Keelteoskus

Urdu Emakeel
Inglise Kõrgtase
Vene Algtase

Teenistuskäik

2017–2018 Tallinna Tehnikaülikool, Mehaanika ja tööstustehnika instituut,
doktorant-nooremteadur
2013–2015 Kuumsurvetöötlemise ja termotöötamise kvaliteediinsener

Osalemine teadus- ja arendusprojektides

IUT19–29 Mitmeastmeliselt struktureeritud keraamika-baasil komposiitmaterjalid
kasutamiseks ekstreemtingimustes
PUT1369 Teemantpinnete adaptatsioonimehhanismid kuiv hõõrdekulumise

ISSN 2585-6901 (PDF)
ISBN 978-9949-83-706-9 (PDF)